

UC Berkeley

UC Berkeley Previously Published Works

Title

Search for flavour-changing neutral-current interactions of a top quark and a gluon in pp collisions at $s=13$ TeV with the ATLAS detector

Permalink

<https://escholarship.org/uc/item/8x01c6rj>

Journal

European Physical Journal C, 82(4)

ISSN

1434-6044

Authors

Aad, G
Abbott, B
Abbott, DC
[et al.](#)

Publication Date

2022-04-01

DOI

10.1140/epjc/s10052-022-10182-7

Peer reviewed



Search for flavour-changing neutral-current interactions of a top quark and a gluon in pp collisions at $\sqrt{s} = 13$ TeV with the ATLAS detector

ATLAS Collaboration*

CERN, 1211 Geneva 23, Switzerland

Received: 3 December 2021 / Accepted: 4 March 2022 / Published online: 19 April 2022
© CERN for the benefit of the ATLAS collaboration 2022

Abstract A search is presented for the production of a single top quark via left-handed flavour-changing neutral-current (FCNC) interactions of a top quark, a gluon and an up or charm quark. Two production processes are considered: $u + g \rightarrow t$ and $c + g \rightarrow t$. The analysis is based on proton–proton collision data taken at a centre-of-mass energy of 13 TeV with the ATLAS detector at the LHC. The data set corresponds to an integrated luminosity of 139 fb^{-1} . Events with exactly one electron or muon, exactly one b -tagged jet and missing transverse momentum are selected, resembling the decay products of a singly produced top quark. Neural networks based on kinematic variables differentiate between events from the two signal processes and events from background processes. The measured data are consistent with the background-only hypothesis, and limits are set on the production cross-sections of the signal processes: $\sigma(u + g \rightarrow t) \times \mathcal{B}(t \rightarrow Wb) \times \mathcal{B}(W \rightarrow \ell\nu) < 3.0 \text{ pb}$ and $\sigma(c + g \rightarrow t) \times \mathcal{B}(t \rightarrow Wb) \times \mathcal{B}(W \rightarrow \ell\nu) < 4.7 \text{ pb}$ at the 95% confidence level, with $\mathcal{B}(W \rightarrow \ell\nu) = 0.325$ being the sum of branching ratios of all three leptonic decay modes of the W boson. Based on the framework of an effective field theory, the cross-section limits are translated into limits on the strengths of the tug and tcg couplings occurring in the theory: $|C_{uG}^{ut}|/\Lambda^2 < 0.057 \text{ TeV}^{-2}$ and $|C_{uG}^{ct}|/\Lambda^2 < 0.14 \text{ TeV}^{-2}$. These bounds correspond to limits on the branching ratios of FCNC-induced top-quark decays: $\mathcal{B}(t \rightarrow u + g) < 0.61 \times 10^{-4}$ and $\mathcal{B}(t \rightarrow c + g) < 3.7 \times 10^{-4}$.

Contents

1	Introduction	1
2	The ATLAS detector	2
3	Samples of data and simulated events	3
3.1	Samples of simulated events from the ugt and cgt FCNC processes	3

3.2	Simulation of $t\bar{t}$ and SM single-top-quark production	4
3.3	Simulation of W +jets and Z +jets production	4
3.4	Simulation of diboson and multijet production	5
4	Object reconstruction and event selection	5
4.1	Object definitions	5
4.2	Basic event selection	6
4.3	Definition of signal and validation regions	7
5	Estimation of the multijet background	8
6	Neural networks separating signal and background events	9
7	Systematic uncertainties	11
7.1	Experimental uncertainties	11
7.2	Modelling uncertainties	12
8	Results	14
8.1	Results of the profile likelihood fit	14
8.2	Upper limits on cross-sections, EFT coefficients and branching ratios	16
8.3	Comparison of expected upper limits	17
9	Conclusions	18
	References	19

1 Introduction

Direct searches for on-shell production of new heavy particles at the Large Hadron Collider (LHC) have not yet been successful. For this reason, indirect searches targeting non-standard couplings among Standard Model (SM) particles attract increasing interest. Among these analyses are searches for flavour-changing neutral-current (FCNC) processes in the top-quark sector. The SM does not contain FCNC processes at tree level, and even though these processes exist at higher orders, they are suppressed due to the Glashow–Iliopoulos–Maiani mechanism [1]. Compared to the b -quark sector, where decays of b -hadrons via FCNCs were first observed in 1995 [2], FCNC decays of top quarks are even more suppressed. Depending on the decay mode, FCNC branching ratios (\mathcal{B}) of the top quark are predicted to range from 10^{-12} to 10^{-17} [3], and are thus well below the

* e-mail: atlas.publications@cern.ch

experimentally accessible regime, at present and in the foreseeable future. The observation of FCNC top-quark decays or top-quark production via FCNCs would therefore be an unambiguous signal of physics beyond the SM.

Many extensions of the SM predict significantly higher rates for FCNC processes in the top-quark sector. These extensions include new scalar particles introduced in two-Higgs-doublet models [4,5] or in supersymmetry [6–8]. In certain regions of the parameter space of these models, the predicted branching ratios of top quarks decaying via FCNC can be as large as 10^{-5} to 10^{-3} and thus become detectable at the LHC.

Searches for FCNCs involving a top quark and a gluon were performed at the Tevatron [9,10] and in data from Run 1 of the LHC [11–13]. Rather than looking for the top-quark decays $t \rightarrow u + g$ and $t \rightarrow c + g$ in top-quark–antiquark pair ($t\bar{t}$) production, these analyses searched for the production of a single top quark (t) via the FCNC processes $u + g \rightarrow t$ (ugt process) and $c + g \rightarrow t$ (cgt process), exploiting specific kinematic features of single-top-quark production to separate a potential signal from the large W +jets and multijet backgrounds. The analysis presented in this paper extends the Run 1 ATLAS search to the Run 2 data set collected with the ATLAS detector in the years 2015 to 2018, during which the LHC operated at a centre-of-mass energy of 13 TeV. Conceptually, the scope of the analysis is expanded by performing independently optimised searches for the ugt and cgt processes. Differences between these two processes are due to differences in the parton distribution functions (PDFs) for valence and sea quarks. For top antiquarks the charge-conjugate processes are implied. The FCNC interaction is assumed to be left-handed. Another novelty compared to the Run 1 analysis is the interpretation of the results in an effective field theory framework provided by the T_{OPFCNC} model [14].

The event selection targets the $t \rightarrow e^+ \nu b$ and $t \rightarrow \mu^+ \nu b$ decay modes of the top quark. However, there is also additional but lower acceptance for events with the decay $t \rightarrow \tau^+ \nu b$ and the subsequent decay of the τ -lepton into $e^+ \nu_e \bar{\nu}_\tau$ or $\mu^+ \nu_\mu \bar{\nu}_\tau$. A leading-order (LO) Feynman diagram illustrating the signature of the targeted scattering events is shown in Fig. 1.

Considering the signature of the signal events, the required reconstructed objects are exactly one charged-lepton candidate (an electron or a muon) with high transverse momentum (p_T), exactly one jet which is identified to originate with a high probability from a b -quark, and large missing transverse momentum as an indication of a high- p_T neutrino.

The main background processes are $W + b\bar{b}$ production, t -channel single-top-quark (tq) production, $t\bar{t}$ production and multijet production. Artificial neural networks (NNs) are used to separate signal events from background events. The observed distributions of the NN discriminants are analysed

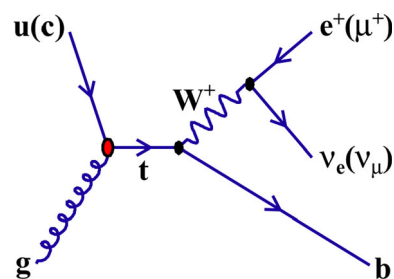


Fig. 1 Leading-order Feynman diagram of non-SM production of a single top quark via the FCNC process $u(c) + g \rightarrow t$

statistically with a profile maximum-likelihood fit in which all systematic uncertainties are treated as nuisance parameters.

The structure of the paper is as follows. A brief description of the ATLAS detector is given in Sect. 2, followed by a comprehensive summary of the collision data and the samples of simulated events in Sect. 3. Section 4 describes the reconstruction of detector-level objects and the event selection. The modelling of multijet background events and the estimation of their rate is discussed in Sect. 5. Section 6 provides details about the separation of signal and background events using NNs. Systematic uncertainties are outlined in Sect. 7 and the results are presented in Sect. 8. Conclusions are given in Sect. 9.

2 The ATLAS detector

The ATLAS detector [15] at the LHC covers nearly the entire solid angle around the collision point.¹ It consists of an inner tracking detector surrounded by a thin superconducting solenoid, electromagnetic and hadronic calorimeters, and a muon spectrometer incorporating three large superconducting toroidal magnets.

The inner-detector system (ID) is immersed in a 2T axial magnetic field and provides charged-particle tracking in the range $|\eta| < 2.5$. The high-granularity silicon pixel detector covers the vertex region and typically provides four measurements per track, the first hit normally being in the insertable B-layer installed before Run 2 [16,17]. It is followed by the silicon microstrip tracker, which usually provides eight measurements per track. These silicon detectors are complemented by the transition radiation tracker (TRT),

¹ ATLAS uses a right-handed coordinate system with its origin at the nominal interaction point (IP) in the centre of the detector and the z -axis along the beam pipe. The x -axis points from the IP to the centre of the LHC ring, and the y -axis points upwards. Cylindrical coordinates (r, ϕ) are used in the transverse plane, ϕ being the azimuthal angle around the z -axis. The pseudorapidity is defined in terms of the polar angle θ as $\eta = -\ln \tan(\theta/2)$. Angular distance is measured in units of $\Delta R \equiv \sqrt{(\Delta\eta)^2 + (\Delta\phi)^2}$.

which enables radially extended track reconstruction up to $|\eta| = 2.0$. The TRT also provides electron identification information based on the fraction of hits (typically 30 in total) above a higher energy-deposit threshold corresponding to transition radiation.

The calorimeter system covers the pseudorapidity range $|\eta| < 4.9$. Within the region $|\eta| < 3.2$, electromagnetic calorimetry is provided by barrel and endcap high-granularity lead/liquid-argon (LAr) calorimeters, with an additional thin LAr presampler covering $|\eta| < 1.8$ to correct for energy loss in material upstream of the calorimeters. Hadronic calorimetry is provided by the steel/scintillator-tile calorimeter, segmented into three barrel structures within $|\eta| < 1.7$, and two copper/LAr hadronic endcap calorimeters. The solid angle coverage is completed with forward copper/LAr and tungsten/LAr calorimeter modules optimised for electromagnetic and hadronic measurements respectively.

The muon spectrometer (MS) comprises separate trigger and high-precision tracking chambers measuring the deflection of muons in a magnetic field generated by superconducting air-core toroids. The field integral of the toroids ranges between 2.0 and 6.0 T m across most of the detector. A set of precision chambers covers the region $|\eta| < 2.7$ with three layers of monitored drift tubes, complemented by cathode-strip chambers in the forward region, where the background is highest. The muon trigger system covers the range $|\eta| < 2.4$ with resistive-plate chambers in the barrel, and thin-gap chambers in the endcap regions. Interesting events are selected to be recorded by the first-level trigger system implemented in custom hardware, followed by selections made by algorithms implemented in software in the high-level trigger [18]. The first-level trigger accepts events from the 40 MHz bunch crossings at a rate below 100 kHz, which the high-level trigger reduces in order to record events to disk at about 1 kHz.

An extensive software suite [19] is used in the reconstruction and analysis of real and simulated data, in detector operations, and in the trigger and data acquisition systems of the experiment.

3 Samples of data and simulated events

The analysis uses proton–proton (pp) collision data recorded with the ATLAS detector in the years 2015 to 2018 at a centre-of-mass energy of 13 TeV. After applying data-quality requirements [20], the data set corresponds to an integrated luminosity of 139 fb^{-1} with a relative uncertainty of 1.7% [21]. The LUCID-2 detector [22] was used for the primary luminosity measurements. At the high instantaneous luminosity reached at the LHC, events were affected by additional inelastic pp collisions in the same and neighbouring bunch

crossings (pile-up). The average number of interactions per bunch crossing was 33.7.

Events were selected online during data taking by single-electron or single-muon triggers [23, 24]. Multiple triggers were used to increase the selection efficiency. The lowest-threshold triggers utilised isolation requirements for reducing the trigger rate. The isolated-lepton triggers had p_T thresholds of 20 GeV for muons and 24 GeV for electrons in 2015 data, and 26 GeV for both lepton types in 2016, 2017 and 2018 data. They were complemented by other triggers with higher p_T thresholds but no isolation requirements in order to increase the trigger efficiency.

Large sets of simulated events from signal and background processes were produced with event generator programs based on the Monte Carlo (MC) method to model the recorded and selected data. After event generation, the response of the ATLAS detector was simulated using the GEANT4 toolkit [25] with a full detector model [26] or a fast simulation [27, 28] which employed a parameterisation of the calorimeter response. To account for pile-up effects, minimum-bias interactions were superimposed on the hard-scattering events and the resulting events were weighted to reproduce the observed pile-up distribution. The minimum-bias events were simulated using PYTHIA 8.186 [29] with the A3 [30] set of tuned parameters and the NNPDF2.3LO PDF set [31]. Finally, the simulated events were reconstructed using the same software as applied to the collision data. Except for the multijet background, the same event selection requirements were applied and the selected events were passed through the same analysis chain. Small corrections were applied to simulated events such that the lepton trigger and reconstruction efficiencies, jet energy calibration and b -tagging efficiency were in better agreement with the response observed in data. More details of the simulated event samples are provided in the following subsections.

3.1 Samples of simulated events from the ugt and cgt FCNC processes

Simulated events from the ugt and cgt processes were produced with the METOP 1.0 event generator [32, 33] at next-to-leading order (NLO) in quantum chromodynamics (QCD). The difference between LO and NLO is very relevant for the analysis since a veto on a second jet is applied in the event selection by requiring exactly one reconstructed jet with $p_T > 30 \text{ GeV}$. Signal samples generated at NLO predict a higher rate of events with two jets than samples generated at LO, leading to a lower acceptance for signal events due to the jet veto. The Lorentz structure of the vertex coupling was taken to be left-handed. It was verified that the shapes of kinematic distributions are independent of the value of the coupling constant used for the event generation. The top quark was assumed to decay as in the SM and the decay was

simulated using MADSPIN [34,35]. Only leptonic decays of the W boson originating from top-quark decay were considered, including e^\pm , μ^\pm and τ^\pm leptons. The renormalisation scale μ_r and the factorisation scale μ_f were set to the top-quark mass m_t , for which a value of $m_t = 172.5$ GeV was used. The CT10 set of PDFs [36] was used for event generation. Parton showers and the hadronisation were simulated with PYTHIA 8.235 [37] with the A14 set of tune parameters [38]. In the METOP + PYTHIA set-up, hard gluon emissions can arise in both the NLO matrix-element generator and the parton-shower generator. The matching between the two generators was achieved by limiting the phase-space region of the first parton-shower emission in a way that depends on the transverse momentum of the top quark. The matching scale between the matrix-element generator and the parton shower was set to 10 GeV.

Samples with alternative generator settings were produced to estimate systematic uncertainties. Samples with $\mu_r = \mu_f = 2 \cdot m_t$ and $\mu_r = \mu_f = 0.5 \cdot m_t$ were used to evaluate the impact of the scale choice on the signal model. The uncertainty in modelling parton showers was evaluated with METOP signal samples in which parton showers were generated by HERWIG7.0.4 [39,40] instead of PYTHIA. The METOP + HERWIG set-up used the same PDF set as the nominal sample, CT10. In addition, METOP + PYTHIA samples with a different matching scale of 15 GeV were produced to evaluate the uncertainties due to the choice of this scale. All samples of the ugt and cgt processes were passed through the fast detector simulation.

3.2 Simulation of $t\bar{t}$ and SM single-top-quark production

Samples of simulated events from $t\bar{t}$ and single-top-quark production were generated using the POWHEG BOXv2 [41–47] NLO matrix-element generator, setting $m_t = 172.5$ GeV. For $t\bar{t}$ and tW production as well as s -channel single-top-quark production ($t\bar{b}$ production) the NNPDF3.0NLO PDF set [48] implementing the five-flavour scheme was used, while t -channel single-top-quark events (tq production) were produced with the NNPDF3.0NLO_nf4 PDF set, which implements the four-flavour scheme, following a recommendation given in Ref. [47]. Parton showers, hadronisation, and the underlying event were modelled using PYTHIA 8.230 with the A14 set of tuned parameters and the NNPDF2.3LO PDF set. The POWHEG BOX + PYTHIA generator set-up applies a matching scheme to the modelling of hard emissions in the two programs. The matrix-element-to-parton-shower matching is steered by the h_{damp} parameter, which controls the p_T of the first additional gluon emission beyond the LO Feynman diagram in the parton shower and therefore regulates the high- p_T emission against which the $t\bar{t}$ system recoils. Event generation was run with $h_{\text{damp}} = 1.5 \times m_t$ [49]. The renormalisation and factorisation scales were set dynamically on

an event-by-event basis, namely to $\mu_r = \mu_f = \sqrt{m_t^2 + p_T^2(t)}$ for $t\bar{t}$ production and to $\mu_r = \mu_f = 4\sqrt{m_b^2 + p_T^2(b)}$ for tq production, with $p_T(t)$ being the p_T of the top quark and $p_T(b)$ being the p_T of the b -quark originating from the initial-state gluon, splitting into a $b\bar{b}$ pair. The scale choice for tq production followed a recommendation of Ref. [47]. When generating tW events, the diagram-removal scheme [50] was employed to handle the interference with $t\bar{t}$ production [49].

In the case of $t\bar{t}$ production, top-quark decays were handled by POWHEG BOX directly, while in the case of single-top-quark production, top-quark decays were modelled by MADSPIN. The decays of bottom and charm hadrons were simulated using the EVTGEN 1.6.0 program [51] for all samples involving top-quark production.

The $t\bar{t}$ production cross-section was scaled to $\sigma(t\bar{t}) = 832_{-51}^{+47}$ pb, the value obtained from next-to-next-to-leading-order (NNLO) predictions from the TOP++ 2.0 program (see Ref. [52] and references therein), which includes the resummation of next-to-next-to-leading logarithmic (NNLL) soft-gluon terms. The total cross-sections for tq and $t\bar{b}$ production were computed at NLO in QCD with the HATHOR v2.1 program [53,54] and the corresponding samples of simulated events were scaled to the following values: $\sigma(tq) = 136.0_{-4.7}^{+5.5}$ pb, $\sigma(t\bar{q}) = 81.0_{-3.7}^{+4.1}$ pb and $\sigma(t\bar{b} + \bar{t}b) = 10.3 \pm 0.38$ pb. The cross-section used for normalising the tW sample is $\sigma(tW + \bar{t}W) = 71.7 \pm 3.8$ pb [55,56]. All cross-section calculations assumed $m_t = 172.5$ GeV as a fixed value.

3.3 Simulation of W +jets and Z +jets production

The production of W bosons and Z bosons in association with jets, including heavy-flavour jets in particular, was simulated with the SHERPA 2.2.1 generator [57]. In this set-up, NLO-accurate matrix elements for up to two partons and LO-accurate matrix elements for up to four partons were calculated with the COMIX [58] and OPENLOOPS1 [59–61] libraries. The default SHERPA parton shower [62] based on Catani–Seymour dipole factorisation and the cluster hadronisation model [63] were used. The generation employed the dedicated set of tuned parameters developed by the SHERPA authors and the NNPDF3.0NLO PDF set.

The NLO matrix elements of a given jet multiplicity were matched to the parton shower using a colour-exact variant of the MC@NLO algorithm [64]. Different jet multiplicities were then merged into an inclusive sample using an improved CKKW matching procedure [65,66] which was extended to NLO accuracy using the MEPS@NLO prescription [67]. The merging threshold was set to 20 GeV. The W +jets and Z +jets samples were normalised to NNLO predictions [68] of the total cross-sections, obtained with the FEWZ package [69].

3.4 Simulation of diboson and multijet production

Samples of on-shell diboson production (WW , WZ and ZZ) were also simulated with the SHERPA 2.2.1 generator. Motivated by the targeted signature of the signal events, only semileptonic final states were produced, in which one boson decayed leptonically and the other hadronically. The considered matrix elements contain all diagrams with four electroweak vertices and they were calculated at NLO accuracy in QCD for up to one additional parton and at LO accuracy for up to three additional parton emissions. The matching of NLO matrix elements to the parton shower and the merging of different jet multiplicities was done in the same way as for W/Z +jets production. Virtual QCD corrections were provided by the OPENLOOPS1 library. The NNPDF3.0NLO PDF set was used along with the dedicated set of tuned parameters developed by the SHERPA authors. The diboson event samples were normalised to the total cross-sections provided by SHERPA at NLO in QCD.

Events featuring generic high- p_T multijet production may pass the event selection if a jet is misidentified as an electron or muon, or if real electrons or muons coming from hadron decays inside the jets pass the isolation requirements. The former are called *fake leptons*, the latter *non-prompt leptons*. In addition, non-prompt electrons occur as a result of photon conversions in the detector material. Multijet events with fake electrons or non-prompt electrons were modelled with a sample of simulated dijet events, while events with non-prompt muons were modelled with collision data. The number of events with fake muons is negligible. The dijet event sample was generated using PYTHIA 8.186 with LO matrix elements for dijet production and interfaced to a p_T -ordered parton shower. The scales μ_r and μ_f were set to the square root of the geometric mean of the squared transverse masses of the two outgoing particles in the matrix element, $\mu_r = \mu_f = \sqrt{(p_{T,1}^2 + m_1^2)(p_{T,2}^2 + m_2^2)}$. At generator level, a filter was applied which required the existence of one particle-level jet with $p_T > 17$ GeV. The generation used the NNPDF2.3LO PDF set and the A14 set of tuned parameters. The generated sample of dijet events was used to model the event kinematics and to produce template distributions in the electron channel, while the rate of the multijet background was estimated in a data-driven way as described in Sect. 5.

4 Object reconstruction and event selection

The hard-scattering process was reconstructed by identifying the particles occurring at parton level with objects which were reconstructed at detector level, such as electron and muon candidates and hadronic jets. The presence of high- p_T neutrinos is signalled by high missing transverse momentum.

4.1 Object definitions

Events were required to have at least one vertex reconstructed from at least two ID tracks with transverse momenta of $p_T > 0.5$ GeV. The primary vertex of an event was defined as the vertex with the highest sum of p_T^2 over all associated ID tracks [70].

Electron candidates were reconstructed from clusters of energy deposited in the electromagnetic calorimeter with a matched track reconstructed in the ID [71]. The pseudorapidity of clusters, η_{cluster} , was required to be in the range $|\eta_{\text{cluster}}| < 2.47$. However, clusters were excluded if they are in the transition region $1.37 < |\eta_{\text{cluster}}| < 1.52$ between the central and the endcap electromagnetic calorimeters. Electron candidates had to have $p_T > 10$ GeV. A likelihood-based method was used to simultaneously evaluate several properties of electron candidates, including shower shapes in the electromagnetic calorimeter, track quality, and detection of transition radiation produced in the TRT. Two categories of electrons with different quality were defined [71]: the first category implemented *Tight* identification criteria and featured a high rejection of non-prompt or fake electrons, while the second category with *Loose* criteria had higher efficiency at the price of lower purity in prompt electrons. Electrons from decays of weak gauge bosons pass the *Tight* criteria with an average efficiency of 80% and the *Loose* criteria with 93%.

Muon candidates were reconstructed by combining tracks in the MS with tracks in the ID [72]. The tracks had to be in the range of $|\eta| < 2.5$ and have $p_T > 10$ GeV. Similarly to electrons, two levels of identification criteria were applied, defining *Medium* and *Loose* quality categories of muon candidates. Muons originating from W bosons in $t\bar{t}$ events with $p_T > 10$ GeV pass the *Medium* quality criteria with an efficiency of 97% and the *Loose* criteria with 99%.

The tracks matched to electron and muon candidates had to point to the primary vertex, which was ensured by requirements imposed on the transverse impact-parameter significance, $|d_0/\sigma(d_0)| < 5.0$ for electrons and $|d_0/\sigma(d_0)| < 3.0$ for muons, and the longitudinal impact parameter, $|z_0 \sin(\theta)| < 0.5$ mm for both lepton flavours. Isolated *Tight* electrons and *Medium* muons were selected by requiring the amount of energy in nearby energy depositions in the calorimeters and the scalar sum of the transverse momenta of nearby tracks in the ID to be small. Isolation requirements were not imposed on electrons and muons of *Loose* quality. Scale factors were used to correct the efficiencies in simulation in order to match the efficiencies measured for the electron [71] and muon [24] triggers, and the reconstruction, identification and isolation criteria.

Jets were reconstructed from topological clusters [73, 74] in the calorimeters with the anti- k_r algorithm [75] using Fast-Jet [76] and a radius parameter of 0.4. Their energy was

calibrated [77], and they had to fulfil $p_T > 20$ GeV and $|\eta| < 4.5$. Jets with $p_T < 120$ GeV and $|\eta| < 2.5$ were required to pass a requirement on the jet-vertex-tagger (JVT) discriminant [78] to suppress jets originating from pile-up collisions. The JVT-discriminant was required to be above 0.59, which corresponds to an efficiency of 92% for non-pile-up jets. Similarly, a forward-JVT (fJVT) requirement was used for jets with $p_T < 60$ GeV and $2.5 < |\eta| < 4.5$ [79]. Differences in the efficiencies of the JVT and fJVT requirements between collision data and simulation were accounted for by corresponding scale factors.

Jets containing b -hadrons were identified (b -tagged) with the MV2c10 algorithm [80], which used boosted decision tree discriminants with several b -tagging algorithms as inputs [81]. The algorithms exploited the impact parameters of charged-particle tracks, the properties of reconstructed secondary vertices and the topology of b - and c -hadron decays inside the jets. In order to strongly reduce the misidentification rate of c -jets and light-flavour (u , d or s)/gluon jets, a specific working point of the MV2c10 algorithm was defined and calibrated, using the standard calibration technique [80]. With this working point, the b -tagging efficiency for jets that originate from the hadronisation of b -quarks is 30% in simulated $t\bar{t}$ events. The b -tagging rejection² for jets that originate from the hadronisation of c -quarks (u -, d -, s -quarks or gluons) is 900 (30,000). By using the high-purity b -tagging working point with 30% efficiency for b -jets the analysis performance was considerably improved in comparison to an analysis based on the tightest standard working point which features a tagging efficiency of 60% for b -jets. The improvement is mainly due to a reduced impact of the W +jets background, including uncertainties in mistagging c -quark jets, light-flavour jets and gluon jets in W +jets production. Differences in b -tagging efficiency between simulated and collision events were corrected for by applying a p_T -dependent scale factor to simulated events. The scale factor ranges from 0.96 ± 0.04 in the interval $30 < p_T(b) \leq 40$ GeV to 1.01 ± 0.02 for $140 < p_T(b) < 175$ GeV, which is the highest calibration interval relevant for this analysis. The b -tagging scale factors were obtained by comparing samples of collision data strongly enriched in $t\bar{t}$ events with samples of simulated events generated by POWHEG+PYTHIA 8.230. The obtained scale factors depend on the parton-shower generator used to produce the $t\bar{t}$ samples. When using samples with a different parton-shower generator, for example SHERPA to model W +jets events, or when evaluating systematic uncertainties with a set-up based on HERWIG, additional correction factors called MC-to-MC scale factors were applied.

To avoid double-counting objects satisfying more than one selection criterion, a procedure called *overlap removal* was applied. Reconstructed objects defined with *Loose* quality

criteria were removed in the following order: electrons sharing an ID track with a muon; jets within $\Delta R = 0.2$ of an electron, thereby avoiding double-counting electron energy deposits as jets; electrons within $\Delta R = 0.4$ of a remaining jet, for reducing the impact of non-prompt electrons; jets within $\Delta R = 0.2$ of a muon if they have two or fewer associated tracks; muons within $\Delta R = 0.4$ of a remaining jet, reducing the rate of non-prompt muons. The *Tight* and *Medium* criteria were applied to those objects which survived overlap removal.

The missing transverse momentum \vec{p}_T^{miss} was reconstructed as the negative vector sum of the p_T of the reconstructed leptons and jets, as well as ID tracks that pointed to the primary vertex but were not associated with a reconstructed object [82]. The magnitude of \vec{p}_T^{miss} is denoted by E_T^{miss} .

4.2 Basic event selection

To be selected, events were required to have exactly one electron of *Tight* quality or exactly one muon of *Medium* quality, both with $p_T > 27$ GeV. The charged lepton was required to match the object which triggered the event. To reduce contributions from $t\bar{t}$ events in the dilepton decay channel, any event with an additional lepton satisfying the *Loose* quality conditions with $p_T > 10$ GeV was rejected (dilepton veto).

Multijet events containing fake or non-prompt leptons tend to have, in contrast to events with prompt leptons from W and Z decays, low E_T^{miss} and low W transverse mass, which is defined as

$$m_T(W) = \sqrt{2p_T(\ell)E_T^{\text{miss}}(1 - \cos \Delta\phi(\ell, \vec{p}_T^{\text{miss}}))}. \quad (1)$$

To reduce the multijet background, $E_T^{\text{miss}} > 30$ GeV and $m_T(W) > 50$ GeV were applied as additional selection requirements.

At least one jet with $p_T > 30$ GeV was required. In order to even further suppress the multijet background and to remove poorly reconstructed leptons with low p_T , the event selection applied an additional requirement based on the azimuthal angle between the primary lepton (ℓ) and the leading jet (j_1), i.e. the jet with the largest p_T . This quantity is denoted by $\Delta\phi(j_1, \ell)$. The imposed requirement was

$$p_T(\ell) > 50 \text{ GeV} \cdot \left(1 - \frac{\pi - |\Delta\phi(j_1, \ell)|}{\pi - 1}\right),$$

which led to a tighter p_T requirement on the charged lepton if the leading jet and the lepton had a back-to-back topology, namely if $|\Delta\phi(j_1, \ell)| > 0.687\pi$. For the maximum separation $|\Delta\phi(j_1, \ell)| = \pi$ between the two objects, $p_T(\ell) > 50$ GeV had to be satisfied.

² The rejection is defined as the inverse of the efficiency.

4.3 Definition of signal and validation regions

A signal region (SR) and three validation regions (VRs) were defined by applying further requirements to the sample of events passing the basic selection. Only events in the SR were used at a later stage of the analysis for a profile-likelihood fit to the data in the search for a signal contribution, while the VRs were used to validate the modelling of different background contributions. A summary of the selection requirements used to define the four analysis regions is given in Table 1.

All requirements mentioned before are common to all regions considered. The SR was defined by narrowing the jet requirement relative to the basic event selection. Each event had to have exactly one jet with $p_T > 30 \text{ GeV}$ and $|\eta| < 2.5$, i.e. events with additional central jets were vetoed. This single jet had to be b -tagged. The selection efficiency for signal events in which the top quark decays into Wb and the resulting W boson decays leptonically was 1.36% for ugt events and 2.30% for cgt events. For the ugt search, the SR was split according to the sign of the charge of the primary lepton $\text{sgn}q(\ell)$. Two NN discriminants D_1 and D_2 , described in Sect. 6, were formed to separate signal and background events in these three SRs.

The first VR was defined for validating the modelling of the events kinematics of W +jets production (W +jetsVR) by the SHERPA 2.2.1 generator. To suppress top-quark backgrounds a less stringent b -tagging requirement was used. Exactly one jet with $p_T > 30 \text{ GeV}$ was required to be b -

tagged at a working point with an efficiency of 60%. All other selection requirements were the same as for the SR. However, events in the SR were vetoed. The modified b -tagging requirement leads to a different flavour composition of the jets in the W +jetsVR compared to the SR; the components of $W+c$ -jets and W +light-flavour jets are increased relative to $W+b$ -jets. To enrich the region further in W +jets events and reduce the number of signal events, the NN discriminant D_1 , specified in Sect. 6, was required to be in the range $0.3 < D_1 < 0.6$. The modelling of events with positive lepton charge was separately checked by requiring the NN discriminant D_2 to be in the range $0.3 < D_2 < 0.6$, defining the ℓ^+ W +jetsVR. When normalising the FCNC processes to the observed limits from the previous ATLAS results obtained at a centre-of-mass energy of 8 TeV, the FCNC signal contamination is 1.2% in the W +jetsVR and 0.9% in the ℓ^+ W +jetsVR.

The second VR was enriched in $t\bar{t}$ events by selecting events with exactly two b -tagged jets using the 30% b -tagging working point ($t\bar{t}$ VR). When normalising the FCNC processes to the observed limits from the previous ATLAS results obtained at a centre-of-mass energy of 8 TeV, the FCNC signal contamination is at a very low level of a few times 10^{-4} . The third VR checked the modelling of tq events (tq VR). Events with exactly two jets were required. Exactly one of the jets had to be b -tagged at the 30% efficiency working point, while the second jet was required to be in the forward region with $|\eta| > 2.5$, which is a characteristic feature of tq events. Thus, the tq VR was a subset of the SR, since

Table 1 Summary of selection requirements used to define the four analysis regions. The left column lists the observables on which the requirements are based. The first part of the table lists requirements which are common to all four analysis regions and define the basic event selection described in Sect. 4.2. Tight electrons and medium muons were counted based on a p_T threshold of 27 GeV and they are a subset of the

corresponding Loose quality category. Loose charged leptons had to exceed a threshold of $p_T(\ell) = 10 \text{ GeV}$. The transverse mass of the W boson, $m_T(W)$, is defined in Eq. (1). The efficiency of the b -tagging working point used to identify b -jets is denoted by ϵ_b . The symbol D_1 represents one of the NN discriminants defined in Sect. 6

Observable	Common requirements			
$n_{\text{Tight}}(e) + n_{\text{Medium}}(\mu)$	= 1			
$n_{\text{Loose}}(e) + n_{\text{Loose}}(\mu)$	= 1			
E_T^{miss}	> 30 GeV			
$m_T(W)$	> 50 GeV			
$n(j)$	≥ 1			
$p_T(\ell)$	$> 50 \text{ GeV} \cdot \left(1 - \frac{\pi - \Delta\phi(j_1, \ell) }{\pi - 1}\right)$			
	Analysis regions			
	SR	W +jetsVR	$t\bar{t}$ VR	tq VR
$n(\eta(j) < 2.5)$	= 1	= 1	= 2	= 1
$n(b)$	= 1	= 1	= 2	= 1
ϵ_b	30%	60% (veto 30%)	30%	30%
$n(\eta(j) > 2.5)$	≥ 0	≥ 0	≥ 0	= 1
$D_{1(2)}$	–	$0.3 < D_{1(2)} < 0.6$	–	$0.2 < D_{1(2)} < 0.4$

there was no condition on jets in the forward region when defining the SR. To further enhance the fraction of tq events and to suppress signal events, the NN discriminant D_1 was required to be in the range $0.2 < D_1 < 0.4$. The modelling of events with positive lepton charge was separately checked by requiring the NN discriminant D_2 to be in the range $0.2 < D_2 < 0.4$, defining the $\ell^+ tq$ VR. When normalising the FCNC processes to the observed limits from the previous ATLAS results obtained at a centre-of-mass energy of 8 TeV, the FCNC signal contamination is 1.2% in the tq VR (cgt analysis) and 0.8% in the $\ell^+ tq$ VR.

5 Estimation of the multijet background

By requiring electron and muon candidates to be isolated, the object definition and the event selection strongly favour prompt leptons originating from decays of W bosons or Z bosons. However, there is a small probability for non-prompt electrons or muons occurring in hadron decays, either directly or through the decay of a τ -lepton, to be reconstructed as isolated leptons. The main source is b -hadron decays in jets, but c -hadrons and long-lived weakly decaying states such as π^\pm and K mesons also contribute. In addition, prompt electrons are mimicked by *fake electrons* which arise from the misidentification of direct photons, photons from π^0 decays, or bremsstrahlung and photon conversions. Even though the probabilities of misidentification are relatively low, some multijet events still pass the selection and contribute to the background, since their production cross-section is approximately three orders of magnitude higher than the cross-sections of top-quark production processes. As the mechanisms of misidentification are not well modelled by the detector simulation, the rate of the multijet background was determined in a data-driven way by fitting the E_T^{miss} distribution for events with an electron (electron channel) and the $m_T(W)$ distribution for events with a muon (muon channel).

In the electron channel, the multijet background was modelled using the *jet-electron* method [83]. Simulated events from dijet production (see Sect. 3.4 for a description of the sample) were selected if they contained a jet depositing a large fraction (>80%) of its energy in the electromagnetic calorimeter. This jet was classified as an electron, the jet-electron, and treated in the subsequent steps of the analysis in the same way as a properly identified prompt electron. The jet-electrons had to pass the nominal p_T and $|\eta|$ requirements, but electron identification requirements were not applied. Since the relative numbers of electrons detected in the barrel ($|\eta| < 1.37$) and endcap ($|\eta| > 1.52$) sections of the electromagnetic calorimeter were not modelled well enough by the sample of simulated dijet events, the electron

channel was divided into two subchannels: a barrel-electron channel and an endcap-electron channel.

In the muon channel, multijet events were modelled with collision events highly enriched in non-prompt muons [83]. Starting from the same sample of collision events as the nominal selection, a subset of events enriched in non-prompt muons was obtained by inverting or modifying some of the muon isolation requirements, such that the resulting sample did not overlap with the nominal sample. The kinematic requirements on muon p_T and $|\eta|$ remained the same as for the nominal selection.

The rate of the multijet background was normalised by performing a binned maximum-likelihood fit to the E_T^{miss} and $m_T(W)$ distributions observed in the electron and muon channels, respectively. All selection criteria were applied, except for the E_T^{miss} requirement in the electron channels (barrel and endcap) and the requirement on $m_T(W)$ in the muon channel. The three channels were further split according to the sign of the charge of the primary lepton $\text{sgn}(\ell)$, leading to six channels per analysis region. Separate fits were performed for the SR and the three VRs. In each region, all six channels were fit simultaneously. Since the multijet background is expected to be independent of lepton charge, its rates in the ℓ^+ and the ℓ^- channels were assumed to be the same. On the other hand, the rates of some of the other background processes, i.e. tq , $t\bar{b}$ and W +jets production, are different in the ℓ^+ and the ℓ^- channels due to the PDFs. For the purpose of these fits, scattering processes other than multijet production were grouped in the following way: (1) *top-quark production* comprises $t\bar{t}$ production and all three single-top-quark production processes (tq , $t\bar{b}$ and tW production), (2) W +jets production, including the production of light-quark, gluon, b -quark and c -quark jets in association with a W boson, and (3) Z +jets and diboson production (WW , WZ and ZZ production). The templates of the fit distributions for these three groups of processes were derived from simulated events and the rates were normalised to the theory predictions reported in Sect. 3. As the shapes of the distributions for Z +jets and diboson production are very similar to those of W +jets production, the rates of Z +jets and diboson production were fixed in the fitting process to the values predicted by simulation. Uncertainties in the normalisation of top-quark production and W +jets production were accounted for by Gaussian constraints on the normalisation factors of these groups of processes. In the W +jetsVR, only the rate of W +jets production was varied, while the top-quark background was fixed. Similarly, in the $t\bar{t}$ VR and tq VR only the rate of top-quark production was varied, while the rate of W +jets production was fixed. In the SR, both rates were free to vary within uncertainties.

The fits yielded estimates of the rates of the multijet background in the four analysis regions before applying

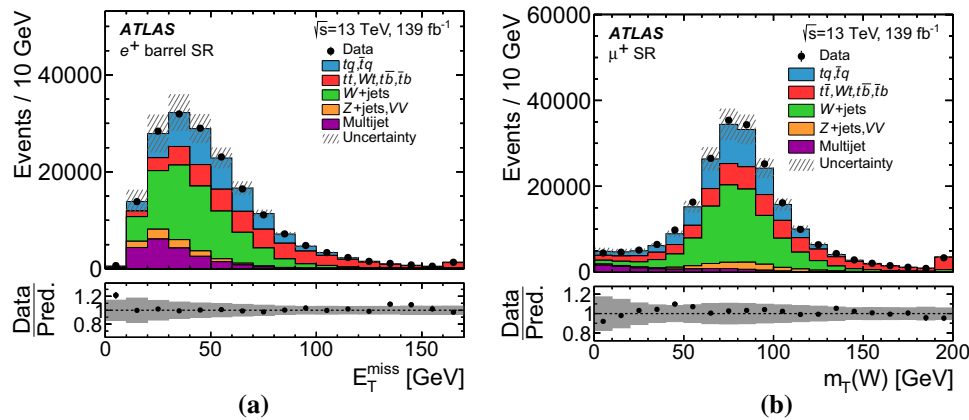


Fig. 2 Illustration of the estimation of the multijet background by fitting the E_T^{miss} and $m_T(W)$ distributions in the analysis regions. As representative examples, the E_T^{miss} distribution is shown in the e^+ barrel channel in (a) and the $m_T(W)$ distribution is shown in the μ^+ channel in (b). Both distributions are in the SR. The stacked histograms were normalised to the fit result. The uncertainty band represents the

uncertainty due to limited sample size and the rate uncertainties of the different processes (20% for W +jets production, 30% for the multijet background and 6% for the top-quark processes). The ratio of observed to predicted (Pred.) numbers of events in each bin is shown in the lower panel. Events beyond the axis range are included in the last bin

the requirements on E_T^{miss} and $m_T(W)$. An uncertainty of 30% was assigned to the estimates, covering alternative results obtained in studies of fits to different discriminating observables. As examples illustrating the fit results, Fig. 2 shows the E_T^{miss} distribution in the e^+ barrel channel of the SR and the $m_T(W)$ distribution in the μ^+ channel of the SR.

The stacked histograms were normalised to the fit result. The low E_T^{miss} and $m_T(W)$ regions drove the estimate of the multijet background, since its fraction of the total yield was larger there than at higher values of the two observables. The yield of the multijet background after applying the requirements of $E_T^{\text{miss}} > 30$ GeV and $m_T(W) > 50$ GeV is based on the normalised histograms of the multijet background normalised to the fit result and was later used as a starting value for the profile-likelihood fit in the final statistical analysis. The normalisation factors obtained for top-quark production and W +jets production were applied to normalise the respective backgrounds when validating the modelling of kinematic distributions prior to the statistical analysis of the NN discriminants, but they were not used in the statistical analysis itself.

All backgrounds other than the multijet background were modelled by simulated events and the event rate was estimated by scaling the samples of simulated events to the integrated luminosity of the sample of collision data being analysed. The event kinematics of the multijet background is described with the jet-electron model and with non-prompt muon events, normalising the rate of the multijet background to the results of the fits to the E_T^{miss} and $m_T(W)$ distributions. Figure 3 provides a summary of the fractional contributions of the different background processes to the expected event yield in the SR.

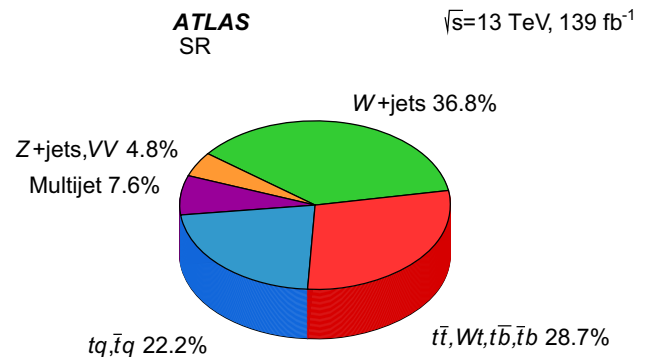


Fig. 3 Pie chart of the background composition of the SR. The SR comprises the two electron channels (barrel and endcap) and the muon channel. The pre-fit event yields are reported in Table 3

The three largest backgrounds are W +jets production, the combined $t\bar{t}$ - tW - $t\bar{b}$ background, and tq production.

6 Neural networks separating signal and background events

Two NNs were employed to enhance the separation of signal events from background events by combining several kinematic (input) variables to form two discriminants named D_1 and D_2 . The kinematics of signal events depends on whether the quark (antiquark) in the initial state is a valence quark or a sea quark (antiquark). Sea quarks (antiquarks) and valence quarks of the proton carry, on average, different fractions x of the proton momentum and this difference leads to different rapidity distributions for the corresponding produced top quarks (antiquarks) and their decay prod-

Table 2 Input variables to the two NNs

Variable	Definition
Variables common to the D_1 and D_2 NNs	
$p_T(b)$	Transverse momentum of the b -tagged jet
$m(\ell b)$	Invariant mass of the charged lepton (ℓ) and the b -tagged jet (b)
$m_T(W)$	Transverse mass of the reconstructed W boson
$\Delta R(W, b)$	Distance in the η - ϕ plane between the reconstructed W boson and the b -tagged jet
$ \Delta\phi(W, b) $	Azimuthal angle between the reconstructed W boson and the b -tagged jet
$m(\ell\nu b)$	Top-quark mass reconstructed from the charged lepton, neutrino, and b -tagged jet
Variables used only for the D_1 NN	
$\text{sgn } q(\ell)$	Sign of the charge of the primary lepton
$H_T(\ell, b, E_T^{\text{miss}})$	Scalar sum of the transverse momenta of all reconstructed objects
$\eta(W)$	Pseudorapidity of the reconstructed W boson
$ \Delta\phi(\ell, \vec{p}_T^{\text{miss}}) $	Azimuthal angle between the charged lepton and \vec{p}_T^{miss} .
$ \Delta\phi(W, \ell) $	Azimuthal angle between the reconstructed W boson and the charged lepton
$p_T(\ell\nu b)$	Transverse momentum of the reconstructed top quark
Variables used only for the D_2 NN	
$\eta(b)$	Pseudorapidity of the b -tagged jet
$p_T(W)$	Transverse momentum of the reconstructed W boson
$\Delta R(\ell\nu b, W)$	Distance in the η - ϕ plane between the reconstructed top quark and W boson

ucts. Top quarks produced in the $u + g \rightarrow t$ process tend to have higher absolute rapidity values than top antiquarks produced in the $\bar{u} + g \rightarrow \bar{t}$ process and top quarks or top antiquarks produced in the $c + g \rightarrow t$ and $\bar{c} + g \rightarrow \bar{t}$ processes. The two discriminants D_1 and D_2 exploit these differences.

The first network was trained only with events from the cgt process and was thus optimised for events featuring a sea quark or antiquark in the initial state. The discriminant obtained from this network is defined to be D_1 . The second NN was trained with events from top-quark production via the ugt process as signal, excluding the charge-conjugate process of top-antiquark production. The corresponding discriminant is called D_2 . The discriminant D_1 is used in a search for the cgt process. The second analysis searches for the ugt process and makes use of both discriminants, D_1 and D_2 . In this case, two SRs were defined based on $\text{sgn}q(\ell)$. The discriminant D_1 was used in the ℓ^- channel targeting top-antiquark production ($\bar{u} + g \rightarrow \bar{t}$). The discriminant D_2 was computed in the ℓ^+ channel, aimed at the search for direct top-quark production ($u + g \rightarrow t$).

The NNs were implemented using the NeuroBayes package [84, 85], which combines a three-layer feed-forward NN with a complex and robust preprocessing of the input variables before they are presented to the NN. The training of the NNs was based on generated signal and background events and used back-propagation to determine the weights of connections among nodes. As a non-linear activation function, NeuroBayes uses the symmetric sigmoid function

$$S(x) = \frac{2}{1 + e^{-x}} - 1$$

which maps the interval $(-\infty, +\infty)$ to the interval $(-1, +1)$. In the region close to zero, the sigmoid function has a linear response. The D_1 and D_2 discriminants were obtained by linearly scaling the outputs of the corresponding NNs to the interval $(0, 1)$.

Sets of input variables were selected based on studies considering the sensitivity of the analyses as given by the expected upper limits on the production cross-sections (Sect. 8 provides more details about the computation of upper limits), how well the observed distributions of the input variables are modelled by simulation, and the ranking of the input variables provided by the preprocessing step of NeuroBayes. The D_1 NN used 12 input variables, the D_2 NN nine. Six of those variables were common to both NNs. Table 2 provides the list of input variables.

Some of the variables, for example $\Delta R(W, b)$ and $m(\ell\nu b)$, required reconstruction of the leptonically decaying W boson, which in turn required reconstruction of the neutrino momentum. While the x - and y -components of the neutrino momentum, $p_x(\nu)$ and $p_y(\nu)$, were approximated by the components of \vec{p}_T^{miss} , the z -component, $p_z(\nu)$, was determined by constraining the mass of the reconstructed W boson to match the measured world average. If the resulting quadratic equation had two real solutions, the one with the smallest $|p_z(\nu)|$ was chosen. In the case of complex solutions, which could occur due to the limited E_T^{miss} resolution, a kinematic fit was performed that rescaled the neutrino p_x

and p_y such that the imaginary part vanished and at the same time the transverse components of the neutrino momentum were kept as close as possible to the \vec{p}_T^{miss} . The W boson was formed by adding the four-vectors of the reconstructed neutrino and the charged lepton.

NeuroBayes uses Bayesian regularisation techniques for the training process to improve the generalisation performance and to avoid overtraining. In general, the network infrastructure consists of one input node for each input variable plus one bias node, an arbitrary, user-defined number of hidden nodes arranged in a single hidden layer, and one output node which gives a continuous output in the interval $(-1, +1)$. For the two NNs of this analysis, 15 nodes were used in the hidden layer and the ratio of signal to background events in the training was chosen to be 1:1. The different background processes were weighted according to their expected number of events. Only $t\bar{t}$, W +jets and single-top-quark events were used as background processes in the training. The multijet background was not used, since its modelling has considerable uncertainties and attempting to optimise the separation of this background from signal events would likely make the results of the analysis more sensitive to any mismodelling of the kinematics of multijet production. After the training step, samples of simulated signal and background events as well as the observed events were processed by the NNs. The resulting distributions of D_1 and D_2 normalised to unit area are shown in Fig. 4.

The signal distributions peak at high values between 0.8 and 0.9, while the distributions of the background processes peak at low values. Compared to the $t\bar{t}$ process, which has a low event fraction in the highest bins, the tq and W +jets production processes have higher event fractions in the most signal-like bins.

Prior to the application of the NNs to the observed collision data in the SR, the modelling of the input variables was checked. The corresponding distributions in the VRs were validated as well. The normalisation of the different scattering processes in the grouping reported in Fig. 3 was taken from the fits to the E_T^{miss} and $m_T(W)$ distributions for the estimation of the multijet background, reported in Sect. 5. As an additional check, the trained NNs were applied in the VRs using input variables corresponding to those in the SR. Three examples of discriminant distributions in the VRs are presented in Fig. 5. In all cases, the model describes the observed discriminant distributions within the estimated uncertainties.

7 Systematic uncertainties

Several sources of systematic uncertainty affect the expected event yield from signal and background processes as well as the shape of the NN discriminants used in the maximum-likelihood fit. The systematic uncertainties are divided into

two major categories. Experimental uncertainties are associated with the reconstruction of the four-momenta of final-state partonic objects: electrons, muons, b -jets, and E_T^{miss} as an indication of a primary neutrino. The second category of uncertainties is related to the modelling of scattering processes with event generators. In the following, the estimation of experimental and modelling uncertainties is explained in more detail.

7.1 Experimental uncertainties

The uncertainty in the integrated luminosity of the combined 2015–2018 data set is 1.7% and is based on a calibration of the luminosity scale using x - y beam-separation scans [21]. The luminosity uncertainty was applied to the signal and background event yields except for the multijet background, which was estimated in a data-driven way. Scale factors were applied to simulated events to correct for reconstruction, identification, isolation and trigger performance differences between data and detector simulation for electrons and muons. These scale factors, as well as the lepton momentum scale and resolution, were assessed using $Z \rightarrow \ell^+\ell^-$ events in simulation and data [71, 72]. Their systematic uncertainties were propagated to the expected event yields and discriminant distributions used in the maximum-likelihood fit.

The jet energy scale (JES) was calibrated using a combination of test-beam data, simulation and in situ techniques [77]. Its uncertainty is decomposed into a set of 30 uncorrelated components, of which 29 are non-zero in a given event depending on the type of simulation used. Sources of uncertainty contributing to the JES uncertainties include pile-up modelling, jet flavour composition, single-particle response and effects of jets not fully contained within the calorimeter. The uncertainty of the jet energy resolution (JER) is represented by eight components accounting for jet- p_T and η -dependent differences between simulation and data [86]. The uncertainty in the efficiency to pass the JVT requirement for pile-up suppression was also considered [78].

The uncertainties in the b -tagging calibration were determined for b -jets [80], broken down into 45 orthogonal components. The uncertainties depend on the p_T of the b -jets and were propagated through the analysis as weights. Since b -jets were identified with very high purity, the misidentification rate of c -jets and light-flavour jets was very low and a dedicated calibration was not performed. Only the W +jets background has a small component of misidentified c -jets and light-flavour jets. For other backgrounds and for the signal processes these components are negligible. Since the rate of the W +jets background was determined directly from the final maximum-likelihood fit, there was no need for an overall rate uncertainty on the W +jets background. Instead a

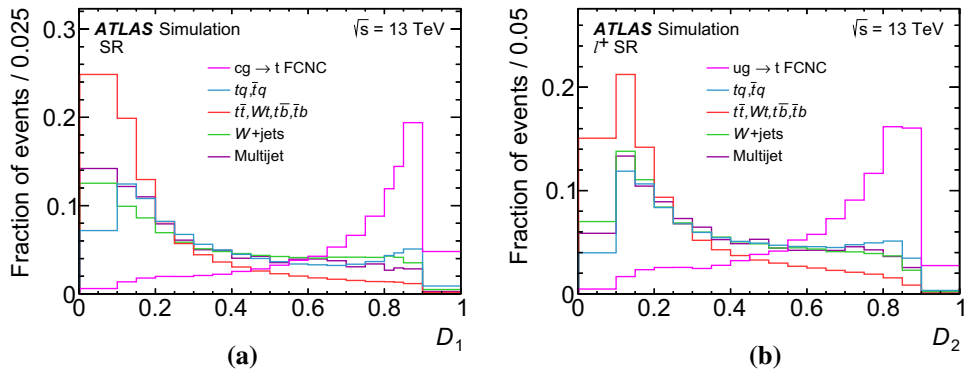
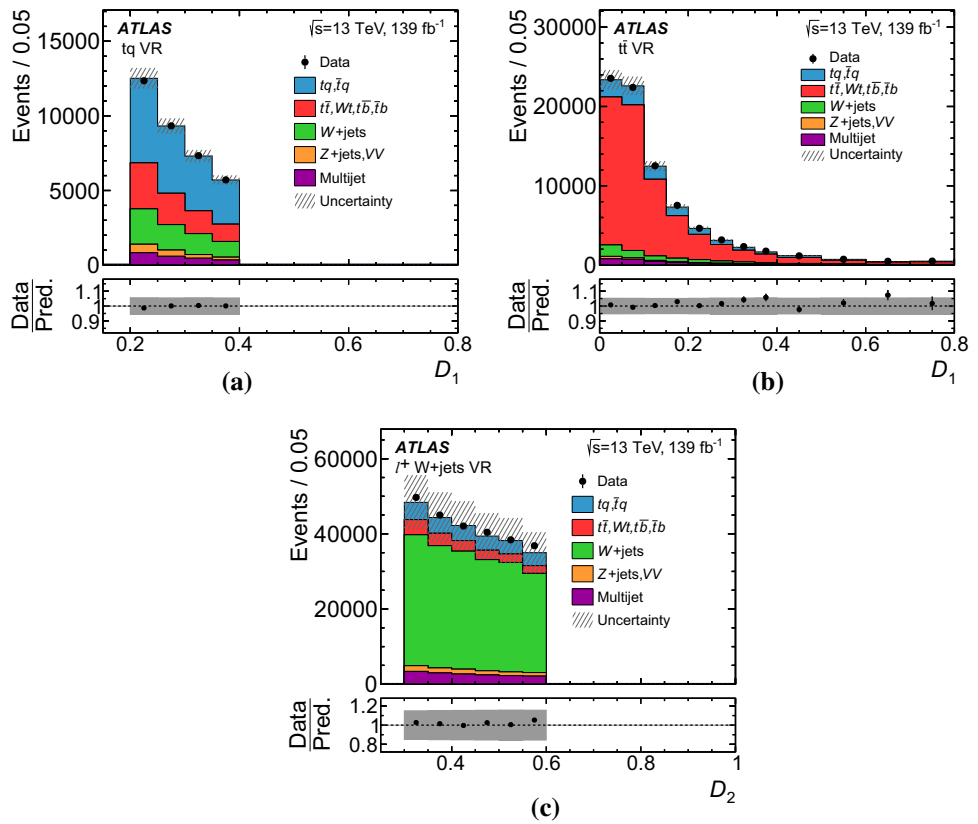


Fig. 4 Distributions of the D_1 and D_2 discriminants for signal and background processes. Each distribution is normalised to unit area. The discriminant D_1 was used for cgt analysis and the ℓ^- channel of the ugt analysis. The discriminant D_2 was used in the ℓ^+ channel of the

ugt analysis. The histograms in (a) show the distributions obtained in the cgt analysis, that is, the discriminant was evaluated for all selected events independent of $sgn q(\ell)$. The distributions in the ℓ^+ channel of the ugt analysis are shown in (b)

Fig. 5 Distributions of the NN discriminants D_1 and D_2 observed in a the tq VR, b the tt VR and c the ℓ^+ W +jets VR. The observed data are compared with the distribution of simulated background events normalised to the number of expected events, accounting for the normalisation factors obtained in the fits of the E_T^{miss} and $m_T(W)$ distributions for estimating the multijet background. The uncertainty band represents the uncertainty due to limited sample size and the rate uncertainties of the different processes (20% for W +jets production, 30% for the multijet background and 6% for the top-quark processes). The ratio of observed to predicted (Pred.) numbers of events in each bin is shown in the lower panel



dedicated shape uncertainty was assigned to the modelling of the contamination by c -jets and light-flavour jets. More details are given in the next section on modelling uncertainties.

The uncertainty in E_T^{miss} due to a possible miscalibration of its soft-track component was derived from data–simulation comparisons of the p_T balance between the hard and soft E_T^{miss} components [82]. To account for pile-up distribution differences between simulation and data, the pile-up profile in the simulation was corrected to match the one in data. The uncertainty associated with the correction factor was applied.

7.2 Modelling uncertainties

Uncertainties in the theoretical cross-sections were evaluated for the SM top-quark processes (tq , $t\bar{t}$, tW and $t\bar{b}$) as quoted in Sect. 3.2. The single largest background, W +jets production, was allowed to float in the likelihood fit and thus a cross-section uncertainty was not applied. A symmetric uncertainty of $\pm 20\%$ was assigned to the Z +jets production cross-section by evaluating the effect of seven variations of μ_r and μ_f in the matrix-element computation [87]. In this estimate, which is meant to account for missing higher-order

corrections, the scales were independently varied by factors of 0.5 and 2.0, avoiding the variations with ratios of four between the two scales. The biggest impact on the cross-sections was found for a correlated variation of μ_r and μ_f . The same uncertainty of $\pm 20\%$ was assigned to diboson production. The uncertainty in the event yield of the multijet background is 30%.

Uncertainties in modelling parton showers and hadronisation were assigned to the FCNC signal and the SM top-quark production processes ($t\bar{t}$, tW , tq and $t\bar{b}$ production) by comparing the nominal samples with alternative samples for which METOP and POWHEG BOX were interfaced to HERWIG7.0.4 instead of PYTHIA 8.235 or PYTHIA 8.230, respectively. When generating parton showers the MMHT2014LO [88] PDF set was used as well as the H7-UE-MMHT [40] set of tuned parameters. The uncertainties were defined independently for each scattering process, namely the FCNC signal process and the four SM top-quark production processes. In addition, normalisation and shape effects were decorrelated as well.

Uncertainties related to the choice of renormalisation and factorisation scales for the matrix-element calculations were evaluated by varying the scales in a correlated way by factors of 2 and 0.5, separately for each process. In the case of the FCNC signal processes, dedicated samples of simulated events were generated with varied scales. For the SM top-quark production processes and for W +jets production, the scale variations were implemented as generator weights in the nominal sample. These weights were propagated through the entire analysis.

The uncertainty due to the choice of a scale for matching the matrix-element calculation of the $t\bar{t}$ process to the parton shower was estimated using an additional $t\bar{t}$ sample produced with the h_{damp} parameter set to $3 \times m_t$, while keeping all other generator settings the same as for the nominal sample of $t\bar{t}$ events. The uncertainty due to the choice of matrix-element-to-parton-shower matching scale used in the generation of the FCNC signal samples was evaluated by comparisons with alternative samples produced with a matching scale of 15 GeV instead of the 10 GeV scale used for the nominal sample. The uncertainty related to the specific algorithm for matching the NLO-matrix-element computation to parton showers was evaluated for the SM top-quark production processes (tq , $t\bar{t}$, tW and $t\bar{b}$) by comparing samples generated by POWHEG BOX with samples generated by MADGRAPH5_AMC@NLO [89]. Both set-ups used PYTHIA for the parton-shower computation. The effects of this matching-algorithm uncertainty on the shape of the NN discriminants and on the event yields were decorrelated in the maximum-likelihood fit.

Uncertainties in the amount of initial-state and final-state radiation were assessed for the FCNC signal processes and the SM top-quark production processes by varying the

parameter Var3C of the A14 parton-shower tune within the uncertainties of the tune and, for final-state radiation, by varying the renormalisation scale μ_r , at which the strong coupling constant α_s was evaluated, by factors of 0.5 and 2.0. The two variations, the one of Var3C and the one of μ_r , were handled independently. The uncertainty due to the scheme for removing the overlap of the tW process with $t\bar{t}$ production was evaluated by comparing the nominal sample, using the diagram-removal scheme, with a sample produced with an alternative scheme (diagram subtraction) [50]. In all uncertainty evaluations mentioned above the alternative samples or reweighted samples were normalised to the total cross-section of the nominal samples.

Uncertainties due to PDFs were evaluated for the tq process and the combined $t\bar{t}$ - tW - $t\bar{b}$ process using the PDF4LHC15 combined PDF set [90] with 30 symmetric eigenvectors. Samples of simulated events were reweighted to the central value and the eigenvectors of the combined PDF set. Systematically varied templates were constructed by taking the differences between the samples reweighted to the central value and those reweighted to the eigenvectors. In the likelihood fit the PDF uncertainties were treated as correlated between the tq process and the combined $t\bar{t}$ - tW - $t\bar{b}$ process. The uncertainty in the average number of interactions per bunch crossing was accounted for by varying accordingly the scale factors applied to weight the simulated events in order to obtain the pile-up distribution observed in collision data.

The uncertainty in the multijet background was evaluated by modifying the respective selection criteria for the jet-lepton and the non-prompt-muon candidate. For each lepton type, two alternative selections were defined by varying the requirements on the energy fraction measured in the electromagnetic calorimeter in the case of the jet-lepton and by varying the isolation criteria for the muon candidates. The variations leading to the larger deviations from the nominal set-up were chosen when defining uncertainties in the shape of the NN discriminant distribution for the multijet background.

With a fraction of 92% the W + b -jets component dominates the W +jets background. Since the number of simulated events with jets of different flavour, c -jets or light-flavour jets, was very limited, the W +jets template was based on the W + b -jets component only. The expected event yield was scaled such that the events with jets of different flavour were also considered. To account for small shape differences between the NN-discriminant distributions for W + b -jets, W + c -jets and W +light-flavour jets, two alternative W +jets template histograms were created by adding to the nominal W + b -jets component the W + c -jets and W +light-flavour jets contributions with three times the expected rate. The resulting shape differences were applied in a symmetric way in the maximum-likelihood fit, which constrained the input uncer-

tainties to a level of 80% for $W+c$ -jets in both searches (ugt and cgt) and 40% (70%) for W +light-flavour jets in the ugt analysis (cgt analysis). In the cgt analysis using the D_1 discriminant, the $W+c$ -jets input uncertainty is approximately $\pm 9\%$ for NN discriminant values below 0.7 and rises to $\pm 12\%$ at high values. The W +light-flavour jets input uncertainty is approximately $\pm 4\%$ for NN discriminant values of 0.75 to 1.0, while at values below 0.1 it reaches $\pm 10\%$. In the ugt analysis, the corresponding uncertainties in the shapes of the D_1 and D_2 discriminants have very similar features.

The uncertainties due to the finite number of simulated events, also called the MC statistical uncertainty, was accounted for by adding a nuisance parameter for each bin of the NN discriminant distributions separately for each scattering process, implementing the Barlow–Beeston approach [91].

8 Results

The observed distributions of the NN discriminants were subjected to a binned maximum-likelihood fit, probing for a potential FCNC signal. Two analyses were performed, searching separately for the ugt and cgt FCNC processes. The likelihood function \mathcal{L} was constructed as a product of Poisson probability terms over all bins of the NN discriminants. The function $\mathcal{L}(\mu, \vec{\theta})$ depends on the signal-strength parameter μ , a multiplicative factor to the signal production cross-section used to normalise the simulated signal samples, and $\vec{\theta}$, a set of nuisance parameters including the effects of systematic uncertainties on the signal and background expectations. The range of each nuisance parameter was constrained in the likelihood function by a Gaussian term. The signal strength of the W +jets process, $\mu(Wj)$, was treated as a free multiplicative factor as well. In the ugt analysis, in contrast to the cgt analysis, the rates of the W^+ +jets and W^- +jets processes were determined separately in a simultaneous fit using two independent normalisation parameters.

Systematically varied discriminant distributions were smoothed and nuisance parameters of systematic uncertainties with negligible impact were entirely removed in order to reduce spurious effects in minimisation, improve convergence of the fit, and reduce the computing time. Normalisation and shape effects of a source of systematic uncertainty were treated separately in the pruning process.

Single-sided systematic variations were turned into symmetric variations by taking the full difference in event yield and shape between the nominal model and the alternative model and mirroring this difference in the opposite direction. For sources with two variations, their effects were made symmetric by using the average deviation from the nominal prediction.

8.1 Results of the profile likelihood fit

The results of the maximum-likelihood fits yielded: $\mu(ugt) = 0.10 \pm 0.18$,³ $\mu(W^+j) = 1.25 \pm 0.15$ and $\mu(W^-j) = 1.32 \pm 0.17$ as well as $\mu(cgt) = 0.15 \pm 0.17$ and $\mu(Wj) = 1.19 \pm 0.15$. The normalisation factors of the W +jets process were determined to be above 1 in all cases. This finding is similar to that from a dedicated measurement of the cross-section of the $Z + \geq 1$ b -jet process [92]. No significant nuisance parameters pulls were observed in either fit. The impact of systematic uncertainties on the sensitivity is much larger than that of the data statistical uncertainties. An importance ranking of systematic uncertainties was determined by computing the shifts $\Delta\mu_j$ in the signal-strength parameters $\mu(ugt)$ and $\mu(cgt)$ when fixing a particular nuisance θ_j related to the uncertainty j to its estimated value $\hat{\theta}_j$ plus or minus its post-fit uncertainty $\Delta\hat{\theta}_j$. In the ranking, the uncertainties are sorted in $|\Delta\mu_j|$ in descending order.

The five leading systematic uncertainties in the ugt fit are due to the MC statistical uncertainty in the highest bin of the NN discriminant D_2 of the W +jets process, the $W+c$ -jets shape uncertainty, the first effective nuisance parameter of the uncertainty in the jet-energy resolution, the MC statistical uncertainty in the second-highest bin of the NN discriminant D_2 of the W +jets process, and the normalisation component of the uncertainty in the matrix-element-matching algorithm of the tq process. Out of these leading uncertainties, the three non-MC-statistical uncertainties were constrained in the fit to the range of 80% to 90% of their original value. The five leading systematic uncertainties in the cgt fit are due to the modelling of the parton shower of the FCNC cgt process, the shape component of the parton-shower uncertainty of the tq process, the uncertainty in the resolution of the soft-track term of the E_T^{miss} computation, the shape component of the uncertainty in the matrix-element-matching algorithm of the tq process, and the MC statistical uncertainty in the highest bin of the NN discriminant D_1 of the W +jets process. Out of these leading uncertainties of the cgt analysis, the fit constrained the three non-MC-statistical uncertainties to the range of 65% to 90% of their original value.

Table 3 provides the expected, the observed, and the fitted event yields in the SR.

The results of the ugt and cgt analyses differ slightly, but agree well within uncertainties. The event yields after the fit account for pulls of the nuisance parameters. The fitted discriminant distributions are shown in Figs. 6 and 7 for the ugt and cgt analyses, respectively.

³ The reference cross-sections of the signal processes are $\sigma(u + g \rightarrow t) \times \mathcal{B}(t \rightarrow Wb) \times \mathcal{B}(W \rightarrow \ell\nu) = 6.27$ pb and $\sigma(c + g \rightarrow t) \times \mathcal{B}(t \rightarrow Wb) \times \mathcal{B}(W \rightarrow \ell\nu) = 8.52$ pb.

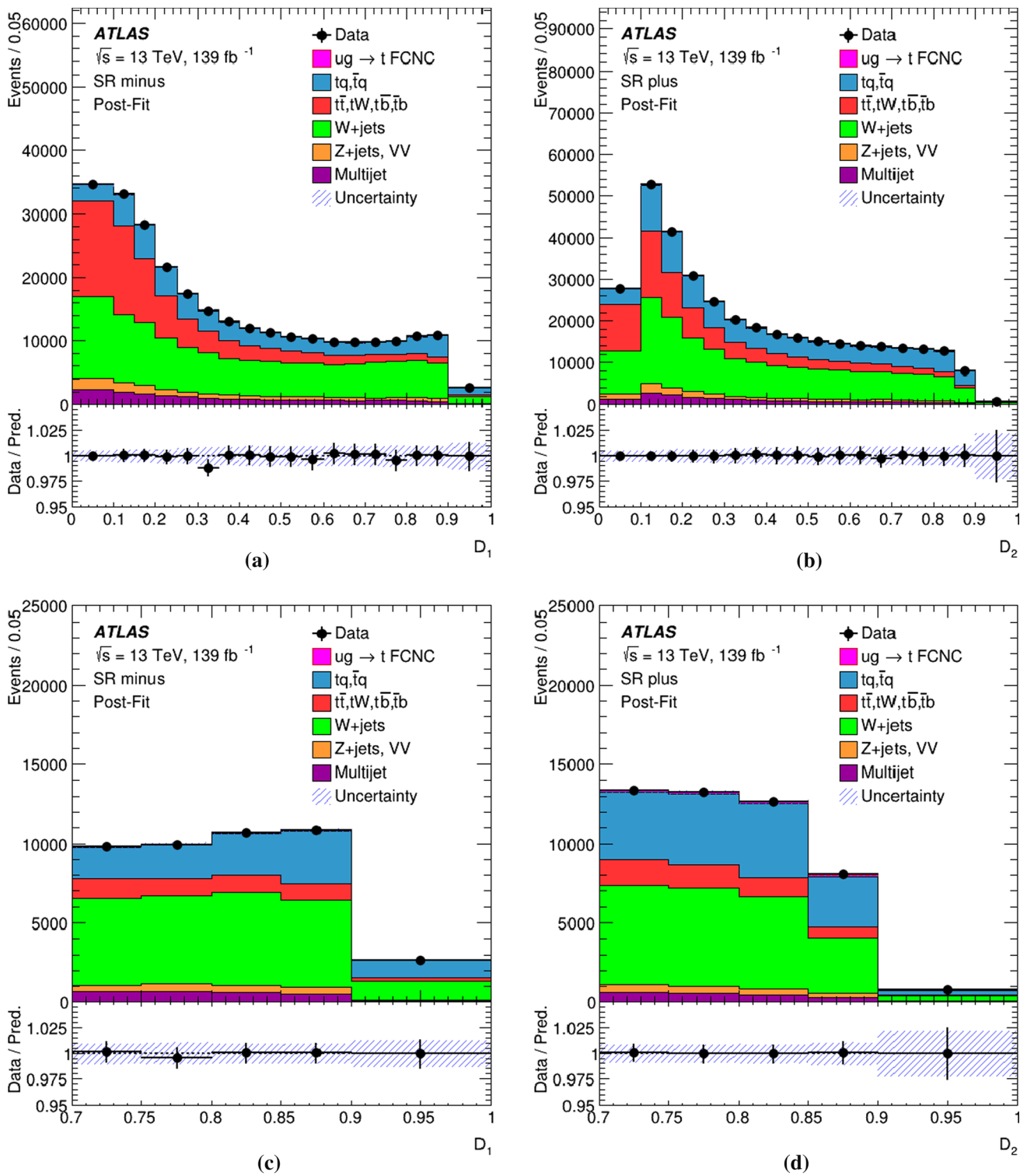


Fig. 6 The NN discriminants D_1 and D_2 of the ugt search are shown with the post-fit normalisation applied to the stacked histograms of the different hard-scattering processes. The histograms in **a** and **b** show the full discriminant range in the negatively charged lepton channel and the positively charged lepton channel, respectively. The histograms **c**

and **d** show a zoomed-in view of the high discriminant region between 0.7 and 1.0. The hatched bands represent the post-fit uncertainty of the total event yield in each bin. Correlations among uncertainties were taken into account as determined in the fit. The fitted signal contribution is included but is barely visible because its relative size is very small

Table 3 Expected pre-fit and post-fit event yields along with the observed event yield in the SR. The quoted uncertainties include the statistical and systematic uncertainties of the event yields. Correlations,

including anticorrelations, among the nuisance parameters related to the uncertainties were taken into account as determined in the maximum-likelihood fit

Process	Pre-fit	Post-fit cg_t	Post-fit ugt
ugt FCNC process	0	0	1200 ± 2100
cg_t FCNC process	0	4100 ± 4500	0
tq	$138,600 \pm 9300$	$149,200 \pm 9400$	$150,000 \pm 10,000$
$t\bar{t}, tW, t\bar{b}$	$179,000 \pm 17,000$	$179,000 \pm 14,000$	$175,200 \pm 9700$
W +jets	$229,000 \pm 30,000$	$281,000 \pm 21,000$	$292,000 \pm 18,000$
Z +jets, VV	$29,700 \pm 6000$	$30,000 \pm 6000$	$29,800 \pm 6000$
Multijet	$47,000 \pm 14,000$	$45,000 \pm 14000$	$40,000 \pm 12,000$
Total	$650,000 \pm 46,000$	$688,600 \pm 2400$	$688,700 \pm 3500$
Observed	688,380	688,380	688,380

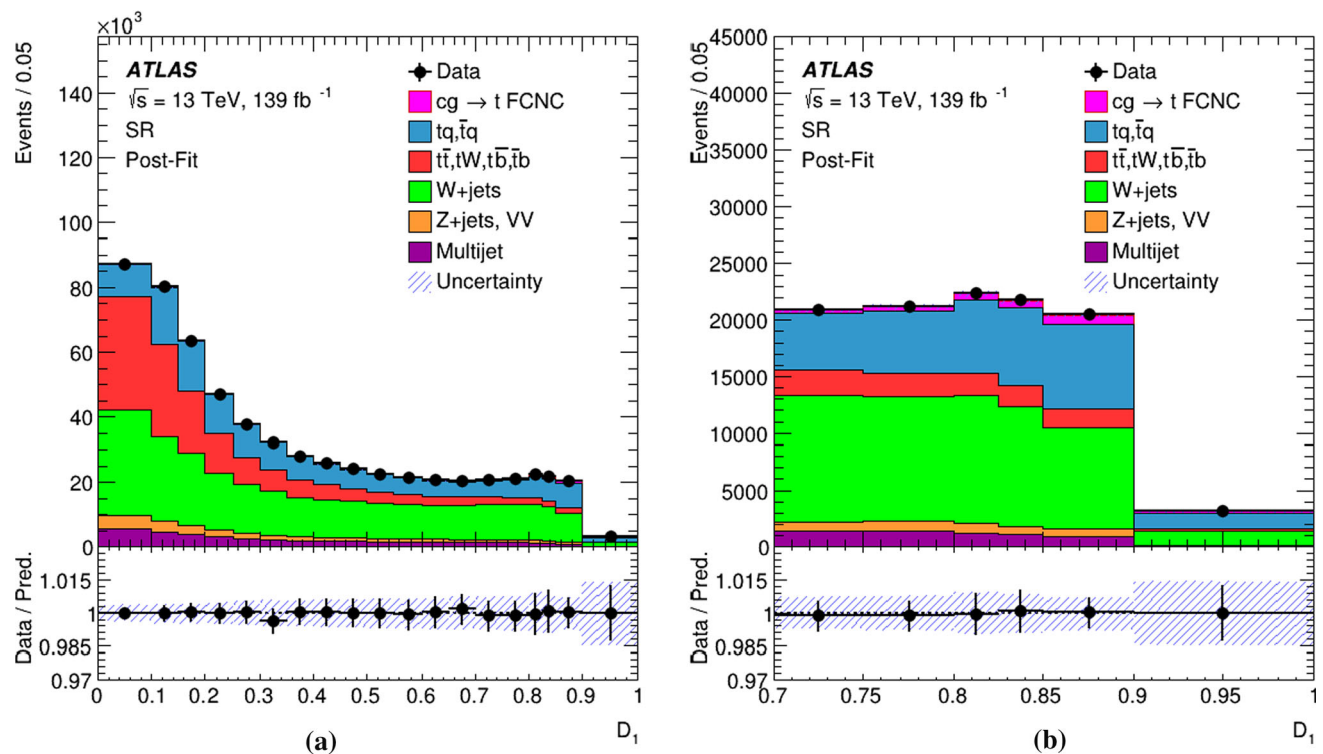


Fig. 7 The NN discriminant D_1 of the cg_t search is shown with the post-fit normalisation applied to the stacked histograms of the different hard-scattering processes. The histogram in **a** shows the full discriminant range. The histogram **b** shows a zoomed-in view of the high

discriminant region between 0.7 and 1.0. The hatched bands represent the post-fit uncertainty of the total event yield in each bin. Correlations among uncertainties were taken into account as determined in the fit

The observed discriminant distributions are very well described by the fitted model and they are compatible with the background-only hypothesis.

8.2 Upper limits on cross-sections, EFT coefficients and branching ratios

Since the observed NN-discriminant distributions were found to be compatible with the background-only hypoth-

esis, upper limits were set on the cross-sections of the ugt and the cg_t processes at the 95% confidence level (CL). The limits were computed by applying the CL_s method [93, 94] as implemented in the RooFit package [95] to the test statistic

$$\tilde{q}_\mu = \begin{cases} -2 \ln \left(\frac{\mathcal{L}(\mu, \hat{\theta}(\mu))}{\mathcal{L}(0, \hat{\theta}(0))} \right) & \text{if } \hat{\mu} < 0, \\ -2 \ln \left(\frac{\mathcal{L}(\mu, \hat{\theta}(\mu))}{\mathcal{L}(\hat{\mu}, \hat{\theta})} \right) & \text{if } 0 \leq \hat{\mu} \leq \mu, \\ 0 & \text{if } \hat{\mu} > \mu. \end{cases} \quad (2)$$

In Eq. (2), the symbols $\hat{\mu}$ and $\hat{\theta}$ represent the values of the parameters maximising the likelihood function and $\hat{\theta}$ are the values of the nuisance parameters which maximise the likelihood function for a fixed value of μ . The obtained upper limits on the cross-sections times branching ratio are

$$\sigma(ugt) \times \mathcal{B}(t \rightarrow Wb) \times \mathcal{B}(W \rightarrow \ell\nu) < 3.0 \text{ pb} \quad \text{and} \quad (3)$$

$$\sigma(cgt) \times \mathcal{B}(t \rightarrow Wb) \times \mathcal{B}(W \rightarrow \ell\nu) < 4.7 \text{ pb}, \quad (4)$$

with $\mathcal{B}(W \rightarrow \ell\nu) = 0.325$ being the sum of branching ratios of all three leptonic decay modes of the W boson. The expected cross-section-times-branching-ratio limits are 2.4 pb and 2.5 pb, respectively. The observed limits are larger than the expected ones because non-zero signal yields are fitted.

The cross-section limits are interpreted within the TOPFCNC model [14], which implements an effective operator formalism and is based on the FEYNRULES 2.0 framework [96] used inside the MADGRAPH5_AMC@NLOevent generator. With this set-up the cross-sections of the FCNC processes under consideration were calculated at NLO in QCD, providing a significant improvement on LO calculations, since NLO corrections for this class of processes were found to be between 30% and 80% [14].⁴ In the TOPFCNC model, the two operators \mathcal{O}_{uG}^{ut} and \mathcal{O}_{uG}^{ct} generate the ugt and cgt processes, and the coupling strengths of the corresponding vertices are given by the two coefficients C_{uG}^{ut} and C_{uG}^{ct} divided by the square of the new-physics scale Λ . The total cross-sections are found to be related to the EFT coefficients by

$$\sigma(u + g \rightarrow t) = 2773 \times \left(\frac{C_{uG}^{ut}}{\Lambda^2} \right)^2 \text{ pb TeV}^4 \quad \text{and} \quad (5)$$

$$\sigma(c + g \rightarrow t) = 719 \times \left(\frac{C_{uG}^{ct}}{\Lambda^2} \right)^2 \text{ pb TeV}^4. \quad (6)$$

Using Eqs. (5) and (6) the cross-section limits of Eqs. (3) and (4) become limits on the EFT coefficients:

$$\begin{aligned} \frac{|C_{uG}^{ut}|}{\Lambda^2} &< 0.057 \text{ TeV}^{-2} \quad \text{and} \\ \frac{|C_{uG}^{ct}|}{\Lambda^2} &< 0.14 \text{ TeV}^{-2} \quad \text{at the 95\% CL.} \end{aligned} \quad (7)$$

⁴ While MADGRAPH5_AMC@NLO can be used for a fixed-order calculation at NLO, events for which a matching to a parton-shower program is needed can only be generated at LO in the current implementation.

Since the u -quark is a valence quark of the proton, it carries on average a much larger momentum fraction than the c -quark, and thus the cross-section of the ugt process is much larger than the cross-section of the cgt process, when considering the same value of the corresponding coefficient ($C_{uG}^{ut} = C_{uG}^{ct}$). For a certain experimental sensitivity, the sensitivity to C_{uG}^{ut} is therefore higher than to C_{uG}^{ct} . However, in the two-Higgs-doublet models mentioned in Sect. 1 the predicted FCNC couplings to charm quarks are much higher than to up quarks. For this reason, the limits on C_{uG}^{ct} have phenomenological relevance even though they are weaker than the limits on C_{uG}^{ut} . The limits presented in Eq. (7) tighten constraints set by the CMS Collaboration using dilepton events recorded in Run 2 of the LHC [97] by more than a factor of three. The CMS analysis searched for tW production cross-section via FCNC.

An alternative and very accessible way of comparing the upper limits on the EFT coefficient with previous results uses the branching ratios of FCNC top-quark decays: $\mathcal{B}(t \rightarrow u + g)$ and $\mathcal{B}(t \rightarrow c + g)$. These branching ratios are given as a function of the EFT coefficients by the relation

$$\mathcal{B}(t \rightarrow q + g) = 0.0186 \times \left(\frac{C_{uG}^{qt}}{\Lambda^2} \right)^2 \text{ TeV}^4,$$

with $q = u, c$ [98], assuming the top-quark width to be $\Gamma_t = 1.32 \text{ GeV}$. The resulting upper limits at the 95% CL are

$$\begin{aligned} \mathcal{B}(t \rightarrow u + g) &< 0.61 \times 10^{-4} \quad \text{and} \\ \mathcal{B}(t \rightarrow c + g) &< 3.7 \times 10^{-4}. \end{aligned} \quad (8)$$

These new bounds are approximately a factor of two more restrictive than the previous ATLAS results obtained at a centre-of-mass energy of 8 TeV [12]. The bound on the cgt mode is comparable to that of the CMS analysis combining 7 and 8 TeV data [11], while the bound on the ugt mode is significantly weaker than the CMS one.

8.3 Comparison of expected upper limits

For assessing the sensitivity of this analysis and comparing it with the sensitivity of other results, and for evaluating the impact of different groups of systematic uncertainties, the computation of expected upper limits is more suitable than using the observed results, since biases caused by statistical fluctuations are avoided and the signal contribution is set to zero. The expected limits were derived by using the expected distributions of the NN discriminants, considering background processes only. The initially predicted rate of the W +jets process was scaled by a factor of $\mu(W^+b) = 1.22$ or $\mu(W^-b) = 1.30$ for the ugt analysis and by a factor of $\mu(Wb) = 1.18$ for the cgt analysis. These normalisation factors were obtained from background-only fits to the observed NN discriminants in background-dominated regions, namely

Table 4 Impact of systematic uncertainties on the expected upper limits on the branching ratios of the FCNC decay modes $\mathcal{B}(t \rightarrow u + g)$ and $\mathcal{B}(t \rightarrow c + g)$. Four scenarios are considered: (1) include only data

Scenario	Description	$\mathcal{B}_{95}^{\text{exp}}(t \rightarrow u + g)$	$\mathcal{B}_{95}^{\text{exp}}(t \rightarrow c + g)$
(1)	Data statistical only	1.1×10^{-5}	2.4×10^{-5}
(2)	Experimental uncertainties also	3.1×10^{-5}	12×10^{-5}
(3)	All uncertainties except MC statistical	3.9×10^{-5}	18×10^{-5}
(4)	All uncertainties	4.9×10^{-5}	20×10^{-5}

the ranges 0.0 to 0.7 for the D_1 discriminant and 0.0 to 0.55 for the D_2 discriminant. The resulting expected upper limits in terms of branching ratios are

$$\begin{aligned} \mathcal{B}_{95}^{\text{exp}}(t \rightarrow u + g) &= 0.49 \times 10^{-4} \quad \text{and} \\ \mathcal{B}_{95}^{\text{exp}}(t \rightarrow c + g) &= 2.0 \times 10^{-4}. \end{aligned} \quad (9)$$

Compared to the ATLAS analysis at 8 TeV centre-of-mass energy, significant improvements in sensitivity are obtained for both the ugt and cgt analyses. However, the improvements in sensitivity are smaller than expected from a simple scaling of the number of expected events with the increase in integrated luminosity and the increase in signal cross-sections. The main reason for this effect is that the cross-sections of the top-quark background processes rise faster with the centre-of-mass energy than the cross-sections of the FCNC signal processes.

The expected upper limits are lower than the observed upper limits in Eq. (8), since non-zero, yet insignificant, signals are observed, while the expected limits are obtained from expected distributions without any signal events included. The effect is larger for the cgt analysis than for the ugt analysis because the fitted signal event yield is more than three times larger in the cgt case, as seen in Table 3.

In order to quantify the impact of different groups of systematic uncertainties, expected upper limits were computed for different scenarios: (1) include only data statistical uncertainties, (2) include the experimental systematic uncertainties in addition, (3) include all systematic uncertainties except for the MC statistical uncertainties and (4) include all uncertainties. The last case leads to the limits quoted in Eq. (9). The results of this study are reported in Table 4 and clearly demonstrate how large the impact of systematic uncertainties is. Both the experimental and modelling uncertainties are relevant. MC statistical uncertainties increase the expected upper limits by approximately 20% in the ugt case and by about 10% for the cgt process.

9 Conclusions

A search for the production of a single top quark via left-handed FCNC interactions of a top quark, a gluon and an

statistical uncertainties, (2) include the experimental systematic uncertainties in addition, (3) include all systematic uncertainties except for the MC statistical uncertainties and (4) include all uncertainties

up or charm quark was performed. The analysis used the full LHC Run 2 proton–proton collision data set recorded with the ATLAS detector at a centre-of-mass energy of 13 TeV, corresponding to an integrated luminosity of 139 fb^{-1} . Events with exactly one electron or muon, exactly one b -tagged jet and missing transverse momentum were selected, resembling the decay products of a single top quark. A dedicated high-purity working point was devised for the identification of b -jets, reducing the background of $W+c$ -jets and W +light-flavour jets considerably. Neural networks were used to separate signal events from background events, and a binned maximum-likelihood fit to the neural-network discriminants was performed to search for a contribution from the $u+g \rightarrow t$ and $c+g \rightarrow t$ processes. The observed distributions were found to be compatible with the background-only hypothesis and therefore upper limits on the production cross-sections times branching ratios were derived, leading to

$$\begin{aligned} \sigma(ugt) \times \mathcal{B}(t \rightarrow Wb) \times \mathcal{B}(W \rightarrow \ell\nu) &< 3.0 \text{ pb} \quad \text{and} \\ \sigma(cgt) \times \mathcal{B}(t \rightarrow Wb) \times \mathcal{B}(W \rightarrow \ell\nu) &< 4.7 \text{ pb}. \end{aligned}$$

The cross-section limits were interpreted in the framework of an effective field theory, yielding limits on the coefficients of the operators producing the FCNC processes under investigation: $|C_{uG}^{ut}|/\Lambda^2 < 0.057 \text{ TeV}^{-2}$ and $|C_{uG}^{ct}|/\Lambda^2 < 0.14 \text{ TeV}^{-2}$ at the 95% confidence level. These limits are also expressed in terms of branching ratios of corresponding FCNC top-quark decays, resulting in

$$\begin{aligned} \mathcal{B}(t \rightarrow u + g) &< 0.61 \times 10^{-4} \quad \text{and} \quad \mathcal{B}(t \rightarrow c + g) \\ &< 3.7 \times 10^{-4}. \end{aligned}$$

The new bounds improve on previous ATLAS results obtained at a centre-of-mass energy of 8 TeV by approximately a factor of two.

Acknowledgements We thank CERN for the very successful operation of the LHC, as well as the support staff from our institutions without whom ATLAS could not be operated efficiently. We acknowledge the support of ANPCyT, Argentina; YerPhI, Armenia; ARC, Australia; BMWF and FWF, Austria; ANAS, Azerbaijan; SSTC, Belarus; CNPq and FAPESP, Brazil; NSERC, NRC and CFI, Canada; CERN; ANID, Chile; CAS, MOST and NSFC, China; Minciencias, Colombia; MSMT CR, MPO CR and VSC CR, Czech Republic; DNR and DNSRC, Denmark; IN2P3-CNRS and CEA-DRF/IRFU, France; SRNSFG, Georgia;

BMBF, HGF and MPG, Germany; GSRI, Greece; RGC and Hong Kong SAR, China; ISF and Benozio Center, Israel; INFN, Italy; MEXT and JSPS, Japan; CNRST, Morocco; NWO, Netherlands; RCN, Norway; MEiN, Poland; FCT, Portugal; MNE/IFA, Romania; JINR; MES of Russia and NRC KI, Russian Federation; MESTD, Serbia; MSSR, Slovakia; ARRS and MIZŠ, Slovenia; DSI/NRF, South Africa; MICINN, Spain; SRC and Wallenberg Foundation, Sweden; SERI, SNSF and Cantons of Bern and Geneva, Switzerland; MOST, Taiwan; TAEK, Turkey; STFC, United Kingdom; DOE and NSF, United States of America. In addition, individual groups and members have received support from BCKDF, CANARIE, Compute Canada and CRC, Canada; COST, ERC, ERDF, Horizon 2020 and Marie Skłodowska-Curie Actions, European Union; Investissements d'Avenir Labex, Investissements d'Avenir IDEX and ANR, France; DFG and AvH Foundation, Germany; Herakleitos, Thales and Aristeia programmes co-financed by EU-ESF and the Greek NSRF, Greece; BSF-NSF and GIF, Israel; Norwegian Financial Mechanism 2014-2021, Norway; NCN and NAWA, Poland; La Caixa Banking Foundation, CERCA Programme Generalitat de Catalunya and PROMETEO and GenT Programmes Generalitat Valenciana, Spain; Göran Gustafssons Stiftelse, Sweden; The Royal Society and Leverhulme Trust, United Kingdom. The crucial computing support from all WLCG partners is acknowledged gratefully, in particular from CERN, the ATLAS Tier-1 facilities at TRIUMF (Canada), NDGF (Denmark, Norway, Sweden), CC-IN2P3 (France), KIT/GridKA (Germany), INFN-CNAF (Italy), NL-T1 (Netherlands), PIC (Spain), ASGC (Taiwan), RAL (UK) and BNL (USA), the Tier-2 facilities worldwide and large non-WLCG resource providers. Major contributors of computing resources are listed in Ref. [99].

Open Access This article is licensed under a Creative Commons Attribution 4.0 International License, which permits use, sharing, adaptation, distribution and reproduction in any medium or format, as long as you give appropriate credit to the original author(s) and the source, provide a link to the Creative Commons licence, and indicate if changes were made. The images or other third party material in this article are included in the article's Creative Commons licence, unless indicated otherwise in a credit line to the material. If material is not included in the article's Creative Commons licence and your intended use is not permitted by statutory regulation or exceeds the permitted use, you will need to obtain permission directly from the copyright holder. To view a copy of this licence, visit <http://creativecommons.org/licenses/by/4.0/>.
Funded by SCOAP³.

References

1. S.L. Glashow, J. Iliopoulos, L. Maiani, Weak interactions with lepton-hadron symmetry. Phys. Rev. D **2**, 1285 (1970)
2. CLEO Collaboration, First measurement of the rate for the inclusive radiative penguin decay $b \rightarrow s\gamma$. Phys. Rev. Lett. **74**, 2885 (1995)
3. J.A. Aguilar-Saavedra, Top flavour-changing neutral interactions: theoretical expectations and experimental detection. Acta Phys. Polon. B **35**, 2695 (2004). [arXiv:hep-ph/0409342](https://arxiv.org/abs/hep-ph/0409342)
4. D. Atwood, L. Reina, A. Soni, Phenomenology of two Higgs doublet models with flavor-changing neutral currents. Phys. Rev. D **55**, 3156 (1997). [arXiv:hep-ph/9609279](https://arxiv.org/abs/hep-ph/9609279)
5. S. Bejar, J. Guasch, J. Sola, Loop induced flavor changing neutral decays of the top quark in a general two-Higgs-doublet model. Nucl. Phys. B **600**, 21 (2001). [arXiv:hep-ph/0011091](https://arxiv.org/abs/hep-ph/0011091)
6. D. Delepine, S. Khalil, Top flavour violating decays in general supersymmetric models. Phys. Lett. B **599**, 62 (2004). [arXiv:hep-ph/0406264](https://arxiv.org/abs/hep-ph/0406264)
7. J.J. Cao et al., Supersymmetry-induced flavor-changing neutral-current top-quark processes at the CERN Large Hadron Collider. Phys. Rev. D **75**, 075021 (2007). [arXiv:hep-ph/0702264](https://arxiv.org/abs/hep-ph/0702264)
8. J.-L. Yang, T.-F. Feng, H.-B. Zhang, G.-Z. Ning, X.-Y. Yang, Top quark decays with flavor violation in the B-LSSM. Eur. Phys. J. C **78**, 438 (2018). [arXiv:1806.01476](https://arxiv.org/abs/1806.01476) [hep-ph]
9. D0 Collaboration, Search for flavor changing neutral currents via quark-gluon couplings in single top quark production using $2.3 fb^{-1}$ of $p\bar{p}$ collisions. Phys. Lett. B **693**, 81 (2010). [arXiv:1006.3575](https://arxiv.org/abs/1006.3575) [hep-ex]
10. CDF II Collaboration, Search for top-quark production via flavor-changing neutral currents in W+1 jet events at CDF. Phys. Rev. Lett. **102**, 151801 (2009). [arXiv:0812.3400](https://arxiv.org/abs/0812.3400) [hep-ex]
11. CMS Collaboration, Search for anomalous Wtb couplings and flavour-changing neutral currents in t-channel single top quark production in pp collisions at $\sqrt{s} = 7$ and 8 TeV. JHEP **02**, 028 (2017). [arXiv:1610.03545](https://arxiv.org/abs/1610.03545) [hep-ex]
12. ATLAS Collaboration, Search for single top-quark production via flavour-changing neutral currents at 8 TeV with the ATLAS detector. Eur. Phys. J. C **76**, 55 (2016). [arXiv:1509.00294](https://arxiv.org/abs/1509.00294) [hep-ex]. Erratum: Eur. Phys. J. C **82**, 70 (2022)
13. ATLAS Collaboration, Search for FCNC single top-quark production at $\sqrt{s} = 7$ TeV with the ATLAS detector. Phys. Lett. B **712**, 351 (2012). [arXiv:1203.0529](https://arxiv.org/abs/1203.0529) [hep-ex]
14. C. Degrande, F. Maltoni, J. Wang, C. Zhang, Automatic computations at next-to-leading order in QCD for top-quark flavor-changing neutral processes. Phys. Rev. D **91**, 034024 (2015). [arXiv:1412.5594](https://arxiv.org/abs/1412.5594) [hep-ph]
15. ATLAS Collaboration, The ATLAS Experiment at the CERN Large Hadron Collider. JINST **3**, S08003 (2008)
16. ATLAS Collaboration, ATLAS Insertable B-Layer Technical Design Report, ATLAS-TDR-19, CERN-LHCC-2010-013 (2010). <https://cds.cern.ch/record/1291633>. Addendum: ATLAS-TDR-19-ADD-1, CERN-LHCC-2012-009 (2012). <https://cds.cern.ch/record/1451888>
17. B. Abbott et al., Production and integration of the ATLAS Insertable B-Layer. JINST **13**, T05008 (2018). [arXiv:1803.00844](https://arxiv.org/abs/1803.00844) [physics.ins-det]
18. ATLAS Collaboration, Performance of the ATLAS trigger system in 2015. Eur. Phys. J. C **77**, 317 (2017). [arXiv:1611.09661](https://arxiv.org/abs/1611.09661) [hep-ex]
19. ATLAS Collaboration, The ATLAS Collaboration Software and Firmware, ATL-SOFT-PUB-2021-001 (2021). <https://cds.cern.ch/record/2767187>
20. ATLAS Collaboration, ATLAS data quality operations and performance for 2015–2018 data-taking. JINST **15**, P04003 (2020). [arXiv:1911.04632](https://arxiv.org/abs/1911.04632) [physics.ins-det]
21. ATLAS Collaboration, Luminosity determination in pp collisions at $\sqrt{s} = 13 TeV$ using the ATLAS detector at the LHC. ATLAS-CONF-2019-021 (2019). <https://cds.cern.ch/record/2677054>
22. ATLAS Collaboration, The new LUCID-2 detector for luminosity measurement and monitoring in ATLAS. JINST **13**, P07017 (2018)
23. ATLAS Collaboration, Performance of electron and photon triggers in ATLAS during LHC Run 2. Eur. Phys. J. C **80**, 47 (2020). [arXiv:1909.00761](https://arxiv.org/abs/1909.00761) [hep-ex]
24. ATLAS Collaboration, Performance of the ATLAS muon triggers in Run 2. JINST **15**, P09015 (2020). [arXiv:2004.13447](https://arxiv.org/abs/2004.13447) [hep-ex]
25. GEANT4 Collaboration, S. Agostinelli et al., Geant4—a simulation toolkit. Nucl. Instrum. Methods A **506**, 250 (2003)
26. ATLAS Collaboration, The ATLAS simulation infrastructure. Eur. Phys. J. C **70**, 823 (2010). [arXiv:1005.4568](https://arxiv.org/abs/1005.4568) [physics.ins-det]
27. ATLAS Collaboration, The simulation principle and performance of the ATLAS fast calorimeter simulation FastCaloSim. ATL-PHYS-PUB-2010-013 (2010). <https://cds.cern.ch/record/1300517>
28. ATLAS Collaboration, Fast Simulation for ATLAS: Atfast-II and ISF, ATL-SOFT-PROC-2012-065 (2012). [http://cds.cern.ch/record/1458503](https://cds.cern.ch/record/1458503)

29. T. Sjöstrand, S. Mrenna, P. Skands, A brief introduction to PYTHIA 8.1. *Comput. Phys. Commun.* **178**, 852 (2008). [arXiv:7103820 \[hep-ph\]](#)
30. ATLAS Collaboration, The Pythia 8 A3 tune description of ATLAS minimum bias and inelastic measurements incorporating the Donnachie-Landshoff diffractive model, ATL-PHYS-PUB-2016-017 (2016). <https://cds.cern.ch/record/2206965>
31. R.D. Ball et al., Parton distributions with LHC data. *Nucl. Phys. B* **867**, 244 (2013). [arXiv:1207.1303 \[hep-ph\]](#)
32. R. Coimbra, A. Onofre, R. Santos, M. Won, METop—a generator for single top production via FCNC interactions. *Eur. Phys. J. C* **72**, 2222 (2012). [arXiv:1207.7026 \[hep-ph\]](#)
33. R. Guedes, R. Santos, M. Won, Limits on strong flavor changing neutral current top couplings at the LHC. *Phys. Rev. D* **88**, 114011 (2013). [arXiv:1308.4723 \[hep-ph\]](#)
34. S. Frixione, E. Laenen, P. Motylinski, B.R. Webber, Angular correlations of lepton pairs from vector boson and top quark decays in Monte Carlo simulations. *JHEP* **04**, 081 (2007). [arXiv:hep-ph/0702198](#)
35. P. Artoisenet, R. Frederix, O. Mattelaer, R. Rietkerk, Automatic spin-entangled decays of heavy resonances in Monte Carlo simulations. *JHEP* **03**, 015 (2013). [arXiv:1212.3460 \[hep-ph\]](#)
36. J. Gao et al., CT10 next-to-next-to-leading order global analysis of QCD. *Phys. Rev. D* **89**, 033009 (2014). [arXiv:1302.6246 \[hep-ph\]](#)
37. T. Sjöstrand et al., An introduction to PYTHIA 8.2. *Comput. Phys. Commun.* **191**, 159 (2015). [arXiv:1410.3012 \[hep-ph\]](#)
38. ATLAS Collaboration, ATLAS Pythia 8 tunes to 7 TeV data. ATL-PHYS-PUB-2014-021 (2014). <https://cds.cern.ch/record/1966419>
39. M. Bähr et al., Herwig++ physics and manual. *Eur. Phys. J. C* **58**, 639 (2008). [arXiv:0803.0883 \[hep-ph\]](#)
40. J. Bellm et al., Herwig 7.0/Herwig++ 3.0 release note. *Eur. Phys. J. C* **76**, 196 (2016). [arXiv:1512.01178 \[hep-ph\]](#)
41. P. Nason, A new method for combining NLO QCD with shower Monte Carlo algorithms. *JHEP* **11**, 040 (2004). [arXiv:hep-ph/0409146](#)
42. S. Frixione, P. Nason, G. Ridolfi, A positive-weight next-to-leading-order Monte Carlo for heavy flavour hadroproduction. *JHEP* **09**, 126 (2007). [arXiv:0707.3088 \[hep-ph\]](#)
43. S. Frixione, P. Nason, C. Oleari, Matching NLO QCD computations with parton shower simulations: the POWHEG method. *JHEP* **11**, 070 (2007). [arXiv:0709.2092 \[hep-ph\]](#)
44. S. Alioli, P. Nason, C. Oleari, E. Re, NLO single-top production matched with shower in POWHEG: s- and t-channel contributions. *JHEP* **09**, 111 (2009). [arXiv:0907.4076 \[hep-ph\]](#). Erratum: *JHEP* **02**, 011 (2010)
45. S. Alioli, P. Nason, C. Oleari, E. Re, A general framework for implementing NLO calculations in shower Monte Carlo programs: the POWHEG BOX. *JHEP* **06**, 043 (2010). [arXiv:1002.2581 \[hep-ph\]](#)
46. E. Re, Single-top Wt-channel production matched with parton showers using the POWHEG method. *Eur. Phys. J. C* **71**, 1547 (2011). [arXiv:1009.2450 \[hep-ph\]](#)
47. R. Frederix, E. Re, P. Torrielli, Single-top t-channel hadroproduction in the four-flavour scheme with POWHEG and aMC@NLO. *JHEP* **09**, 130 (2012). [arXiv:1207.5391 \[hep-ph\]](#)
48. R.D. Ball et al., Parton distributions for the LHC run II. *JHEP* **04**, 040 (2015). [arXiv:1410.8849 \[hep-ph\]](#)
49. ATLAS Collaboration, Studies on top-quark Monte Carlo modelling for Top2016, ATL-PHYS-PUB-2016-020 (2016). <https://cds.cern.ch/record/2216168>
50. S. Frixione, E. Laenen, P. Motylinski, C. White, B.R. Webber, Single-top hadroproduction in association with a W boson. *JHEP* **07**, 029 (2008). [arXiv:0805.3067 \[hep-ph\]](#)
51. D.J. Lange, The EvtGen particle decay simulation package. *Nucl. Instrum. Methods A* **462**, 152 (2001)
52. M. Czakon, A. Mitov, Top++: a program for the calculation of the top-pair cross-section at hadron colliders. *Comput. Phys. Commun.* **185**, 2930 (2014). [arXiv:1112.5675 \[hep-ph\]](#)
53. M. Aliev et al., HATHOR—HADronic Top and Heavy quarks cross section calculator. *Comput. Phys. Commun.* **182**, 1034 (2011). [arXiv:1007.1327 \[hep-ph\]](#)
54. P. Kant et al., HatHor for single top-quark production: updated predictions and uncertainty estimates for single top-quark production in hadronic collisions. *Comput. Phys. Commun.* **191**, 74 (2015). [arXiv:1406.4403 \[hep-ph\]](#)
55. N. Kidonakis, Two-loop soft anomalous dimensions for single top quark associated production with a W- or H-. *Phys. Rev. D* **82**, 054018 (2010). [arXiv:1005.4451 \[hep-ph\]](#)
56. N. Kidonakis, ‘Top Quark Production’, in *Proceedings, Helmholtz International Summer School on Physics of Heavy Quarks and Hadrons (HQ 2013)* (JINR, Dubna, Russia, 15th–28th July 2013), p. 139. [arXiv:1311.0283 \[hep-ph\]](#)
57. E. Bothmann et al., Event generation with Sherpa 2.2. *SciPost Phys.* **7**, 034 (2019). [arXiv:1905.09127 \[hep-ph\]](#)
58. T. Gleisberg, S. Höche, Comix, a new matrix element generator. *JHEP* **12**, 039 (2008). [arXiv:0808.3674 \[hep-ph\]](#)
59. F. Buccioni et al., OpenLoops 2. *Eur. Phys. J. C* **79**, 866 (2019). [arXiv:1907.13071 \[hep-ph\]](#)
60. F. Cascioli, P. Maierhöfer, S. Pozzorini, Scattering amplitudes with open loops. *Phys. Rev. Lett.* **108**, 111601 (2012). [arXiv:1111.5206 \[hep-ph\]](#)
61. A. Denner, S. Dittmaier, L. Hofer, Collier: a fortran-based complex one-loop library in extended regularizations. *Comput. Phys. Commun.* **212**, 220 (2017). [arXiv:1604.06792 \[hep-ph\]](#)
62. S. Schumann, F. Krauss, A parton shower algorithm based on Catani-Seymour dipole factorisation. *JHEP* **03**, 038 (2008). [arXiv:0709.1027 \[hep-ph\]](#)
63. J.-C. Winter, F. Krauss, G. Soff, A modified cluster-hadronization model. *Eur. Phys. J. C* **36**, 381 (2004). [arXiv:hep-ph/0311085](#)
64. S. Höche, F. Krauss, M. Schönherr, F. Siegert, A critical appraisal of NLO+PS matching methods. *JHEP* **09**, 049 (2012). [arXiv:1111.1220 \[hep-ph\]](#)
65. S. Catani, F. Krauss, B.R. Webber, R. Kuhn, QCD Matrix Elements + Parton Showers. *JHEP* **11**, 063 (2001). [arXiv:hep-ph/0109231](#)
66. S. Höche, F. Krauss, S. Schumann, F. Siegert, QCD matrix elements and truncated showers. *JHEP* **05**, 053 (2009). [arXiv:0903.1219 \[hep-ph\]](#)
67. S. Höche, F. Krauss, M. Schönherr, F. Siegert, QCD matrix elements + parton showers. The NLO case. *JHEP* **04**, 027 (2013). [arXiv:1207.5030 \[hep-ph\]](#)
68. C. Anastasiou, L.J. Dixon, K. Melnikov, F. Petriello, High precision QCD at hadron colliders: electroweak gauge boson rapidity distributions at next-to-next-to leading order. *Phys. Rev. D* **69**, 094008 (2004). [arXiv:hep-ph/0312266](#)
69. R. Gavin, Y. Li, F. Petriello, S. Quackenbush, FEWZ 2.0: a code for hadronic Z production at next-to-next-to-leading order. *Comput. Phys. Commun.* **182**, 2388 (2011)
70. ATLAS Collaboration, Vertex Reconstruction Performance of the ATLAS Detector at $\sqrt{s} = 13\text{TeV}$. ATL-PHYS-PUB-2015-026 (2015). <https://cds.cern.ch/record/2037717>
71. ATLAS Collaboration, Electron and photon performance measurements with the ATLAS detector using the 2015-2017 LHC proton-proton collision data. *JINST* **14**, P12006 (2019). [arXiv:1908.00005 \[hep-ex\]](#)
72. ATLAS Collaboration, Muon reconstruction and identification efficiency in ATLAS using the full Run 2 pp collision data set at $\sqrt{s} = 13\text{TeV}$. *Eur. Phys. J. C* **81**, 578 (2021). [arXiv:2012.00578 \[hep-ex\]](#)
73. ATLAS Collaboration, Properties of jets and inputs to jet reconstruction and calibration with the ATLAS detector using proton-

- proton collisions at $\sqrt{s} = 13\text{TeV}$. ATL-PHYS-PUB-2015-036 (2015). <https://cds.cern.ch/record/2044564>
74. ATLAS Collaboration, Topological cell clustering in the ATLAS calorimeters and its performance in LHC Run 1. *Eur. Phys. J. C* **77**, 490 (2017). [arXiv:1603.02934](https://arxiv.org/abs/1603.02934) [hep-ex]
 75. M. Cacciari, G.P. Salam, G. Soyez, The anti-kt jet clustering algorithm. *JHEP* **04**, 063 (2008). [arXiv:0802.1189](https://arxiv.org/abs/0802.1189) [hep-ph]
 76. M. Cacciari, G.P. Salam, G. Soyez, FastJet user manual. *Eur. Phys. J. C* **72**, 1896 (2012). [arXiv:1111.6097](https://arxiv.org/abs/1111.6097) [hep-ph]
 77. ATLAS Collaboration, Jet energy scale measurements and their systematic uncertainties in proton-proton collisions at $\sqrt{s} = 13\text{TeV}$ with the ATLAS detector. *Phys. Rev. D* **96**, 072002 (2017). [arXiv:1703.09665](https://arxiv.org/abs/1703.09665) [hep-ex]
 78. ATLAS Collaboration, Performance of pile-up mitigation techniques for jets in pp collisions at $\sqrt{s} = 8\text{TeV}$ using the ATLAS detector. *Eur. Phys. J. C* **76**, 581 (2016). [arXiv:1510.03823](https://arxiv.org/abs/1510.03823) [hep-ex]
 79. ATLAS Collaboration, Identification and rejection of pile-up jets at high pseudorapidity with the ATLAS detector. *Eur. Phys. J. C* **77**, 580 (2017). [arXiv:1705.02211](https://arxiv.org/abs/1705.02211) [hep-ex]. Erratum: *Eur. Phys. J. C* **77**, 712 (2017)
 80. ATLAS Collaboration, ATLAS b-jet identification performance and efficiency measurement with $t\bar{t}$ events in pp collisions at $\sqrt{s} = 13\text{TeV}$. *Eur. Phys. J. C* **79**, 970 (2019). [arXiv:1907.05120](https://arxiv.org/abs/1907.05120) [hep-ex]
 81. ATLAS Collaboration, Performance of b-jet identification in the ATLAS experiment, JINST 11 (2016) P04008, [arXiv:1512.01094](https://arxiv.org/abs/1512.01094) [hep-ex]
 82. ATLAS Collaboration, Performance of missing transverse momentum reconstruction with the ATLAS detector using proton-proton collisions at $\sqrt{s} = 13\text{TeV}$. *Eur. Phys. J. C* **78**, 903 (2018). [arXiv:1802.08168](https://arxiv.org/abs/1802.08168) [hep-ex]
 83. ATLAS Collaboration, Estimation of non-prompt and fake lepton backgrounds in final states with top quarks produced in proton-proton collisions at $\sqrt{s} = 8\text{TeV}$ with the ATLAS Detector. ATLAS-CONF-2014-058 (2014). <https://cds.cern.ch/record/1951336>
 84. M. Feindt, A neural Bayesian estimator for conditional probability densities (2004). [arXiv:physics/0402093](https://arxiv.org/abs/physics/0402093)
 85. M. Feindt, U. Kerzel, The NeuroBayes neural network package. *Nucl. Instrum. Methods A* **559**, 190 (2006)
 86. ATLAS Collaboration, Jet energy measurement with the ATLAS detector in proton-proton collisions at $\sqrt{s} = 7\text{TeV}$. *Eur. Phys. J. C* **73**, 2304 (2013). [arXiv:1112.6426](https://arxiv.org/abs/1112.6426) [hep-ex]
 87. E. Bothmann, M. Schönherr, S. Schumann, Reweighting QCD matrix-element and parton-shower calculations. *Eur. Phys. J. C* **76**, 590 (2016). [arXiv:1606.08753](https://arxiv.org/abs/1606.08753) [hep-ph]
 88. L. Harland-Lang, A. Martin, P. Motylinski, R. Thorne, Parton distributions in the LHC era: MMHT 2014 PDFs. *Eur. Phys. J. C* **75**, 204 (2015). [arXiv:1412.3989](https://arxiv.org/abs/1412.3989) [hep-ph]
 89. J. Alwall, M. Herquet, F. Maltoni, O. Mattelaer, T. Stelzer, MadGraph 5: going beyond. *JHEP* **06**, 128 (2011). [arXiv:1106.0522](https://arxiv.org/abs/1106.0522) [hep-ph]
 90. J. Butterworth et al., PDF4LHC recommendations for LHC Run II. *J. Phys. G* **43**, 023001 (2016). [arXiv:1510.03865](https://arxiv.org/abs/1510.03865) [hep-ph]
 91. R.J. Barlow, C. Beeston, Fitting using finite Monte Carlo samples. *Comput. Phys. Commun.* **77**, 219 (1993)
 92. ATLAS Collaboration, Measurements of the production cross-section for a Z boson in association with b-jets in proton-proton collisions at $\sqrt{s} = 13\text{TeV}$ with the ATLAS detector. *JHEP* **07**, 044 (2020). [arXiv:2003.11960](https://arxiv.org/abs/2003.11960) [hep-ex]
 93. A. L. Read, Presentation of search results: the CL_s technique. *J. Phys. G* **28**, 2693 (2002). <http://stacks.iop.org/0954-3899/28/i=10/a=313>
 94. T. Junk, Confidence level computation for combining searches with small statistics. *Nucl. Instrum. Methods A* **434**, 435 (1999). <http://www.sciencedirect.com/science/article/pii/S0168900299004982>
 95. W. Verkerke, D. Kirkby, The RooFit toolkit for data modeling (2003). [arXiv:physics/0306116](https://arxiv.org/abs/physics/0306116)
 96. A. Alloul, N.D. Christensen, C. Degrande, C. Duhr, B. Fuks, FeynRules 2.0—a complete toolbox for tree-level phenomenology. *Comput. Phys. Commun.* **185**, 2250 (2014). <http://www.sciencedirect.com/science/article/pii/S0010465514001350>
 97. CMS Collaboration, Search for new physics in top quark production in dilepton final states in proton-proton collisions at $\sqrt{s} = 13\text{TeV}$. *Eur. Phys. J. C* **79**, 886 (2019). [arXiv:1903.11144](https://arxiv.org/abs/1903.11144) [hep-ex]
 98. G. Durieux, F. Maltoni, C. Zhang, Global approach to top-quark flavor-changing interactions. *Phys. Rev. D* **91**, 074017 (2015). [arXiv:1412.7166](https://arxiv.org/abs/1412.7166) [hep-ph]
 99. ATLAS Collaboration, ATLAS Computing Acknowledgements, ATL-SOFT-PUB-2021-003. <https://cds.cern.ch/record/2776662>

ATLAS Collaboration

G. Aad⁹⁸, B. Abbott¹²⁴, D. C. Abbott⁹⁹, A. Abed Abud³⁴, K. Abeling⁵¹, D. K. Abhayasinghe⁹¹, S. H. Abidi²⁷, A. Aboulhorma^{33c}, H. Abramowicz¹⁵⁷, H. Abreu¹⁵⁶, Y. Abulaiti⁵, A. C. Abusleme Hoffman^{142a}, B. S. Acharya^{64a,64b,o}, B. Achkar⁵¹, L. Adam⁹⁶, C. Adam Bourdarios⁴, L. Adamczyk^{81a}, L. Adamek¹⁶², S. V. Addepalli²⁴, J. Adelman¹¹⁶, A. Adiguzel^{11c,ac}, S. Adorni⁵², T. Adye¹³⁹, A. A. Affolder¹⁴¹, Y. Afik³⁴, C. Agapopoulou⁶², M. N. Agaras¹², J. Agarwala^{68a,68b}, A. Aggarwal¹¹⁴, C. Agheorghiesei^{25c}, J. A. Aguilar-Saavedra^{135a,135f,ab}, A. Ahmad³⁴, F. Ahmadov⁷⁷, W. S. Ahmed¹⁰⁰, X. Ai⁴⁴, G. Aielli^{71a,71b}, I. Aizenberg¹⁷⁵, S. Akatsuka⁸³, M. Akbiyik⁹⁶, T. P. A. Åkesson⁹⁴, A. V. Akimov¹⁰⁷, K. Al Houry³⁷, G. L. Alberghi^{21b}, J. Albert¹⁷¹, P. Albicocco⁴⁹, M. J. Alconada Verzini⁸⁶, S. Alderweireldt⁴⁸, M. Aleksa³⁴, I. N. Aleksandrov⁷⁷, C. Alexa^{25b}, T. Alexopoulos⁹, A. Alfonsi¹¹⁵, F. Alfonsi^{21b}, M. Alhroob¹²⁴, B. Ali¹³⁷, S. Ali¹⁵⁴, M. Aliev¹⁶¹, G. Alimonti^{66a}, C. Allaire³⁴, B. M. M. Allbrooke¹⁵², P. P. Allport¹⁹, A. Aloisio^{67a,67b}, F. Alonso⁸⁶, C. Alpigiani¹⁴⁴, E. Alunno Camelia^{71a,71b}, M. Alvarez Estevez⁹⁵, M. G. Alvigi^{67a,67b}, Y. Amaral Coutinho^{78b}, A. Ambler¹⁰⁰, L. Ambroz¹³⁰, C. Amelung³⁴, D. Amidei¹⁰², S. P. Amor Dos Santos^{135a}, S. Amoroso⁴⁴, K. R. Amos¹⁶⁹, C. S. Amrouche⁵², V. Ananiev¹²⁹, C. Anastopoulos¹⁴⁵, N. Andari¹⁴⁰, T. Andeen¹⁰, J. K. Anders¹⁸, S. Y. Andrean^{43a,43b}, A. Andreatta^{66a,66b}, S. Angelidakis⁸, A. Angerami³⁷, A. V. Anisenkov^{117a,117b}, A. Annovi^{69a}, C. Antel⁵², M. T. Anthony¹⁴⁵, E. Antipov¹²⁵, M. Antonelli⁴⁹, D. J. A. Antrim¹⁶, F. Anulli^{70a}, M. Aoki⁷⁹, J. A. Aparisi Pozo¹⁶⁹, M. A. Aparo¹⁵², L. Aperio Bella⁴⁴, N. Aranzabal³⁴, V. Araujo Ferraz^{78a}, C. Arcangeletti⁴⁹, A. T. H. Arce⁴⁷, E. Arena⁸⁸, J-F. Arguin¹⁰⁶, S. Argyropoulos⁵⁰, J.-H. Arling⁴⁴, A. J. Armbruster³⁴, A. Armstrong¹⁶⁶, O. Arnaez¹⁶², H. Arnold³⁴, Z. P. Arrubarrena Tame¹¹⁰, G. Artoni¹³⁰, H. Asada¹¹², K. Asai¹²², S. Asai¹⁵⁹, N. A. Asbah⁵⁷, E. M. Asimakopoulou¹⁶⁷, L. Asquith¹⁵², J. Assahsah^{33d}, K. Assamagan²⁷, R. Astalos^{26a}, R. J. Atkin^{31a}, M. Atkinson¹⁶⁸, N. B. Atlay¹⁷, H. Atmani^{58b}, P. A. Atlasiddha¹⁰², K. Augsten¹³⁷, S. Auricchio^{67a,67b}, V. A. Austrup¹⁷⁷, G. Avner¹⁵⁶, G. Avolio³⁴, M. K. Ayoub^{13c}, G. Azuelos^{106,aj}, D. Babal^{26a}, H. Bachacou¹⁴⁰, K. Bachas¹⁵⁸, A. Bachi³², F. Backman^{43a,43b}, A. Badea⁵⁷, P. Bagnaia^{70a,70b}, H. Bahrasemani¹⁴⁸, A. J. Bailey¹⁶⁹, V. R. Bailey¹⁶⁸, J. T. Baines¹³⁹, C. Bakalis⁹, O. K. Baker¹⁷⁸, P. J. Bakker¹¹⁵, E. Bakos¹⁴, D. Bakshi Gupta⁷, S. Balaji¹⁵³, R. Balasubramanian¹¹⁵, E. M. Baldin^{117a,117b}, P. Balek¹³⁸, E. Ballabene^{66a,66b}, F. Balli¹⁴⁰, L. M. Baltes^{59a}, W. K. Balunas¹³⁰, J. Balz⁹⁶, E. Banas⁸², M. Bandieramonte¹³⁴, A. Bandyopadhyay²², S. Bansal²², L. Barak¹⁵⁷, E. L. Barberio¹⁰¹, D. Barberis^{53a,53b}, M. Barbero⁹⁸, G. Barbour⁹², K. N. Barends^{31a}, T. Barillari¹¹¹, M.-S. Barisits³⁴, J. Barkeloo¹²⁷, T. Barklow¹⁴⁹, B. M. Barnett¹³⁹, R. M. Barnett¹⁶, A. Baroncelli^{58a}, G. Barone²⁷, A. J. Barr¹³⁰, L. Barranco Navarro^{43a,43b}, F. Barreiro⁹⁵, J. Barreiro Guimarães da Costa^{13a}, U. Barron¹⁵⁷, S. Barsov¹³³, F. Bartels^{59a}, R. Bartoldus¹⁴⁹, G. Bartolini⁹⁸, A. E. Barton⁸⁷, P. Bartos^{26a}, A. Basalae⁴⁴, A. Basan⁹⁶, M. Baselga⁴⁴, I. Bashta^{72a,72b}, A. Bassalat^{62,ag}, M. J. Basso¹⁶², C. R. Basson⁹⁷, R. L. Bates⁵⁵, S. Batlamous^{33c}, J. R. Batley³⁰, B. Batool¹⁴⁷, M. Battaglia¹⁴¹, M. Baucé^{70a,70b}, F. Bauer^{140,*}, P. Bauer²², H. S. Bawa²⁹, A. Bayirli^{11c}, J. B. Beacham⁴⁷, T. Beau¹³¹, P. H. Beauchemin¹⁶⁵, F. Becherer⁵⁰, P. Bechtel²², H. P. Beck^{18,q}, K. Becker¹⁷³, C. Becot⁴⁴, A. J. Beddall^{11a}, V. A. Bednyakov⁷⁷, C. P. Bee¹⁵¹, T. A. Beermann³⁴, M. Begalli^{78b}, M. Begel²⁷, A. Behara¹⁵¹, J. K. Behr⁴⁴, C. Beirao Da Cruz E Silva³⁴, J. F. Beirer^{51,34}, F. Beisiegel²², M. Belfkir⁴, G. Bella¹⁵⁷, L. Bellagamba^{21b}, A. Bellerive³², P. Bellos¹⁹, K. Beloborodov^{117a,117b}, K. Belotskiy¹⁰⁸, N. L. Belyaev¹⁰⁸, D. Benckekroun^{33a}, Y. Benhammou¹⁵⁷, D. P. Benjamin²⁷, M. Benoit²⁷, J. R. Bensinger²⁴, S. Bentvelsen¹¹⁵, L. Beresford³⁴, M. Beretta⁴⁹, D. Berge¹⁷, E. Bergeas Kuutmann¹⁶⁷, N. Berger⁴, B. Bergmann¹³⁷, L. J. Bergsten²⁴, J. Beringer¹⁶, S. Berlendis⁶, G. Bernardi¹³¹, C. Bernius¹⁴⁹, F. U. Bernlochner²², T. Berry⁹¹, P. Berta¹³⁸, A. Berthold⁴⁶, I. A. Bertram⁸⁷, O. Bessidskaia Bylund¹⁷⁷, S. Bethke¹¹¹, A. Betti⁴⁰, A. J. Bevan⁹⁰, S. Bhatta¹⁵¹, D. S. Bhattacharya¹⁷², P. Bhattarai²⁴, V. S. Bhopatkar⁵, R. Bi¹³⁴, R. M. Bianchi¹³⁴, O. Biebel¹¹⁰, R. Bielski¹²⁷, N. V. Biesuz^{69a,69b}, M. Biglietti^{72a}, T. R. V. Billoud¹³⁷, M. Bindi⁵¹, A. Bingul^{11d}, C. Bini^{70a,70b}, S. Biondi^{21a,21b}, A. Biondini⁸⁸, C. J. Birch-sykes⁹⁷, G. A. Bird^{19,139}, M. Birman¹⁷⁵, T. Bisanz³⁴, J. P. Biswal², D. Biswas^{176,j}, A. Bitadze⁹⁷, C. Bittrich⁴⁶, K. Björke¹²⁹, I. Bloch⁴⁴, C. Blocker²⁴, A. Blue⁵⁵, U. Blumenschein⁹⁰, J. Blumenthal⁹⁶, G. J. Bobbink¹¹⁵, V. S. Bobrovnikov^{117a,117b}, M. Boehler⁵⁰, D. Bogavac¹², A. G. Bogdanchikov^{117a,117b}, C. Bohm^{43a}, V. Boisvert⁹¹, P. Bokan⁴⁴, T. Bold^{81a}, M. Bomben¹³¹, M. Bona⁹⁰, M. Boonekamp¹⁴⁰, C. D. Booth⁹¹, A. G. Borbély⁵⁵, H. M. Borecka-Bielska¹⁰⁶, L. S. Borgna⁹², G. Borissov⁸⁷, D. Bortoletto¹³⁰, D. Boscherini^{21b}, M. Bosman¹², J. D. Bossio Sola³⁴, K. Bouaouda^{33a}, J. Boudreau¹³⁴, E. V. Bouhova-Thacker⁸⁷, D. Boumediene³⁶, R. Bouquet¹³¹, A. Boveia¹²³

J. Dickinson¹⁶, M. Didenko¹⁶⁹, E. B. Diehl¹⁰², J. Dietrich¹⁷, S. Díez Cornell⁴⁴, C. Díez Pardos¹⁴⁷, A. Dimitrievska¹⁶, W. Ding^{13b}, J. Dingfelder²², I-M. Dinu^{25b}, S. J. Dittmeier^{59b}, F. Dittus³⁴, F. Djama⁹⁸, T. Djobava^{155b}, J. I. Djuvsland¹⁵, M. A. B. Do Vale¹⁴³, D. Dodsworth²⁴, C. Doglioni⁹⁴, J. Dolejsi¹³⁸, Z. Dolezal¹³⁸, M. Donadelli^{78c}, B. Dong^{58c}, J. Donini³⁶, A. D'onofrio^{13c}, M. D'Onofrio⁸⁸, J. Dopke¹³⁹, A. Doria^{67a}, M. T. Dova⁸⁶, A. T. Doyle⁵⁵, E. Drechsler¹⁴⁸, E. Dreyer¹⁴⁸, T. Dreyer⁵¹, A. S. Drobac¹⁶⁵, D. Du^{58a}, T. A. du Pree¹¹⁵, F. Dubinin¹⁰⁷, M. Dubovsky^{26a}, A. Dubreuil⁵², E. Duchovni¹⁷⁵, G. Duckeck¹¹⁰, O. A. Ducu^{25b,34}, D. Duda¹¹¹, A. Dudarev³⁴, M. D'uffizi⁹⁷, L. Duflo⁶², M. Dührssen³⁴, C. Dülsen¹⁷⁷, A. E. Dumitriu^{25b}, M. Dunford^{59a}, S. Dungs⁴⁵, K. Dunne^{43a,43b}, A. Duperrin⁹⁸, H. Duran Yildiz^{3a}, M. Düren⁵⁴, A. Durglishvili^{155b}, B. Dutta⁴⁴, B. L. Dwyer¹¹⁶, G. I. Dyckes¹⁶, M. Dyndal^{81a}, S. Dysch⁹⁷, B. S. Dziedzic⁸², B. Eckerova^{26a}, M. G. Eggleston⁴⁷, E. Egidio Purcino De Souza^{78b}, L. F. Ehrke⁵², T. Eifert⁷, G. Eigen¹⁵, K. Einsweiler¹⁶, T. Ekelof¹⁶⁷, Y. El Ghazali^{33b}, H. El Jarrari^{33e}, A. El Moussaouy^{33a}, V. Ellajosyula¹⁶⁷, M. Ellert¹⁶⁷, F. Ellinghaus¹⁷⁷, A. A. Elliot⁹⁰, N. Ellis³⁴, J. Elmsheuser²⁷, M. Elsing³⁴, D. Emelianov¹³⁹, A. Emerman³⁷, Y. Enari¹⁵⁹, J. Erdmann⁴⁵, A. Ereditato¹⁸, P. A. Erland⁸², M. Errenst¹⁷⁷, M. Escalier⁶², C. Escobar¹⁶⁹, O. Estrada Pastor¹⁶⁹, E. Etzion¹⁵⁷, G. Evans^{135a}, H. Evans⁶³, M. O. Evans¹⁵², A. Ezhilov¹³³, F. Fabbri⁵⁵, L. Fabbri^{21a,21b}, G. Facini¹⁷³, V. Fadeyev¹⁴¹, R. M. Fakhruddinov¹¹⁸, S. Falciano^{70a}, P. J. Falke²², S. Falke³⁴, J. Faltova¹³⁸, Y. Fan^{13a}, Y. Fang^{13a}, G. Fanourakis⁴², M. Fanti^{66a,66b}, M. Faraj^{58c}, A. Farbin⁷, A. Farilla^{72a}, E. M. Farina^{68a,68b}, T. Faroouque¹⁰³, S. M. Farrington⁴⁸, P. Farthouat³⁴, F. Fassi^{33e}, D. Fassouliotis⁸, M. Fauci Giannelli^{71a,71b}, W. J. Fawcett³⁰, L. Fayard⁶², O. L. Fedin^{133,p}, M. Feickert¹⁶⁸, L. Felgioni⁹⁸, A. Fell¹⁴⁵, C. Feng^{58b}, M. Feng^{13b}, M. J. Fenton¹⁶⁶, A. B. Fenyuk¹¹⁸, S. W. Ferguson⁴¹, J. Ferrando⁴⁴, A. Ferrari¹⁶⁷, P. Ferrari¹¹⁵, R. Ferrari^{68a}, D. Ferrere⁵², C. Ferretti¹⁰², F. Fiedler⁹⁶, A. Filipčić⁸⁹, F. Filthaut¹¹⁴, M. C. N. Fiolhais^{135a,135c,a}, L. Fiorini¹⁶⁹, F. Fischer¹⁴⁷, W. C. Fisher¹⁰³, T. Fitschen¹⁹, I. Fleck¹⁴⁷, P. Fleischmann¹⁰², T. Flick¹⁷⁷, B. M. Flierl¹¹⁰, L. Flores¹³², M. Flores^{31d}, L. R. Flores Castillo^{60a}, F. M. Follega^{73a,73b}, N. Fomin¹⁵, J. H. Foo¹⁶², B. C. Forland⁶³, A. Formica¹⁴⁰, F. A. Förster¹², A. C. Forti⁹⁷, E. Fortin⁹⁸, M. G. Foti¹³⁰, L. Fountas⁸, D. Fournier⁶², H. Fox⁸⁷, P. Francavilla^{69a,69b}, S. Francescato⁵⁷, M. Franchini^{21a,21b}, S. Franchino^{59a}, D. Francis³⁴, L. Franco⁴, L. Franconi¹⁸, M. Franklin⁵⁷, G. Frattari^{70a,70b}, A. C. Freegard⁹⁰, P. M. Freeman¹⁹, W. S. Freund^{78b}, E. M. Freundlich⁴⁵, D. Froidevaux³⁴, J. A. Frost¹³⁰, Y. Fu^{58a}, M. Fujimoto¹²², E. Fullana Torregrosa¹⁶⁹, J. Fuster¹⁶⁹, A. Gabrielli^{21a,21b}, A. Gabrielli³⁴, P. Gadov⁴⁴, G. Gagliardi^{53a,53b}, L. G. Gagnon¹⁶, G. E. Gallardo¹³⁰, E. J. Gallas¹³⁰, B. J. Gallop¹³⁹, R. Gamboa Goni⁹⁰, K. K. Gan¹²³, S. Ganguly¹⁵⁹, J. Gao^{58a}, Y. Gao⁴⁸, Y. S. Gao^{29,m}, F. M. Garay Walls^{142a}, C. García¹⁶⁹, J. E. García Navarro¹⁶⁹, J. A. García Pascual^{13a}, M. Garcia-Sciveres¹⁶, R. W. Gardner³⁵, D. Garg⁷⁵, R. B. Garg¹⁴⁹, S. Gargiulo⁵⁰, C. A. Garner¹⁶², V. Garonne¹²⁹, S. J. Gasiorowski¹⁴⁴, P. Gaspar^{78b}, G. Gaudio^{68a}, P. Gauzzi^{70a,70b}, I. L. Gavrilenko¹⁰⁷, A. Gavriluk¹¹⁹, C. Gay¹⁷⁰, G. Gaycken⁴⁴, E. N. Gazis⁹, A. A. Geanta^{25b}, C. M. Gee¹⁴¹, C. N. P. Gee¹³⁹, J. Geisen⁹⁴, M. Geisen⁹⁶, C. Gemme^{53b}, M. H. Genest⁵⁶, S. Gentile^{70a,70b}, S. George⁹¹, W. F. George¹⁹, T. Gerialis⁴², L. O. Gerlach⁵¹, P. Gessinger-Befurt³⁴, M. Ghasemi Bostanabad¹⁷¹, A. Ghosh¹⁶⁶, A. Ghosh⁷⁵, B. Giacobbe^{21b}, S. Giagu^{70a,70b}, N. Giangiacomi¹⁶², P. Giannetti^{69a}, A. Giannini^{67a,67b}, S. M. Gibson⁹¹, M. Gignac¹⁴¹, D. T. Gil^{81b}, B. J. Gilbert³⁷, D. Gillberg³², G. Gilles¹¹⁵, N. E. K. Gillwald⁴⁴, D. M. Gingrich^{2,aj}, M. P. Giordani^{64a,64c}, P. F. Giraud¹⁴⁰, G. Giugliarelli^{64a,64c}, D. Giugni^{66a}, F. Giulia^{71a,71b}, I. Gkialas^{8,h}, P. Gkoutoumis⁹, L. K. Gladilin¹⁰⁹, C. Glasman⁹⁵, G. R. Gledhill¹²⁷, M. Glisic¹²⁷, I. Gnesi^{39b,d}, M. Goblirsch-Kolb²⁴, D. Godin¹⁰⁶, S. Goldfarb¹⁰¹, T. Golling⁵², D. Golubkov¹¹⁸, J. P. Gombas¹⁰³, A. Gomes^{135a,135b}, R. Goncalves Gama⁵¹, R. Gonçalo^{135a,135c}, G. Gonella¹²⁷, L. Gonella¹⁹, A. Gongadze⁷⁷, F. Gonnella¹⁹, J. L. Gonski³⁷, S. González de la Hoz¹⁶⁹, S. Gonzalez Fernandez¹², R. Gonzalez Lopez⁸⁸, C. Gonzalez Renteria¹⁶, R. Gonzalez Suarez¹⁶⁷, S. Gonzalez-Sevilla⁵², G. R. Gonzalvo Rodriguez¹⁶⁹, R. Y. González Andana^{142a}, L. Goossens³⁴, N. A. Gorasia¹⁹, P. A. Gorbounov¹¹⁹, H. A. Gordon²⁷, B. Gorini³⁴, E. Gorini^{65a,65b}, A. Gorišek⁸⁹, A. T. Goshaw⁴⁷, M. I. Gostkin⁷⁷, C. A. Gottardo¹¹⁴, M. Goughri^{33b}, V. Goumarre⁴⁴, A. G. Goussiou¹⁴⁴, N. Govender^{31c}, C. Goy⁴, I. Grabowska-Bold^{81a}, K. Graham³², E. Gramstad¹²⁹, S. Grancagnolo¹⁷, M. Grandi¹⁵², V. Gratchev¹³³, P. M. Gravila^{25f}, F. G. Gravili^{65a,65b}, H. M. Gray¹⁶, C. Grefe²², I. M. Gregor⁴⁴, P. Grenier¹⁴⁹, K. Grevtsov⁴⁴, C. Grieco¹², N. A. Grieser¹²⁴, A. A. Grillo¹⁴¹, K. Grimm^{29,1}, S. Grinstein^{12,v}, J.-F. Grivaz⁶², S. Groh⁹⁶, E. Gross¹⁷⁵, J. Grosse-Knetter⁵¹, C. Grud¹⁰², A. Grummer¹¹³, J. C. Grundy¹³⁰, L. Guan¹⁰², W. Guan¹⁷⁶, C. Gubbels¹⁷⁰, J. Guenther³⁴, J. G. R. Guerrero Rojas¹⁶⁹, F. Guescini¹¹¹, D. Guest¹⁷, R. Gugel⁹⁶, A. Guida⁴⁴, T. Guillemain⁴, S. Guindon³⁴, J. Guo^{58c}, L. Guo⁶², Y. Guo¹⁰², R. Gupta⁴⁴, S. Gurbuz²², G. Gustavino¹²⁴, M. Guth⁵², P. Gutierrez¹²⁴

L. F. Gutierrez Zagazeta¹³², C. Gutsche⁹², C. Guyot¹⁴⁰, C. Gwenlan¹³⁰, C. B. Gwilliam⁸⁸, E. S. Haaland¹²⁹, A. Haas¹²¹, M. Habedank⁴⁴, C. Haber¹⁶, H. K. Hadavand⁷, A. Hadeef⁹⁶, S. Hadzic¹¹¹, M. Haleem¹⁷², J. Haley¹²⁵, J. J. Hall¹⁴⁵, G. Halladjian¹⁰³, G. D. Hallewell⁹⁸, L. Halser¹⁸, K. Hamano¹⁷¹, H. Hamdaoui^{33e}, M. Hamer²², G. N. Hamity⁴⁸, K. Han^{58a}, L. Han^{13c}, L. Han^{58a}, S. Han¹⁶, Y. F. Han¹⁶², K. Hanagaki^{79,t}, M. Hance¹⁴¹, M. D. Hank³⁵, R. Hankache⁹⁷, E. Hansen⁹⁴, J. B. Hansen³⁸, J. D. Hansen³⁸, M. C. Hansen²², P. H. Hansen³⁸, K. Hara¹⁶⁴, T. Harenberg¹⁷⁷, S. Harkusha¹⁰⁴, Y. T. Harris¹³⁰, P. F. Harrison¹⁷³, N. M. Hartman¹⁴⁹, N. M. Hartmann¹¹⁰, Y. Hasegawa¹⁴⁶, A. Hasib⁴⁸, S. Hassani¹⁴⁰, S. Haug¹⁸, R. Hauser¹⁰³, M. Havranek¹³⁷, C. M. Hawkes¹⁹, R. J. Hawkins³⁴, S. Hayashida¹¹², D. Hayden¹⁰³, C. Hayes¹⁰², R. L. Hayes¹⁷⁰, C. P. Hays¹³⁰, J. M. Hays⁹⁰, H. S. Hayward⁸⁸, S. J. Haywood¹³⁹, F. He^{58a}, Y. He¹⁶⁰, Y. He¹³¹, M. P. Heath⁴⁸, V. Hedberg⁹⁴, A. L. Heggelund¹²⁹, N. D. Hehir⁹⁰, C. Heidegger⁵⁰, K. K. Heidegger⁵⁰, W. D. Heidorn⁷⁶, J. Heilman³², S. Heim⁴⁴, T. Heim¹⁶, B. Heinemann^{44,ab}, J. G. Heinlein¹³², J. J. Heinrich¹²⁷, L. Heinrich³⁴, J. Hejbal¹³⁶, L. Helary⁴⁴, A. Held¹²¹, C. M. Helling¹⁴¹, S. Hellman^{43a,43b}, C. Helsen³⁴, R. C. W. Henderson⁸⁷, L. Henkelmann³⁰, A. M. Henriques Correia³⁴, H. Herde¹⁴⁹, Y. Hernández Jiménez¹⁵¹, H. Herr⁹⁶, M. G. Herrmann¹¹⁰, T. Herrmann⁴⁶, G. Herten⁵⁰, R. Hertenberger¹¹⁰, L. Hervás³⁴, N. P. Hessey^{163a}, H. Hibi⁸⁰, S. Higashino⁷⁹, E. Higón-Rodríguez¹⁶⁹, K. H. Hiller⁴⁴, S. J. Hillier¹⁹, M. Hils⁴⁶, I. Hinchliffe¹⁶, F. Hinterkeuser²², M. Hirose¹²⁸, S. Hirose¹⁶⁴, D. Hirschbuehl¹⁷⁷, B. Hiti⁸⁹, O. Hladik¹³⁶, J. Hobbs¹⁵¹, R. Hobincu^{25e}, N. Hod¹⁷⁵, M. C. Hodgkinson¹⁴⁵, B. H. Hodgkinson³⁰, A. Hoecker³⁴, J. Hofer⁴⁴, D. Hohn⁵⁰, T. Holm²², T. R. Holmes³⁵, M. Holzbock¹¹¹, L. B. A. H. Hommels³⁰, B. P. Honan⁹⁷, J. Hong^{58c}, T. M. Hong¹³⁴, Y. Hong⁵¹, J. C. Honig⁵⁰, A. Hönle¹¹¹, B. H. Hooberman¹⁶⁸, W. H. Hopkins⁵, Y. Horii¹¹², L. A. Horyn³⁵, S. Hou¹⁵⁴, J. Howarth⁵⁵, J. Hoya⁸⁶, M. Hrabovsky¹²⁶, A. Hrynevich¹⁰⁵, T. Hryn'ova⁴, P. J. Hsu⁶¹, S.-C. Hsu¹⁴⁴, Q. Hu³⁷, S. Hu^{58c}, Y. F. Hu^{13a,13d,al}, D. P. Huang⁹², X. Huang^{13c}, Y. Huang^{58a}, Y. Huang^{13a}, Z. Hubacek¹³⁷, F. Hubaut⁹⁸, M. Huebner²², F. Huegging²², T. B. Huffman¹³⁰, M. Huhtinen³⁴, S. K. Huiberts¹⁵, R. Hulsken⁵⁶, N. Huseynov^{77,z}, J. Huston¹⁰³, J. Huth⁵⁷, R. Hyneman¹⁴⁹, S. Hyrych^{26a}, G. Iacobucci⁵², G. Iakovidis²⁷, I. Ibragimov¹⁴⁷, L. Iconomidou-Fayard⁶², P. Iengo³⁴, R. Iguchi¹⁵⁹, T. Iizawa⁵², Y. Ikegami⁷⁹, A. Ilg¹⁸, N. Ilic¹⁶², H. Imam^{33a}, T. Ingebretsen Carlson^{43a,43b}, G. Introzzi^{68a,68b}, M. Iodice^{72a}, V. Ippolito^{70a,70b}, M. Ishino¹⁵⁹, W. Islam¹⁷⁶, C. Issever^{17,44}, S. Istin^{11c,am}, J. M. Iturbe Ponce^{60a}, R. Iuppa^{73a,73b}, A. Ivina¹⁷⁵, J. M. Izen⁴¹, V. Izzo^{67a}, P. Jacka¹³⁶, P. Jackson¹, R. M. Jacobs⁴⁴, B. P. Jaeger¹⁴⁸, C. S. Jagfeld¹¹⁰, G. Jäkel¹⁷⁷, K. Jakobs⁵⁰, T. Jakoubek¹⁷⁵, J. Jamieson⁵⁵, K. W. Janas^{81a}, G. Jarlskog⁹⁴, A. E. Jaspán⁸⁸, N. Javadov^{77,z}, T. Javůrek³⁴, M. Javurkova⁹⁹, F. Jeanneau¹⁴⁰, L. Jeanty¹²⁷, J. Jejelava^{155a,aa}, P. Jenni^{50,e}, S. Jézéquel⁴, J. Jia¹⁵¹, Z. Jia^{13c}, Y. Jiang^{58a}, S. Jiggins⁴⁸, J. Jimenez Pena¹¹¹, S. Jin^{13c}, A. Jinaru^{25b}, O. Jinnouchi¹⁶⁰, H. Jivan^{31f}, P. Johansson¹⁴⁵, K. A. Johns⁶, C. A. Johnson⁶³, D. M. Jones³⁰, E. Jones¹⁷³, R. W. L. Jones⁸⁷, T. J. Jones⁸⁸, J. Jovicevic¹⁴, X. Ju¹⁶, J. J. Junggeburth³⁴, A. Juste Rozas^{12,v}, S. Kabana^{142d}, A. Kaczmarska⁸², M. Kado^{70a,70b}, H. Kagan¹²³, M. Kagan¹⁴⁹, A. Kahn³⁷, A. Kahn¹³², C. Kahra⁹⁶, T. Kaji¹⁷⁴, E. Kajomovitz¹⁵⁶, C. W. Kalderon²⁷, A. Kamenshchikov¹¹⁸, M. Kaneda¹⁵⁹, N. J. Kang¹⁴¹, S. Kang⁷⁶, Y. Kano¹¹², D. Kar^{31f}, K. Karava¹³⁰, M. J. Kareem^{163b}, I. Karkanas¹⁵⁸, S. N. Karpov⁷⁷, Z. M. Karpova⁷⁷, V. Kartvelishvili⁸⁷, A. N. Karyukhin¹¹⁸, E. Kasimi¹⁵⁸, C. Kato^{58d}, J. Katzy⁴⁴, K. Kawade¹⁴⁶, K. Kawagoe⁸⁵, T. Kawaguchi¹¹², T. Kawamoto¹⁴⁰, G. Kawamura⁵¹, E. F. Kay¹⁷¹, F. I. Kaya¹⁶⁵, S. Kazakos¹², V. F. Kazanin^{117a,117b}, Y. Ke¹⁵¹, J. M. Keaveney^{31a}, R. Keeler¹⁷¹, J. S. Keller³², D. Kelsey¹⁵², J. J. Kempster¹⁹, J. Kendrick¹⁹, K. E. Kennedy³⁷, O. Kepka¹³⁶, S. Kersten¹⁷⁷, B. P. Kerševan⁸⁹, S. Ketabchi Haghighat¹⁶², M. Khandoga¹³¹, A. Khanov¹²⁵, A. G. Kharlamov^{117a,117b}, T. Kharlamova^{117a,117b}, E. E. Khoda¹⁴⁴, T. J. Khoo¹⁷, G. Khorauli¹⁷², E. Khravov⁷⁷, J. Khubua^{155b}, S. Kido⁸⁰, M. Kiehn³⁴, A. Kilgallon¹²⁷, E. Kim¹⁶⁰, Y. K. Kim³⁵, N. Kimura⁹², A. Kirchhoff⁵¹, D. Kirchmeier⁴⁶, C. Kirfel²², J. Kirk¹³⁹, A. E. Kiryunin¹¹¹, T. Kishimoto¹⁵⁹, D. P. Kisluk¹⁶², C. Kitsaki⁹, O. Kivernyk²², T. Klapdor-Kleingrothaus⁵⁰, M. Klassen^{59a}, C. Klein³², L. Klein¹⁷², M. H. Klein¹⁰², M. Klein⁸⁸, U. Klein⁸⁸, P. Klimek³⁴, A. Klimentov²⁷, F. Klimpel¹¹¹, T. Klingl²², T. Klioutchnikova³⁴, F. F. Klitzner¹¹⁰, P. Kluit¹¹⁵, S. Kluth¹¹¹, E. Kneringer⁷⁴, T. M. Knight¹⁶², A. Knue⁵⁰, D. Kobayashi⁸⁵, R. Kobayashi⁸³, M. Kobel⁴⁶, M. Kocian¹⁴⁹, T. Kodama¹⁵⁹, P. Kodys¹³⁸, D. M. Koeck¹⁵², P. T. Koenig²², T. Koffas³², N. M. Köhler³⁴, M. Kolb¹⁴⁰, I. Koletsou⁴, T. Komarek¹²⁶, K. Köneke⁵⁰, A. X. Y. Kong¹, T. Kono¹²², V. Konstantinides⁹², N. Konstantinidis⁹², B. Konya⁹⁴, R. Kopeliansky⁶³, S. Koperny^{81a}, K. Korcyl⁸², K. Kordas¹⁵⁸, G. Koren¹⁵⁷, A. Korn⁹², S. Korn⁵¹, I. Korolkov¹², E. V. Korolkova¹⁴⁵, N. Korotkova¹⁰⁹, B. Kortman¹¹⁵, O. Kortner¹¹¹, S. Kortner¹¹¹, W. H. Kostecka¹¹⁶, V. V. Kostyukhin^{147,161}, A. Kotsokechagia⁶², A. Kotwal⁴⁷, A. Koulouris³⁴, A. Kourkoumeli-Charalampidi^{68a,68b}, C. Kourkoumelis⁸

M. Mentink³⁴, E. Meoni^{39a,39b}, C. Merlassino¹³⁰, P. Mermod^{52,*}, L. Merola^{67a,67b}, C. Meroni^{66a}, G. Merz¹⁰², O. Meshkov^{107,109}, J. K. R. Meshreki¹⁴⁷, J. Metcalfe⁵, A. S. Mete⁵, C. Meyer⁶³, J.-P. Meyer¹⁴⁰, M. Michetti¹⁷, R. P. Middleton¹³⁹, L. Mijović⁴⁸, G. Mikenberg¹⁷⁵, M. Mikestikova¹³⁶, M. Mikuz⁸⁹, H. Mildner¹⁴⁵, A. Milic¹⁶², C. D. Milke⁴⁰, D. W. Miller³⁵, L. S. Miller³², A. Milov¹⁷⁵, D. A. Milstead^{43a,43b}, T. Min^{13c}, A. A. Minaenko¹¹⁸, I. A. Minashvili^{155b}, L. Mince⁵⁵, A. I. Mincer¹²¹, B. Mindur^{81a}, M. Mineev⁷⁷, Y. Minegishi¹⁵⁹, Y. Mino⁸³, L. M. Mir¹², M. Miralles Lopez¹⁶⁹, M. Mironova¹³⁰, T. Mitani¹⁷⁴, V. A. Mitsou¹⁶⁹, M. Mittal^{58c}, O. Miu¹⁶², P. S. Miyagawa⁹⁰, Y. Miyazaki⁸⁵, A. Mizukami⁷⁹, J. U. Mjörnmark⁹⁴, T. Mkrtychyan^{59a}, M. Mlynarikova¹¹⁶, T. Moa^{43a,43b}, S. Mobius⁵¹, K. Mochizuki¹⁰⁶, P. Moder⁴⁴, P. Mogg¹¹⁰, A. F. Mohammed^{13a}, S. Mohapatra³⁷, G. Mokgatitswane^{31f}, B. Mondal¹⁴⁷, S. Mondal¹³⁷, K. Mönig⁴⁴, E. Monnier⁹⁸, L. Monsonis Romero¹⁶⁹, A. Montalbano¹⁴⁸, J. Montejo Berlingen³⁴, M. Montella¹²³, F. Monticelli⁸⁶, N. Morange⁶², A. L. Moreira De Carvalho^{135a}, M. Moreno Llácer¹⁶⁹, C. Moreno Martinez¹², P. Moretti^{53b}, S. Morgenstern¹⁷³, D. Mori¹⁴⁸, M. Morii⁵⁷, M. Morinaga¹⁵⁹, V. Morisbak¹²⁹, A. K. Morley³⁴, A. P. Morris⁹², L. Morvaj³⁴, P. Moschovakos³⁴, B. Moser¹¹⁵, M. Mosidze^{155b}, T. Moskalets⁵⁰, P. Moskvitina¹¹⁴, J. Moss^{29,n}, E. J. W. Moyse⁹⁹, S. Muanza⁹⁸, J. Mueller¹³⁴, R. Mueller¹⁸, D. Muenstermann⁸⁷, G. A. Mullier⁹⁴, J. J. Mullin¹³², D. P. Mungo^{66a,66b}, J. L. Munoz Martinez¹², F. J. Munoz Sanchez⁹⁷, M. Murin⁹⁷, P. Murin^{26b}, W. J. Murray^{139,173}, A. Murrone^{66a,66b}, J. M. Muse¹²⁴, M. Muškinja¹⁶, C. Mwewa²⁷, A. G. Myagkov^{118,ac}, A. J. Myers⁷, A. A. Myers¹³⁴, G. Myers⁶³, M. Myska¹³⁷, B. P. Nachman¹⁶, O. Nackenhorst⁴⁵, A. Nag Nag⁴⁶, K. Nagai¹³⁰, K. Nagano⁷⁹, J. L. Nagle²⁷, E. Nagy⁹⁸, A. M. Nairz³⁴, Y. Nakahama¹¹², K. Nakamura⁷⁹, H. Nanjo¹²⁸, F. Napolitano^{59a}, R. Narayan⁴⁰, E. A. Narayanan¹¹³, I. Naryshkin¹³³, M. Naseri³², C. Nass²², T. Naumann⁴⁴, G. Navarro^{20a}, J. Navarro-Gonzalez¹⁶⁹, R. Nayak¹⁵⁷, P. Y. Nechaeva¹⁰⁷, F. Nechansky⁴⁴, T. J. Neep¹⁹, A. Negri^{68a,68b}, M. Negrini^{21b}, C. Nellist¹¹⁴, C. Nelson¹⁰⁰, K. Nelson¹⁰², S. Nemecek¹³⁶, M. Nessi^{34,f}, M. S. Neubauer¹⁶⁸, F. Neuhaus⁹⁶, J. Neundorff⁴⁴, R. Newhouse¹⁷⁰, P. R. Newman¹⁹, C. W. Ng¹³⁴, Y. S. Ng¹⁷, Y. W. Y. Ng¹⁶⁶, B. Ngair^{33c}, H. D. N. Nguyen¹⁰⁶, R. B. Nickerson¹³⁰, R. Nicolaidou¹⁴⁰, D. S. Nielsen³⁸, J. Nielsen¹⁴¹, M. Niemeyer⁵¹, N. Nikiforou¹⁰, V. Nikolaenko^{118,ae}, I. Nikolic-Audit¹³¹, K. Nikolopoulos¹⁹, P. Nilsson²⁷, H. R. Nindhito⁵², A. Nisati^{70a}, N. Nishu², R. Nisius¹¹¹, T. Nitta¹⁷⁴, T. Nobe¹⁵⁹, D. L. Noel³⁰, Y. Noguchi⁸³, I. Nomidis¹³¹, M. A. Nomura²⁷, M. B. Norfolk¹⁴⁵, R. R. B. Norisam⁹², J. Novak⁸⁹, T. Novak⁴⁴, O. Novgorodova⁴⁶, L. Novotny¹³⁷, R. Novotny¹¹³, L. Nozka¹²⁶, K. Ntekas¹⁶⁶, E. Nurse⁹², F. G. Oakham^{32,aj}, J. Ocariz¹³¹, A. Ochi⁸⁰, I. Ochoa^{135a}, J. P. Ochoa-Ricoux^{142a}, S. Oda⁸⁵, S. Odaka⁷⁹, S. Oerdek¹⁶⁷, A. Ogrodnik^{81a}, A. Oh⁹⁷, C. C. Ohm¹⁵⁰, H. Oide¹⁶⁰, R. Oishi¹⁵⁹, M. L. Ojeda⁴⁴, Y. Okazaki⁸³, M. W. O'Keefe⁸⁸, Y. Okumura¹⁵⁹, A. Olariu^{25b}, L. F. Oleiro Seabra^{135a}, S. A. Olivares Pino^{142d}, D. Oliveira Damazio²⁷, D. Oliveira Goncalves^{78a}, J. L. Oliver¹⁶⁶, M. J. R. Olsson¹⁶⁶, A. Olszewski⁸², J. Olszowska⁸², Ö. O. Öncel²², D. C. O'Neil¹⁴⁸, A. P. O'Neill¹³⁰, A. Onofre^{135a,135e}, P. U. E. Onyisi¹⁰, R. G. Oreamuno Madriz¹¹⁶, M. J. Oreglia³⁵, G. E. Orellana⁸⁶, D. Orestano^{72a,72b}, N. Orlando¹², R. S. Orr¹⁶², V. O'Shea⁵⁵, R. Ospanov^{58a}, G. Otero y Garzon²⁸, H. Otono⁸⁵, P. S. Ott^{59a}, G. J. Ottino¹⁶, M. Ouchrif^{33d}, J. Ouellette²⁷, F. Ould-Saada¹²⁹, A. Ouraou^{140,*}, Q. Ouyang^{13a}, M. Owen⁵⁵, R. E. Owen¹³⁹, K. Y. Oyulmaz^{11c}, V. E. Ozcan^{11c}, N. Ozturk⁷, S. Ozturk^{11c}, J. Pacalt¹²⁶, H. A. Pacey³⁰, K. Pachal⁴⁷, A. Pacheco Pages¹², C. Padilla Aranda¹², S. Pagan Griso¹⁶, G. Palacino⁶³, S. Palazzo⁴⁸, S. Palestini³⁴, M. Palka^{81b}, P. Palmi^{81a}, D. K. Panchal¹⁰, C. E. Pandini⁵², J. G. Panduro Vazquez⁹¹, P. Pani⁴⁴, G. Panizzo^{64a,64c}, L. Paolozzi⁵², C. Papadatos¹⁰⁶, S. Parajuli⁴⁰, A. Paramonov⁵, C. Paraskevopoulos⁹, D. Paredes Hernandez^{60b}, S. R. Paredes Saenz¹³⁰, B. Parida¹⁷⁵, T. H. Park¹⁶², A. J. Parker²⁹, M. A. Parker³⁰, F. Parodi^{53a,53b}, E. W. Parrish¹¹⁶, J. A. Parsons³⁷, U. Parzefall⁵⁰, L. Pascual Dominguez¹⁵⁷, V. R. Pascuzzi¹⁶, F. Pasquali¹¹⁵, E. Pasqualucci^{70a}, S. Passaggio^{53b}, F. Pastore⁹¹, P. Pasuwan^{43a,43b}, J. R. Pater⁹⁷, A. Pathak¹⁷⁶, J. Patton⁸⁸, T. Pauly³⁴, J. Pearkes¹⁴⁹, M. Pedersen¹²⁹, L. Pedraza Diaz¹¹⁴, R. Pedro^{135a}, T. Peiffer⁵¹, S. V. Peleganchuk^{117a,117b}, O. Penc¹³⁶, C. Peng^{60b}, H. Peng^{58a}, M. Penzin¹⁶¹, B. S. Peralva^{78a}, A. P. Pereira Peixoto^{135a}, L. Pereira Sanchez^{43a,43b}, D. V. Perepelitsa²⁷, E. Perez Codina^{163a}, M. Perganti⁹, L. Perini^{66a,66b}, H. Pernegger³⁴, S. Perrella³⁴, A. Perrevoort¹¹⁵, K. Peters⁴⁴, R. F. Y. Peters⁹⁷, B. A. Petersen³⁴, T. C. Petersen³⁸, E. Petit⁹⁸, V. Petousis¹³⁷, C. Petridou¹⁵⁸, P. Petroff⁶², F. Petrucci^{72a,72b}, A. Petrukhin¹⁴⁷, M. Pettee¹⁷⁸, N. E. Pettersson³⁴, K. Petukhova¹³⁸, A. Peyaud¹⁴⁰, R. Pezoa^{142e}, L. Pezzotti³⁴, G. Pezzullo¹⁷⁸, T. Pham¹⁰¹, P. W. Phillips¹³⁹, M. W. Phipps¹⁶⁸, G. Piacquadio¹⁵¹, E. Pianori¹⁶, F. Piazza^{66a,66b}, A. Picazio⁹⁹, R. Piegaia²⁸, D. Pietreanu^{25b}, J. E. Pilcher³⁵, A. D. Pilkington⁹⁷, M. Pinamonti^{64a,64c}, J. L. Pinfold², C. Pitman Donaldson⁹², D. A. Pizzi³², L. Pizzimento^{71a,71b}, A. Pizzini¹¹⁵, M.-A. Pleier²⁷, V. Plesanov⁵⁰, V. Pleskot¹³⁸, E. Plotnikova⁷⁷, P. Podberezko^{117a,117b}

R. Poettgen⁹⁴, R. Poggi⁵², L. Poggioni¹³¹, I. Pogrebnyak¹⁰³, D. Pohl²², I. Pokharel⁵¹, G. Polesello^{68a}, A. Poley^{148,163a}, A. Policicchio^{70a,70b}, R. Polifka¹³⁸, A. Polini^{21b}, C. S. Pollard¹³⁰, Z. B. Pollock¹²³, V. Polychronakos²⁷, D. Ponomarenko¹⁰⁸, L. Pontecorvo³⁴, S. Popa^{25a}, G. A. Popeneci^{25d}, L. Portales⁴, D. M. Portillo Quintero^{163a}, S. Pospisil¹³⁷, P. Postolache^{25c}, K. Potamianos¹³⁰, I. N. Potrap⁷⁷, C. J. Potter³⁰, H. Potti¹, T. Poulsen⁴⁴, J. Poveda¹⁶⁹, T. D. Powell¹⁴⁵, G. Pownall⁴⁴, M. E. Pozo Astigarraga³⁴, A. Prades Ibanez¹⁶⁹, P. Pralavorio⁹⁸, M. M. Prapa⁴², S. Prell⁷⁶, D. Price⁹⁷, M. Primavera^{65a}, M. A. Principe Martin⁹⁵, M. L. Proffitt¹⁴⁴, N. Proklova¹⁰⁸, K. Prokofiev^{60c}, F. Prokoshin⁷⁷, S. Protopopescu²⁷, J. Proudfoot⁵, M. Przybycien^{81a}, D. Pudzha¹³³, P. Puzo⁶², D. Pyatizbyantseva¹⁰⁸, J. Qian¹⁰², Y. Qin⁹⁷, T. Qiu⁹⁰, A. Quadt⁵¹, M. Queitsch-Maitland³⁴, G. Rabanal Bolanos⁵⁷, F. Ragusa^{66a,66b}, J. A. Raine⁵², S. Rajagopalan²⁷, K. Ran^{13a,13d}, D. F. Rassloff^{59a}, D. M. Rauch⁴⁴, S. Rave⁹⁶, B. Ravina⁵⁵, I. Ravinovich¹⁷⁵, M. Raymond³⁴, A. L. Read¹²⁹, N. P. Readioff¹⁴⁵, D. M. Rebutzi^{68a,68b}, G. Redlinger²⁷, K. Reeves⁴¹, D. Reikher¹⁵⁷, A. Reiss⁹⁶, A. Rej¹⁴⁷, C. Rembser³⁴, A. Renardi⁴⁴, M. Renda^{25b}, M. B. Rendel¹¹¹, A. G. Rennie⁵⁵, S. Resconi^{66a}, M. Ressegotti^{53a,53b}, E. D. Resseguie¹⁶, S. Rettie⁹², B. Reynolds¹²³, E. Reynolds¹⁹, M. Rezaei Estabragh¹⁷⁷, O. L. Rezanova^{117a,117b}, P. Reznicek¹³⁸, E. Ricci^{73a,73b}, R. Richter¹¹¹, S. Richter⁴⁴, E. Richter-Was^{81b}, M. Ridel¹³¹, P. Rieck¹¹¹, P. Riedler³⁴, O. Rifki⁴⁴, M. Rijssenbeek¹⁵¹, A. Rimoldi^{68a,68b}, M. Rimoldi⁴⁴, L. Rinaldi^{21a,21b}, T. T. Rinn¹⁶⁸, M. P. Rinnagel¹¹⁰, G. Ripellino¹⁵⁰, I. Riu¹², P. Rivadeneira⁴⁴, J. C. Rivera Vergara¹⁷¹, F. Rizatdinova¹²⁵, E. Rizvi⁹⁰, C. Rizzi⁵², B. A. Roberts¹⁷³, B. R. Roberts¹⁶, S. H. Robertson^{100,y}, M. Robin⁴⁴, D. Robinson³⁰, C. M. Robles Gajardo^{142c}, M. Robles Manzano⁹⁶, A. Robson⁵⁵, A. Rocchi^{71a,71b}, C. Roda^{69a,69b}, S. Rodriguez Bosca^{59a}, A. Rodriguez Rodriguez⁵⁰, A. M. Rodríguez Vera^{163b}, S. Roe³⁴, A. R. Roepe¹²⁴, J. Roggel¹⁷⁷, O. Røhne¹²⁹, R. A. Rojas¹⁷¹, B. Roland⁵⁰, C. P. A. Roland⁶³, J. Roloff²⁷, A. Romaniouk¹⁰⁸, M. Romano^{21b}, A. C. Romero Hernandez¹⁶⁸, N. Rompotis⁸⁸, M. Ronzani¹²¹, L. Roos¹³¹, S. Rosati^{70a}, B. J. Rosser¹³², E. Rossi¹⁶², E. Rossi⁴, E. Rossi^{67a,67b}, L. P. Rossi^{53b}, L. Rossini⁴⁴, R. Rosten¹²³, M. Rotaru^{25b}, B. Rottler⁵⁰, D. Rousseau⁶², D. Rouso³⁰, G. Rovelli^{68a,68b}, A. Roy¹⁰, A. Rozanov⁹⁸, Y. Rozen¹⁵⁶, X. Ruan^{31f}, A. J. Ruby⁸⁸, T. A. Ruggeri¹, F. Rühr⁵⁰, A. Ruiz-Martinez¹⁶⁹, A. Rummeler³⁴, Z. Rurikova⁵⁰, N. A. Rusakovich⁷⁷, H. L. Russell³⁴, L. Rustige³⁶, J. P. Rutherford⁶, E. M. Rüttinger¹⁴⁵, M. Rybar¹³⁸, E. B. Rye¹²⁹, A. Ryzhov¹¹⁸, J. A. Sabater Iglesias⁴⁴, P. Sabatini¹⁶⁹, L. Sabetta^{70a,70b}, H. F.-W. Sadrozinski¹⁴¹, R. Sadykov⁷⁷, F. Safai Tehrani^{70a}, B. Safarzadeh Samani¹⁵², M. Safdari¹⁴⁹, S. Saha¹⁰⁰, M. Sahinsoy¹¹¹, A. Sahu¹⁷⁷, M. Saimpert¹⁴⁰, M. Saito¹⁵⁹, T. Saito¹⁵⁹, D. Salamani³⁴, G. Salamanna^{72a,72b}, A. Salnikov¹⁴⁹, J. Salt¹⁶⁹, A. Salvador Salas¹², D. Salvatore^{39a,39b}, F. Salvatore¹⁵², A. Salzburger³⁴, D. Sammel⁵⁰, D. Sampsonidis¹⁵⁸, D. Sampsonidou^{58c,58d}, J. Sánchez¹⁶⁹, A. Sanchez Pineda⁴, V. Sanchez Sebastian¹⁶⁹, H. Sandaker¹²⁹, C. O. Sander⁴⁴, I. G. Sanderswood⁸⁷, J. A. Sandesara⁹⁹, M. Sandhoff¹⁷⁷, C. Sandoval^{20b}, D. P. C. Sankey¹³⁹, M. Sannino^{53a,53b}, A. Sansoni⁴⁹, C. Santoni³⁶, H. Santos^{135a,135b}, S. N. Santpur¹⁶, A. Santra¹⁷⁵, K. A. Saoucha¹⁴⁵, A. Saponov⁷⁷, J. G. Saraiva^{135a,135d}, J. Sardain⁹⁸, O. Sasaki⁷⁹, K. Sato¹⁶⁴, C. Sauer^{59b}, F. Sauerburger⁵⁰, E. Sauvan⁴, P. Savard^{162,aj}, R. Sawada¹⁵⁹, C. Sawyer¹³⁹, L. Sawyer⁹³, I. Sayago Galvan¹⁶⁹, C. Sbarra^{21b}, A. Sbrizzi^{21a,21b}, T. Scanlon⁹², J. Schaarschmidt¹⁴⁴, P. Schacht¹¹¹, D. Schaefer³⁵, U. Schäfer⁹⁶, A. C. Schaffer⁶², D. Schaile¹¹⁰, R. D. Schamberger¹⁵¹, E. Schanet¹¹⁰, C. Scharf¹⁷, N. Scharmberg⁹⁷, V. A. Schegelsky¹³³, D. Scheirich¹³⁸, F. Schenck¹⁷, M. Schernau¹⁶⁶, C. Schiavi^{53a,53b}, L. K. Schildgen²², Z. M. Schillaci²⁴, E. J. Schioppa^{65a,65b}, M. Schioppa^{39a,39b}, B. Schlag⁹⁶, K. E. Schleicher⁵⁰, S. Schlenker³⁴, K. Schmieden⁹⁶, C. Schmitt⁹⁶, S. Schmitt⁴⁴, L. Schoeffel¹⁴⁰, A. Schoening^{59b}, P. G. Scholer⁵⁰, E. Schopf¹³⁰, M. Schott⁹⁶, J. Schovancova³⁴, S. Schramm⁵², F. Schroeder¹⁷⁷, H.-C. Schultz-Coulon^{59a}, M. Schumacher⁵⁰, B. A. Schumm¹⁴¹, Ph. Schune¹⁴⁰, A. Schwartzman¹⁴⁹, T. A. Schwarz¹⁰², Ph. Schwemling¹⁴⁰, R. Schwienhorst¹⁰³, A. Sciandra¹⁴¹, G. Sciolla²⁴, F. Scuri^{69a}, F. Scutti¹⁰¹, C. D. Sebastiani⁸⁸, K. Sedlaczek⁴⁵, P. Seema¹⁷, S. C. Seidel¹¹³, A. Seiden¹⁴¹, B. D. Seidlitz²⁷, T. Seiss³⁵, C. Seitz⁴⁴, J. M. Seixas^{78b}, G. Sekhniaidze^{67a}, S. J. Sekula⁴⁰, L. Selem⁴, N. Semprini-Cesari^{21a,21b}, S. Sen⁴⁷, C. Serfon²⁷, L. Serin⁶², L. Serkin^{64a,64b}, M. Sessa^{72a,72b}, H. Severini¹²⁴, S. Sevova¹⁴⁹, F. Sforza^{53a,53b}, A. Sfyrlla⁵², E. Shabalina⁵¹, R. Shaheen¹⁵⁰, J. D. Shahinian¹³², N. W. Shaikh^{43a,43b}, D. Shaked Renous¹⁷⁵, L. Y. Shan^{13a}, M. Shapiro¹⁶, A. Sharma³⁴, A. S. Sharma¹, S. Sharma⁴⁴, P. B. Shatalov¹¹⁹, K. Shaw¹⁵², S. M. Shaw⁹⁷, P. Sherwood⁹², L. Shi⁹², C. O. Shimmin¹⁷⁸, Y. Shimogama¹⁷⁴, J. D. Shinner⁹¹, I. P. J. Shipsey¹³⁰, S. Shirabe⁵², M. Shiyakova⁷⁷, J. Shlomi¹⁷⁵, M. J. Shochet³⁵, J. Shojaii¹⁰¹, D. R. Shope¹⁵⁰, S. Shrestha¹²³, E. M. Shrif^{31f}, M. J. Shroff¹⁷¹, E. Shulga¹⁷⁵, P. Sicho¹³⁶, A. M. Sickles¹⁶⁸, E. Sideras Haddad^{31f}, O. Sidiropoulou³⁴, A. Sidoti^{21b}, F. Siegert⁴⁶, Dj. Sijacki¹⁴, J. M. Silva¹⁹, M. V. Silva Oliveira³⁴, S. B. Silverstein^{43a}, S. Simion⁶², R. Simoniello³⁴

N. D. Simpson⁹⁴, S. Simsek^{11b}, P. Sinervo¹⁶², V. Sinetkii¹⁰⁹, S. Singh¹⁴⁸, S. Singh¹⁶², S. Sinha⁴⁴, S. Sinha^{31f}, M. Sioli^{21a,21b}, I. Siral¹²⁷, S. Yu. Sivoklov¹⁰⁹, J. Sjölin^{43a,43b}, A. Skaf⁵¹, E. Skorda⁹⁴, P. Skubic¹²⁴, M. Slawinska⁸², K. Sliwa¹⁶⁵, V. Smakhtin¹⁷⁵, B. H. Smart¹³⁹, J. Smiesko¹³⁸, S. Yu. Smirnov¹⁰⁸, Y. Smirnov¹⁰⁸, L. N. Smirnova^{109,r}, O. Smirnova⁹⁴, E. A. Smith³⁵, H. A. Smith¹³⁰, M. Smizanska⁸⁷, K. Smolek¹³⁷, A. Smykiewicz⁸², A. A. Snesarev¹⁰⁷, H. L. Snoek¹¹⁵, S. Snyder²⁷, R. Sobie^{171,y}, A. Soffer¹⁵⁷, F. Sohns⁵¹, C. A. Solans Sanchez³⁴, E. Yu. Soldatov¹⁰⁸, U. Soldevila¹⁶⁹, A. A. Solodkov¹¹⁸, S. Solomon⁵⁰, A. Soloshenko⁷⁷, O. V. Solovyanov¹¹⁸, V. Solovyev¹³³, P. Sommer¹⁴⁵, H. Son¹⁶⁵, A. Sonay¹², W. Y. Song^{163b}, A. Sopczak¹³⁷, A. L. Soppio⁹², F. Sopkova^{26b}, S. Sottocornola^{68a,68b}, R. Soualah^{64a,64c}, A. M. Soukharev^{117a,117b}, Z. Soumami^{33e}, D. South⁴⁴, S. Spagnolo^{65a,65b}, M. Spalla¹¹¹, M. Spangenberg¹⁷³, F. Spanò⁹¹, D. Sperlich⁵⁰, T. M. Spieker^{59a}, G. Spigo³⁴, M. Spina¹⁵², D. P. Spiteri⁵⁵, M. Spousta¹³⁸, A. Stabile^{66a,66b}, R. Stamen^{59a}, M. Stamenkovic¹¹⁵, A. Stampekis¹⁹, M. Standke²², E. Stanecka⁸², B. Stanislaus³⁴, M. M. Stanitzki⁴⁴, M. Stankaityte¹³⁰, B. Stapf⁴⁴, E. A. Starchenko¹¹⁸, G. H. Stark¹⁴¹, J. Stark⁹⁸, D. M. Starke^{163b}, P. Staroba¹³⁶, P. Starovoitov^{59a}, S. Stärz¹⁰⁰, R. Staszewski⁸², G. Stavropoulos⁴², P. Steinberg²⁷, A. L. Steinhebel¹²⁷, B. Stelzer^{148,163a}, H. J. Stelzer¹³⁴, O. Stelzer-Chilton^{163a}, H. Stenzel⁵⁴, T. J. Stevenson¹⁵², G. A. Stewart³⁴, M. C. Stockton³⁴, G. Stoica^{25b}, M. Stolarski^{135a}, S. Stonjek¹¹¹, A. Straessner⁴⁶, J. Strandberg¹⁵⁰, S. Strandberg^{43a,43b}, M. Strauss¹²⁴, T. Streble⁹⁸, P. Strizenc^{26b}, R. Ströhmer¹⁷², D. M. Strom¹²⁷, L. R. Strom⁴⁴, R. Stroynowski⁴⁰, A. Strubig^{43a,43b}, S. A. Stucci²⁷, B. Stugu¹⁵, J. Stupak¹²⁴, N. A. Styles⁴⁴, D. Su¹⁴⁹, S. Su^{58a}, W. Su^{58c,58d,144}, X. Su^{58a}, K. Sugizaki¹⁵⁹, V. V. Sulin¹⁰⁷, M. J. Sullivan⁸⁸, D. M. S. Sultan⁵², L. Sultanaliyeva¹⁰⁷, S. Sultansoy^{3c}, T. Sumida⁸³, S. Sun¹⁰², S. Sun¹⁷⁶, X. Sun⁹⁷, O. Sunneborn Gudnadottir¹⁶⁷, C. J. E. Suster¹⁵³, M. R. Sutton¹⁵², M. Svatos¹³⁶, M. Swiatlowski^{163a}, T. Swirski¹⁷², I. Sykora^{26a}, M. Sykora¹³⁸, T. Sykora¹³⁸, D. Ta⁹⁶, K. Tackmann^{44,w}, A. Taffard¹⁶⁶, R. Tafirout^{163a}, R. H. M. Taibah¹³¹, R. Takashima⁸⁴, K. Takeda⁸⁰, T. Takeshita¹⁴⁶, E. P. Takeva⁴⁸, Y. Takubo⁷⁹, M. Talby⁹⁸, A. A. Talyshev^{117a,117b}, K. C. Tam^{60b}, N. M. Tamir¹⁵⁷, A. Tanaka¹⁵⁹, J. Tanaka¹⁵⁹, R. Tanaka⁶², J. Tang^{58c}, Z. Tao¹⁷⁰, S. Tapia Araya⁷⁶, S. Tapprogge⁹⁶, A. Tarek Abouelfadl Mohamed¹⁰³, S. Tarem¹⁵⁶, K. Tariq^{58b}, G. Tarna^{25b}, G. F. Tartarelli^{66a}, P. Tas¹³⁸, M. Tasevsky¹³⁶, E. Tassi^{39a,39b}, G. Tateno¹⁵⁹, Y. Tayalati^{33e}, G. N. Taylor¹⁰¹, W. Taylor^{163b}, H. Teagle⁸⁸, A. S. Tee¹⁷⁶, R. Teixeira De Lima¹⁴⁹, P. Teixeira-Dias⁹¹, H. Ten Kate³⁴, J. J. Teoh¹¹⁵, K. Terashi¹⁵⁹, J. Terron⁹⁵, S. Terzo¹², M. Testa⁴⁹, R. J. Teuscher^{162,y}, N. Themistokleous⁴⁸, T. Thevenaux-Pelzer¹⁷, O. Thielmann¹⁷⁷, D. W. Thomas⁹¹, J. P. Thomas¹⁹, E. A. Thompson⁴⁴, P. D. Thompson¹⁹, E. Thomson¹³², E. J. Thorpe⁹⁰, Y. Tian⁵¹, V. O. Tikhomirov^{107,af}, Yu. A. Tikhonov^{117a,117b}, S. Timoshenko¹⁰⁸, P. Tipton¹⁷⁸, S. Tisserant⁹⁸, S. H. Tlou^{31f}, A. Tmourji³⁶, K. Todome^{21a,21b}, S. Todorova-Nova¹³⁸, S. Todt⁴⁶, M. Togawa⁷⁹, J. Tojo⁸⁵, S. Tokár^{26a}, K. Tokushuku⁷⁹, E. Tolley¹²³, R. Tombs³⁰, M. Tomoto^{79,112}, L. Tompkins¹⁴⁹, P. Tornambe⁹⁹, E. Torrence¹²⁷, H. Torres⁴⁶, E. Torró Pastor¹⁶⁹, M. Toscani²⁸, C. Toscirri³⁵, J. Toth^{98,x}, D. R. Tovey¹⁴⁵, A. Traet¹⁵, C. J. Treado¹²¹, T. Trefzger¹⁷², A. Tricoli²⁷, I. M. Trigger^{163a}, S. Trincz-Duvold¹³¹, D. A. Trischuk¹⁷⁰, W. Trischuk¹⁶², B. Trocme⁵⁶, A. Trofymov⁶², C. Troncon^{66a}, F. Trovato¹⁵², L. Truong^{31c}, M. Trzebinski⁸², A. Trzupek⁸², F. Tsai¹⁵¹, A. Tsiamis¹⁵⁸, P. V. Tsiarehka^{104,ad}, A. Tsigotis^{158,u}, V. Tsiskaridze¹⁵¹, E. G. Tskhadadze^{155a}, M. Tsopoulou¹⁵⁸, Y. Tsujikawa⁸³, I. I. Tsukerman¹¹⁹, V. Tsulaia¹⁶, S. Tsuno⁷⁹, O. Tsur¹⁵⁶, D. Tsybychev¹⁵¹, Y. Tu^{60b}, A. Tudorache^{25b}, V. Tudorache^{25b}, A. N. Tuna³⁴, S. Turchikhin⁷⁷, I. Turk Cakir^{3a}, R. J. Turner¹⁹, R. Turra^{66a}, P. M. Tuts³⁷, S. Tzamarias¹⁵⁸, P. Tzani⁹, E. Tzovara⁹⁶, K. Uchida¹⁵⁹, F. Ukegawa¹⁶⁴, P. A. Ulloa Poblete^{142c}, G. Unal³⁴, M. Unal¹⁰, A. Undrus²⁷, G. Unel¹⁶⁶, F. C. Ungaro¹⁰¹, K. Uno¹⁵⁹, J. Urban^{26b}, P. Urquijo¹⁰¹, G. Usai⁷, R. Ushioda¹⁶⁰, M. Usman¹⁰⁶, Z. Uysal^{11d}, V. Vacek¹³⁷, B. Vachon¹⁰⁰, K. O. H. Vadla¹²⁹, T. Vafeiadis³⁴, C. Valderanis¹¹⁰, E. Valdes Santurio^{43a,43b}, M. Valente^{163a}, S. Valentini^{21a,21b}, A. Valero¹⁶⁹, R. A. Vallance¹⁹, A. Vallier⁹⁸, J. A. Valls Ferrer¹⁶⁹, T. R. Van Daalen¹⁴⁴, P. Van Gemmeren⁵, S. Van Stroud⁹², I. Van Vulpen¹¹⁵, M. Vanadia^{71a,71b}, W. Vandelli³⁴, M. Vandenbroucke¹⁴⁰, E. R. Vandewall¹²⁵, D. Vannicola¹⁵⁷, L. Vannoli^{53a,53b}, R. Vari^{70a}, E. W. Varnes⁶, C. Varni¹⁶, T. Varol¹⁵⁴, D. Varouchas⁶², K. E. Varvell¹⁵³, M. E. Vasile^{25b}, L. Vaslin³⁶, G. A. Vasquez¹⁷¹, F. Vazeille³⁶, D. Vazquez Furelos¹², T. Vazquez Schroeder³⁴, J. Veatch⁵¹, V. Vecchio⁹⁷, M. J. Veen¹¹⁵, I. Veliscek¹³⁰, L. M. Veloce¹⁶², F. Veloso^{135a,135c}, S. Veneziano^{70a}, A. Ventura^{65a,65b}, A. Verbytskyi¹¹¹, M. Verducci^{69a,69b}, C. Vergis²², M. Verissimo De Araujo^{78b}, W. Verkerke¹¹⁵, A. T. Vermeulen¹¹⁵, J. C. Vermeulen¹¹⁵, C. Vernieri¹⁴⁹, P. J. Verschuur⁹¹, M. Vessella⁹⁹, M. L. Vesterbacka¹²¹, M. C. Vetterli^{148,aj}, A. Vgenopoulos¹⁵⁸, N. Viaux Maira^{142e}, T. Vickey¹⁴⁵, O. E. Vickey Boeriu¹⁴⁵, G. H. A. Viehhauser¹³⁰, L. Vigani^{59b}, M. Villa^{21a,21b}, M. Villaplana Perez¹⁶⁹, E. M. Villhauer⁴⁸, E. Vilucchi⁴⁹, M. G. Vincker³², G. S. Virdee¹⁹, A. Vishwakarma⁴⁸, C. Vittori^{21a,21b}

I. Vivarelli¹⁵², V. Vladimirov¹⁷³, E. Voevodina¹¹¹, M. Vogel¹⁷⁷, P. Vokac¹³⁷, J. Von Ahnen⁴⁴, E. Von Toerne²², V. Vorobel¹³⁸, K. Vorobev¹⁰⁸, M. Vos¹⁶⁹, J. H. Vosseveld⁸⁸, M. Vozak⁹⁷, L. Vozdecky⁹⁰, N. Vranjes¹⁴, M. Vranjes Milosavljevic¹⁴, V. Vrba^{137,*}, M. Vreeswijk¹¹⁵, N. K. Vu⁹⁸, R. Vuillermet³⁴, O. V. Vujinovic⁹⁶, I. Vukotic³⁵, S. Wada¹⁶⁴, C. Wagner⁹⁹, W. Wagner¹⁷⁷, S. Wahdan¹⁷⁷, H. Wahlberg⁸⁶, R. Wakasa¹⁶⁴, M. Wakida¹¹², V. M. Walbrecht¹¹¹, J. Walder¹³⁹, R. Walker¹¹⁰, S. D. Walker⁹¹, W. Walkowiak¹⁴⁷, A. M. Wang⁵⁷, A. Z. Wang¹⁷⁶, C. Wang^{58a}, C. Wang^{58c}, H. Wang¹⁶, J. Wang^{60a}, P. Wang⁴⁰, R.-J. Wang⁹⁶, R. Wang⁵⁷, R. Wang¹¹⁶, S. M. Wang¹⁵⁴, S. Wang^{58b}, T. Wang^{58a}, W. T. Wang⁷⁵, W. X. Wang^{58a}, X. Wang^{13c}, X. Wang¹⁶⁸, X. Wang^{58c}, Y. Wang^{58a}, Z. Wang¹⁰², C. Wanotayaroj³⁴, A. Warburton¹⁰⁰, C. P. Ward³⁰, R. J. Ward¹⁹, N. Warrack⁵⁵, A. T. Watson¹⁹, M. F. Watson¹⁹, G. Watts¹⁴⁴, B. M. Waugh⁹², A. F. Webb¹⁰, C. Weber²⁷, M. S. Weber¹⁸, S. A. Weber³², S. M. Weber^{59a}, C. Wei^{58a}, Y. Wei¹³⁰, A. R. Weidberg¹³⁰, J. Weingarten⁴⁵, M. Weirich⁹⁶, C. Weiser⁵⁰, T. Wenaus²⁷, B. Wendland⁴⁵, T. Wengler³⁴, S. Wenig³⁴, N. Wermes²², M. Wessels^{59a}, K. Whalen¹²⁷, A. M. Wharton⁸⁷, A. S. White⁵⁷, A. White⁷, M. J. White¹, D. Whiteson¹⁶⁶, L. Wickremasinghe¹²⁸, W. Wiedenmann¹⁷⁶, C. Wiel⁴⁶, M. Wielers¹³⁹, N. Wieseotte⁹⁶, C. Wiglesworth³⁸, L. A. M. Wiik-Fuchs⁵⁰, D. J. Wilbern¹²⁴, H. G. Wilkens³⁴, L. J. Wilkins⁹¹, D. M. Williams³⁷, H. H. Williams¹³², S. Williams³⁰, S. Willocq⁹⁹, P. J. Windischhofer¹³⁰, I. Wingerter-Seez⁴, F. Winklmeier¹²⁷, B. T. Winter⁵⁰, M. Wittgen¹⁴⁹, M. Wobisch⁹³, A. Wolf⁹⁶, R. Wölker¹³⁰, J. Wollrath¹⁶⁶, M. W. Wolter⁸², H. Wolters^{135a,135c}, V. W. S. Wong¹⁷⁰, A. F. Wongel⁴⁴, S. D. Worm⁴⁴, B. K. Wosiek⁸², K. W. Woźniak⁸², K. Wraight⁵⁵, J. Wu^{13a,13d}, S. L. Wu¹⁷⁶, X. Wu⁵², Y. Wu^{58a}, Z. Wu^{58a,140}, J. Wuerzinger¹³⁰, T. R. Wyatt⁹⁷, B. M. Wynne⁴⁸, S. Xella³⁸, L. Xia^{13c}, M. Xia^{13b}, J. Xiang^{60c}, X. Xiao¹⁰², M. Xie^{58a}, X. Xie^{58a}, I. Xioidis¹⁵², D. Xu^{13a}, H. Xu^{58a}, H. Xu^{58a}, L. Xu^{58a}, R. Xu¹³², T. Xu^{58a}, W. Xu¹⁰², Y. Xu^{13b}, Z. Xu^{58b}, Z. Xu¹⁴⁹, B. Yabsley¹⁵³, S. Yacoob^{31a}, N. Yamaguchi⁸⁵, Y. Yamaguchi¹⁶⁰, M. Yamatani¹⁵⁹, H. Yamauchi¹⁶⁴, T. Yamazaki¹⁶, Y. Yamazaki⁸⁰, J. Yan^{58c}, S. Yan¹³⁰, Z. Yan²³, H. J. Yang^{58c,58d}, H. T. Yang¹⁶, S. Yang^{58a}, T. Yang^{60c}, X. Yang^{58a}, X. Yang^{13a}, Y. Yang¹⁵⁹, Z. Yang^{58a,102}, W.-M. Yao¹⁶, Y. C. Yap⁴⁴, H. Ye^{13c}, J. Ye⁴⁰, S. Ye²⁷, I. Yeletsikh⁷⁷, M. R. Yexley⁸⁷, P. Yin³⁷, K. Yorita¹⁷⁴, K. Yoshihara⁷⁶, C. J. S. Young⁵⁰, C. Young¹⁴⁹, M. Yuan¹⁰², R. Yuan^{58b,j}, X. Yue^{59a}, M. Zaazoua^{33e}, B. Zabinski⁸², G. Zacharis⁹, E. Zaid⁴⁸, A. M. Zaitsev^{118,ae}, T. Zakareishvili^{155b}, N. Zakharchuk³², S. Zambito³⁴, D. Zanzi⁵⁰, S. V. Zeißner⁴⁵, C. Zeitnitz¹⁷⁷, J. C. Zeng¹⁶⁸, D. T. Zenger Jr²⁴, O. Zenin¹¹⁸, T. Ženiš^{26a}, S. Zenz⁹⁰, S. Zerradi^{33a}, D. Zerwas⁶², B. Zhang^{13c}, D. F. Zhang¹⁴⁵, G. Zhang^{13b}, J. Zhang⁵, K. Zhang^{13a}, L. Zhang^{13c}, M. Zhang¹⁶⁸, R. Zhang¹⁷⁶, S. Zhang¹⁰², X. Zhang^{58c}, X. Zhang^{58b}, Z. Zhang⁶², P. Zhao⁴⁷, T. Zhao^{58b}, Y. Zhao¹⁴¹, Z. Zhao^{58a}, A. Zhemchugov⁷⁷, Z. Zheng¹⁴⁹, D. Zhong¹⁶⁸, B. Zhou¹⁰², C. Zhou¹⁷⁶, H. Zhou⁶, N. Zhou^{58c}, Y. Zhou⁶, C. G. Zhu^{58b}, C. Zhu^{13a,13d}, H. L. Zhu^{58a}, H. Zhu^{13a}, J. Zhu¹⁰², Y. Zhu^{58a}, X. Zhuang^{13a}, K. Zhukov¹⁰⁷, V. Zhulanov^{117a,117b}, D. Zieminska⁶³, N. I. Zimine⁷⁷, S. Zimmermann^{50,*}, J. Zinsser^{59b}, M. Ziolkowski¹⁴⁷, L. Živković¹⁴, A. Zoccoli^{21a,21b}, K. Zoch⁵², T. G. Zorbas¹⁴⁵, O. Zormpa⁴², W. Zou³⁷, L. Zwalinski³⁴

¹ Department of Physics, University of Adelaide, Adelaide, Australia

² Department of Physics, University of Alberta, Edmonton, AB, Canada

³ (a) Department of Physics, Ankara University, Ankara, Turkey; (b) Istanbul Aydin University, Application and Research Center for Advanced Studies, Istanbul, Turkey; (c) Division of Physics, TOBB University of Economics and Technology, Ankara, Turkey

⁴ LAPP, Univ. Savoie Mont Blanc, CNRS/IN2P3, Annecy, France

⁵ High Energy Physics Division, Argonne National Laboratory, Argonne, IL, USA

⁶ Department of Physics, University of Arizona, Tucson, AZ, USA

⁷ Department of Physics, University of Texas at Arlington, Arlington, TX, USA

⁸ Physics Department, National and Kapodistrian University of Athens, Athens, Greece

⁹ Physics Department, National Technical University of Athens, Zografou, Greece

¹⁰ Department of Physics, University of Texas at Austin, Austin, TX, USA

¹¹ (a) Bahcesehir University, Faculty of Engineering and Natural Sciences, Istanbul, Turkey; (b) Istanbul Bilgi University, Faculty of Engineering and Natural Sciences, Istanbul, Turkey; (c) Department of Physics, Bogazici University, Istanbul, Turkey; (d) Department of Physics Engineering, Gaziantep University, Gaziantep, Turkey

¹² Institut de Física d'Altes Energies (IFAE), Barcelona Institute of Science and Technology, Barcelona, Spain

- 13 (a)Institute of High Energy Physics, Chinese Academy of Sciences, Beijing, China; (b)Physics Department, Tsinghua University, Beijing, China; (c)Department of Physics, Nanjing University, Nanjing, China; (d)University of Chinese Academy of Science (UCAS), Beijing, China
- 14 Institute of Physics, University of Belgrade, Belgrade, Serbia
- 15 Department for Physics and Technology, University of Bergen, Bergen, Norway
- 16 Physics Division, Lawrence Berkeley National Laboratory and University of California, Berkeley, CA, USA
- 17 Institut für Physik, Humboldt Universität zu Berlin, Berlin, Germany
- 18 Albert Einstein Center for Fundamental Physics and Laboratory for High Energy Physics, University of Bern, Bern, Switzerland
- 19 School of Physics and Astronomy, University of Birmingham, Birmingham, UK
- 20 (a)Facultad de Ciencias y Centro de Investigaciones, Universidad Antonio Nariño, Bogotá, Colombia; (b)Departamento de Física, Universidad Nacional de Colombia, Bogotá, Colombia
- 21 (a)Dipartimento di Fisica e Astronomia A. Righi, Università di Bologna, Bologna, Italy; (b)INFN Sezione di Bologna, Bologna, Italy
- 22 Physikalisches Institut, Universität Bonn, Bonn, Germany
- 23 Department of Physics, Boston University, Boston, MA, USA
- 24 Department of Physics, Brandeis University, Waltham, MA, USA
- 25 (a)Transilvania University of Brasov, Brasov, Romania; (b)Horia Hulubei National Institute of Physics and Nuclear Engineering, Bucharest, Romania; (c)Department of Physics, Alexandru Ioan Cuza University of Iasi, Iasi, Romania; (d)National Institute for Research and Development of Isotopic and Molecular Technologies, Physics Department, Cluj-Napoca, Romania; (e)University Politehnica Bucharest, Bucharest, Romania; (f)West University in Timisoara, Timisoara, Romania
- 26 (a)Faculty of Mathematics, Physics and Informatics, Comenius University, Bratislava, Slovak Republic; (b)Department of Subnuclear Physics, Institute of Experimental Physics of the Slovak Academy of Sciences, Kosice, Slovak Republic
- 27 Physics Department, Brookhaven National Laboratory, Upton, NY, USA
- 28 Departamento de Física (FCEN) and IFIBA, Universidad de Buenos Aires and CONICET, Buenos Aires, Argentina
- 29 California State University, California, USA
- 30 Cavendish Laboratory, University of Cambridge, Cambridge, UK
- 31 (a)Department of Physics, University of Cape Town, Cape Town, South Africa; (b)iThemba Labs, Western Cape, South Africa; (c)Department of Mechanical Engineering Science, University of Johannesburg, Johannesburg, South Africa; (d)National Institute of Physics, University of the Philippines, Diliman (Philippines), Philippines; (e)University of South Africa, Department of Physics, Pretoria, South Africa; (f)School of Physics, University of the Witwatersrand, Johannesburg, South Africa
- 32 Department of Physics, Carleton University, Ottawa, ON, Canada
- 33 (a)Faculté des Sciences Ain Chock, Réseau Universitaire de Physique des Hautes Energies - Université Hassan II, Casablanca, Morocco; (b)Faculté des Sciences, Université Ibn-Tofail, Kenitra, Morocco; (c)Faculté des Sciences Semlalia, Université Cadi Ayyad, LPHEA-Marrakech, Marrakech, Morocco; (d)LPMR, Faculté des Sciences, Université Mohamed Premier, Oujda, Morocco; (e)Faculté des sciences, Université Mohammed V, Rabat, Morocco; (f)Mohammed VI Polytechnic University, Ben Guerir, Morocco
- 34 CERN, Geneva, Switzerland
- 35 Enrico Fermi Institute, University of Chicago, Chicago, IL, USA
- 36 LPC, Université Clermont Auvergne, CNRS/IN2P3, Clermont-Ferrand, France
- 37 Nevis Laboratory, Columbia University, Irvington, NY, USA
- 38 Niels Bohr Institute, University of Copenhagen, Copenhagen, Denmark
- 39 (a)Dipartimento di Fisica, Università della Calabria, Rende, Italy; (b)INFN Gruppo Collegato di Cosenza, Laboratori Nazionali di Frascati, Cosenza, Italy
- 40 Physics Department, Southern Methodist University, Dallas, TX, USA
- 41 Physics Department, University of Texas at Dallas, Richardson, TX, USA
- 42 National Centre for Scientific Research “Demokritos”, Agia Paraskevi, Greece
- 43 (a)Department of Physics, Stockholm University, Stockholm, Sweden; (b)Oskar Klein Centre, Stockholm, Sweden
- 44 Deutsches Elektronen-Synchrotron DESY, Hamburg and Zeuthen, Germany
- 45 Fakultät Physik, Technische Universität Dortmund, Dortmund, Germany
- 46 Institut für Kern- und Teilchenphysik, Technische Universität Dresden, Dresden, Germany

- ⁴⁷ Department of Physics, Duke University, Durham, NC, USA
- ⁴⁸ SUPA-School of Physics and Astronomy, University of Edinburgh, Edinburgh, UK
- ⁴⁹ INFN e Laboratori Nazionali di Frascati, Frascati, Italy
- ⁵⁰ Physikalisches Institut, Albert-Ludwigs-Universität Freiburg, Freiburg, Germany
- ⁵¹ II. Physikalisches Institut, Georg-August-Universität Göttingen, Göttingen, Germany
- ⁵² Département de Physique Nucléaire et Corpusculaire, Université de Genève, Geneva, Switzerland
- ⁵³ ^(a)Dipartimento di Fisica, Università di Genova, Genoa, Italy; ^(b)INFN Sezione di Genova, Genoa, Italy
- ⁵⁴ II. Physikalisches Institut, Justus-Liebig-Universität Giessen, Giessen, Germany
- ⁵⁵ SUPA-School of Physics and Astronomy, University of Glasgow, Glasgow, UK
- ⁵⁶ LPSC, Université Grenoble Alpes, CNRS/IN2P3, Grenoble INP, Grenoble, France
- ⁵⁷ Laboratory for Particle Physics and Cosmology, Harvard University, Cambridge, MA, USA
- ⁵⁸ ^(a)Department of Modern Physics and State Key Laboratory of Particle Detection and Electronics, University of Science and Technology of China, Hefei, China; ^(b)Institute of Frontier and Interdisciplinary Science and Key Laboratory of Particle Physics and Particle Irradiation (MOE), Shandong University, Qingdao, China; ^(c)School of Physics and Astronomy, Key Laboratory for Particle Astrophysics and Cosmology (MOE), SKLPPC, Shanghai Jiao Tong University, Shanghai, China; ^(d)Tsung-Dao Lee Institute, Shanghai, China
- ⁵⁹ ^(a)Kirchhoff-Institut für Physik, Ruprecht-Karls-Universität Heidelberg, Heidelberg, Germany; ^(b)Physikalisches Institut, Ruprecht-Karls-Universität Heidelberg, Heidelberg, Germany
- ⁶⁰ ^(a)Department of Physics, Chinese University of Hong Kong, Shatin, N.T., Hong Kong, China; ^(b)Department of Physics, University of Hong Kong, Hong Kong, China; ^(c)Department of Physics and Institute for Advanced Study, Hong Kong University of Science and Technology, Clear Water Bay, Kowloon, Hong Kong, China
- ⁶¹ Department of Physics, National Tsing Hua University, Hsinchu, Taiwan
- ⁶² IJCLab, CNRS/IN2P3, Université Paris-Saclay, 91405 Orsay, France
- ⁶³ Department of Physics, Indiana University, Bloomington, IN, USA
- ⁶⁴ ^(a)INFN Gruppo Collegato di Udine, Sezione di Trieste, Udine, Italy; ^(b)ICTP, Trieste, Italy; ^(c)Dipartimento Politecnico di Ingegneria e Architettura, Università di Udine, Udine, Italy
- ⁶⁵ ^(a)INFN Sezione di Lecce, Lecce, Italy; ^(b)Dipartimento di Matematica e Fisica, Università del Salento, Lecce, Italy
- ⁶⁶ ^(a)INFN Sezione di Milano, Milan, Italy; ^(b)Dipartimento di Fisica, Università di Milano, Milan, Italy
- ⁶⁷ ^(a)INFN Sezione di Napoli, Naples, Italy; ^(b)Dipartimento di Fisica, Università di Napoli, Naples, Italy
- ⁶⁸ ^(a)INFN Sezione di Pavia, Pavia, Italy; ^(b)Dipartimento di Fisica, Università di Pavia, Pavia, Italy
- ⁶⁹ ^(a)INFN Sezione di Pisa, Pisa, Italy; ^(b)Dipartimento di Fisica E. Fermi, Università di Pisa, Pisa, Italy
- ⁷⁰ ^(a)INFN Sezione di Roma, Rome, Italy; ^(b)Dipartimento di Fisica, Sapienza Università di Roma, Rome, Italy
- ⁷¹ ^(a)INFN Sezione di Roma Tor Vergata, Rome, Italy; ^(b)Dipartimento di Fisica, Università di Roma Tor Vergata, Rome, Italy
- ⁷² ^(a)INFN Sezione di Roma Tre, Rome, Italy; ^(b)Dipartimento di Matematica e Fisica, Università Roma Tre, Rome, Italy
- ⁷³ ^(a)INFN-TIFPA, Povo, Italy; ^(b)Università degli Studi di Trento, Trento, Italy
- ⁷⁴ Institut für Astro- und Teilchenphysik, Leopold-Franzens-Universität, Innsbruck, Austria
- ⁷⁵ University of Iowa, Iowa City, IA, USA
- ⁷⁶ Department of Physics and Astronomy, Iowa State University, Ames, IA, USA
- ⁷⁷ Joint Institute for Nuclear Research, Dubna, Russia
- ⁷⁸ ^(a)Departamento de Engenharia Elétrica, Universidade Federal de Juiz de Fora (UFJF), Juiz de Fora, Brazil; ^(b)Universidade Federal do Rio De Janeiro COPPE/EE/IF, Rio de Janeiro, Brazil; ^(c)Instituto de Física, Universidade de São Paulo, São Paulo, Brazil
- ⁷⁹ KEK, High Energy Accelerator Research Organization, Tsukuba, Japan
- ⁸⁰ Graduate School of Science, Kobe University, Kobe, Japan
- ⁸¹ ^(a)AGH University of Science and Technology, Faculty of Physics and Applied Computer Science, Kraków, Poland; ^(b)Marian Smoluchowski Institute of Physics, Jagiellonian University, Kraków, Poland
- ⁸² Institute of Nuclear Physics Polish Academy of Sciences, Kraków, Poland
- ⁸³ Faculty of Science, Kyoto University, Kyoto, Japan
- ⁸⁴ Kyoto University of Education, Kyoto, Japan
- ⁸⁵ Research Center for Advanced Particle Physics and Department of Physics, Kyushu University, Fukuoka, Japan
- ⁸⁶ Instituto de Física La Plata, Universidad Nacional de La Plata and CONICET, La Plata, Argentina
- ⁸⁷ Physics Department, Lancaster University, Lancaster, UK

- 88 Oliver Lodge Laboratory, University of Liverpool, Liverpool, UK
- 89 Department of Experimental Particle Physics, Jožef Stefan Institute and Department of Physics, University of Ljubljana, Ljubljana, Slovenia
- 90 School of Physics and Astronomy, Queen Mary University of London, London, UK
- 91 Department of Physics, Royal Holloway University of London, Egham, UK
- 92 Department of Physics and Astronomy, University College London, London, UK
- 93 Louisiana Tech University, Ruston, LA, USA
- 94 Fysiska institutionen, Lunds universitet, Lund, Sweden
- 95 Departamento de Física Teórica C-15 and CIAFF, Universidad Autónoma de Madrid, Madrid, Spain
- 96 Institut für Physik, Universität Mainz, Mainz, Germany
- 97 School of Physics and Astronomy, University of Manchester, Manchester, UK
- 98 CPPM, CNRS/IN2P3, Aix-Marseille Université, Marseille, France
- 99 Department of Physics, University of Massachusetts, Amherst, MA, USA
- 100 Department of Physics, McGill University, Montreal, QC, Canada
- 101 School of Physics, University of Melbourne, Victoria, Australia
- 102 Department of Physics, University of Michigan, Ann Arbor, MI, USA
- 103 Department of Physics and Astronomy, Michigan State University, East Lansing, MI, USA
- 104 B.I. Stepanov Institute of Physics, National Academy of Sciences of Belarus, Minsk, Belarus
- 105 Research Institute for Nuclear Problems of Byelorussian State University, Minsk, Belarus
- 106 Group of Particle Physics, University of Montreal, Montreal, QC, Canada
- 107 P.N. Lebedev Physical Institute of the Russian Academy of Sciences, Moscow, Russia
- 108 National Research Nuclear University MEPhI, Moscow, Russia
- 109 D.V. Skobel'syn Institute of Nuclear Physics, M.V. Lomonosov Moscow State University, Moscow, Russia
- 110 Fakultät für Physik, Ludwig-Maximilians-Universität München, Munich, Germany
- 111 Max-Planck-Institut für Physik (Werner-Heisenberg-Institut), Munich, Germany
- 112 Graduate School of Science and Kobayashi-Maskawa Institute, Nagoya University, Nagoya, Japan
- 113 Department of Physics and Astronomy, University of New Mexico, Albuquerque, NM, USA
- 114 Institute for Mathematics, Astrophysics and Particle Physics, Radboud University/Nikhef, Nijmegen, The Netherlands
- 115 Nikhef National Institute for Subatomic Physics and University of Amsterdam, Amsterdam, The Netherlands
- 116 Department of Physics, Northern Illinois University, DeKalb, IL, USA
- 117 ^(a)Budker Institute of Nuclear Physics and NSU, SB RAS, Novosibirsk, Russia; ^(b)Novosibirsk State University Novosibirsk, Novosibirsk, Russia
- 118 Institute for High Energy Physics of the National Research Centre Kurchatov Institute, Protvino, Russia
- 119 Institute for Theoretical and Experimental Physics named by A.I. Alikhanov of National Research Centre “Kurchatov Institute”, Moscow, Russia
- 120 ^(a)New York University Abu Dhabi, Abu Dhabi, United Arab Emirates; ^(b)United Arab Emirates University, Al Ain, United Arab Emirates; ^(c)University of Sharjah, Sharjah, United Arab Emirates
- 121 Department of Physics, New York University, New York, NY, USA
- 122 Ochanomizu University, Otsuka, Bunkyo-ku, Tokyo, Japan
- 123 Ohio State University, Columbus, OH, USA
- 124 Homer L. Dodge Department of Physics and Astronomy, University of Oklahoma, Norman, OK, USA
- 125 Department of Physics, Oklahoma State University, Stillwater, OK, USA
- 126 Palacký University, Joint Laboratory of Optics, Olomouc, Czech Republic
- 127 Institute for Fundamental Science, University of Oregon, Eugene, OR, USA
- 128 Graduate School of Science, Osaka University, Osaka, Japan
- 129 Department of Physics, University of Oslo, Oslo, Norway
- 130 Department of Physics, Oxford University, Oxford, UK
- 131 LPNHE, CNRS/IN2P3, Sorbonne Université, Université de Paris, Paris, France
- 132 Department of Physics, University of Pennsylvania, Philadelphia, PA, USA
- 133 Konstantinov Nuclear Physics Institute of National Research Centre “Kurchatov Institute”, PNPI, St. Petersburg, Russia
- 134 Department of Physics and Astronomy, University of Pittsburgh, Pittsburgh, PA, USA
- 135 ^(a)Laboratório de Instrumentação e Física Experimental de Partículas - LIP, Lisbon, Portugal; ^(b)Departamento de Física, Faculdade de Ciências, Universidade de Lisboa, Lisbon, Portugal; ^(c)Departamento de Física, Universidade de Coimbra,

- Coimbra, Portugal; ^(d)Centro de Física Nuclear da Universidade de Lisboa, Lisbon, Portugal; ^(e)Departamento de Física, Universidade do Minho, Braga, Portugal; ^(f)Departamento de Física Teórica y del Cosmos, Universidad de Granada, Granada, Spain; ^(g)Instituto Superior Técnico, Universidade de Lisboa, Lisbon, Portugal
- 136 Institute of Physics of the Czech Academy of Sciences, Prague, Czech Republic
- 137 Czech Technical University in Prague, Prague, Czech Republic
- 138 Charles University, Faculty of Mathematics and Physics, Prague, Czech Republic
- 139 Particle Physics Department, Rutherford Appleton Laboratory, Didcot, UK
- 140 IRFU, CEA, Université Paris-Saclay, Gif-sur-Yvette, France
- 141 Santa Cruz Institute for Particle Physics, University of California Santa Cruz, Santa Cruz, CA, USA
- 142 ^(a)Departamento de Física, Pontificia Universidad Católica de Chile, Santiago, Chile; ^(b)Instituto de Investigación Multidisciplinario en Ciencia y Tecnología, y Departamento de Física, Universidad de La Serena, Santiago, Chile; ^(c)Universidad Andres Bello, Department of Physics, Santiago, Chile; ^(d)Instituto de Alta Investigación, Universidad de Tarapacá, Arica, Chile; ^(e)Departamento de Física, Universidad Técnica Federico Santa María, Valparaíso, Chile
- 143 Universidade Federal de São João del Rei (UFSJ), São João del Rei, Brazil
- 144 Department of Physics, University of Washington, Seattle, WA, USA
- 145 Department of Physics and Astronomy, University of Sheffield, Sheffield, UK
- 146 Department of Physics, Shinshu University, Nagano, Japan
- 147 Department Physik, Universität Siegen, Siegen, Germany
- 148 Department of Physics, Simon Fraser University, Burnaby, BC, Canada
- 149 SLAC National Accelerator Laboratory, Stanford, CA, USA
- 150 Department of Physics, Royal Institute of Technology, Stockholm, Sweden
- 151 Departments of Physics and Astronomy, Stony Brook University, Stony Brook, NY, USA
- 152 Department of Physics and Astronomy, University of Sussex, Brighton, UK
- 153 School of Physics, University of Sydney, Sydney, Australia
- 154 Institute of Physics, Academia Sinica, Taipei, Taiwan
- 155 ^(a)E. Andronikashvili Institute of Physics, Iv. Javakhishvili Tbilisi State University, Tbilisi, Georgia; ^(b)High Energy Physics Institute, Tbilisi State University, Tbilisi, Georgia
- 156 Department of Physics, Technion, Israel Institute of Technology, Haifa, Israel
- 157 Raymond and Beverly Sackler School of Physics and Astronomy, Tel Aviv University, Tel Aviv, Israel
- 158 Department of Physics, Aristotle University of Thessaloniki, Thessaloníki, Greece
- 159 International Center for Elementary Particle Physics and Department of Physics, University of Tokyo, Tokyo, Japan
- 160 Department of Physics, Tokyo Institute of Technology, Tokyo, Japan
- 161 Tomsk State University, Tomsk, Russia
- 162 Department of Physics, University of Toronto, Toronto, ON, Canada
- 163 ^(a)TRIUMF, Vancouver, BC, Canada; ^(b)Department of Physics and Astronomy, York University, Toronto, ON, Canada
- 164 Division of Physics and Tomonaga Center for the History of the Universe, Faculty of Pure and Applied Sciences, University of Tsukuba, Tsukuba, Japan
- 165 Department of Physics and Astronomy, Tufts University, Medford, MA, USA
- 166 Department of Physics and Astronomy, University of California Irvine, Irvine, CA, USA
- 167 Department of Physics and Astronomy, University of Uppsala, Uppsala, Sweden
- 168 Department of Physics, University of Illinois, Urbana, IL, USA
- 169 Instituto de Física Corpuscular (IFIC), Centro Mixto Universidad de Valencia - CSIC, Valencia, Spain
- 170 Department of Physics, University of British Columbia, Vancouver, BC, Canada
- 171 Department of Physics and Astronomy, University of Victoria, Victoria, BC, Canada
- 172 Fakultät für Physik und Astronomie, Julius-Maximilians-Universität Würzburg, Würzburg, Germany
- 173 Department of Physics, University of Warwick, Coventry, UK
- 174 Waseda University, Tokyo, Japan
- 175 Department of Particle Physics and Astrophysics, Weizmann Institute of Science, Rehovot, Israel
- 176 Department of Physics, University of Wisconsin, Madison, WI, USA
- 177 Fakultät für Mathematik und Naturwissenschaften, Fachgruppe Physik, Bergische Universität Wuppertal, Wuppertal, Germany
- 178 Department of Physics, Yale University, New Haven, CT, USA

- ^a Also at Borough of Manhattan Community College, City University of New York, New York, NY, USA
- ^b Also at Bruno Kessler Foundation, Trento, Italy
- ^c Also at Center for High Energy Physics, Peking University, Beijing, China
- ^d Also at Centro Studi e Ricerche Enrico Fermi, Rome, Italy
- ^e Also at CERN, Geneva, Switzerland
- ^f Also at Département de Physique Nucléaire et Corpusculaire, Université de Genève, Geneva, Switzerland
- ^g Also at Departament de Física de la Universitat Autònoma de Barcelona, Barcelona, Spain
- ^h Also at Department of Financial and Management Engineering, University of the Aegean, Chios, Greece
- ⁱ Also at Department of Physics and Astronomy, Michigan State University, East Lansing, MI, USA
- ^j Also at Department of Physics and Astronomy, University of Louisville, Louisville, KY, USA
- ^k Also at Department of Physics, Ben Gurion University of the Negev, Beer Sheva, Israel
- ^l Also at Department of Physics, California State University, East Bay, USA
- ^m Also at Department of Physics, California State University, Fresno, USA
- ⁿ Also at Department of Physics, California State University, Sacramento, USA
- ^o Also at Department of Physics, King's College London, London, UK
- ^p Also at Department of Physics, St. Petersburg State Polytechnical University, St. Petersburg, Russia
- ^q Also at Department of Physics, University of Fribourg, Fribourg, Switzerland
- ^r Also at Faculty of Physics, M.V. Lomonosov Moscow State University, Moscow, Russia
- ^s Also at Faculty of Physics, Sofia University, 'St. Kliment Ohridski', Sofia, Bulgaria
- ^t Also at Graduate School of Science, Osaka University, Osaka, Japan
- ^u Also at Hellenic Open University, Patras, Greece
- ^v Also at Institutio Catalana de Recerca i Estudis Avancats, ICREA, Barcelona, Spain
- ^w Also at Institut für Experimentalphysik, Universität Hamburg, Hamburg, Germany
- ^x Also at Institute for Particle and Nuclear Physics, Wigner Research Centre for Physics, Budapest, Hungary
- ^y Also at Institute of Particle Physics (IPP), Victoria, Canada
- ^z Also at Institute of Physics, Azerbaijan Academy of Sciences, Baku, Azerbaijan
- ^{aa} Also at Institute of Theoretical Physics, Ilia State University, Tbilisi, Georgia
- ^{ab} Also at Instituto de Física Teórica, IFT-UAM/CSIC, Madrid, Spain
- ^{ac} Also at Department of Physics, Istanbul University, Istanbul, Turkey
- ^{ad} Also at Joint Institute for Nuclear Research, Dubna, Russia
- ^{ae} Also at Moscow Institute of Physics and Technology State University, Dolgoprudny, Russia
- ^{af} Also at National Research Nuclear University MEPhI, Moscow, Russia
- ^{ag} Also at Physics Department, An-Najah National University, Nablus, Palestine
- ^{ah} Also at Physikalisches Institut, Albert-Ludwigs-Universität Freiburg, Freiburg, Germany
- ^{ai} Also at The City College of New York, New York, NY, USA
- ^{aj} Also at TRIUMF, Vancouver, BC, Canada
- ^{ak} Also at Università di Napoli Parthenope, Naples, Italy
- ^{al} Also at University of Chinese Academy of Sciences (UCAS), Beijing, China
- ^{am} Also at Yeditepe University, Physics Department, Istanbul, Turkey
- * Deceased